INFLUENCE OF Mn SUBSTITUTION ON THE STRUCTURAL, ELECTRICAL AND MAGNETIC PROPERTIES OF Ni-Cu-Cd BULK FERRITES SINTERED FROM NANOCRYSTALLINE POWDER

MIA MD FAKHARUDDIN ALI MAZLOBEE

M.Phil.THESIS

DEPARTMENT OF SCIENCE AND HUMANITIES
MILITARY INSTITUTE OF SCIENCE AND TECHNOLOGY
DHAKA, BANGLADESH

MARCH 2023

INFLUENCE OF Mn SUBSTITUTION ON THE STRUCTURAL, ELECTRICAL AND MAGNETIC PROPERTIES OF Ni-Cu-Cd BULK FERRITES SINTERED FROM NANOCRYSTALLINE POWDER

MIA MD FAKHARUDDIN ALI MAZLOBEE (S.N.1016400002)

A Thesis Submitted in Partial Fulfillment of the Requirements for the
Degree of Master of Philosophy in Physics

DEPARTMENT OF SCIENCE AND HUMANITIES
MILITARY INSTITUTE OF SCIENCE AND TECHNOLOGY
DHAKA, BANGLADESH

MARCH 2023

INFLUENCE OF Mn SUBSTITUTION ON THE STRUCTURAL, ELECTRICAL AND MAGNETIC PROPERTIES OF Ni-Cu-Cd BULK FERRITES SINTERED FROM NANOCRYSTALLINE POWDER

M.Phil. Thesis

By

MIA MD FAKHARUDDIN ALI MAZLOBEE (Roll No:1016400002)

Approved as to style and content by the Board of Examination on 12 March 2023

____

Maj Md Mahabubar Rahman Shah, MPhil, PhD
Instructor Class 'B'
Department of Science & Humanities
MIST, Dhaka

Chairman (Supervisor)
Board of Examination

____

Dr Mohammad Belal Hossen
Professor
Department of Physics
CUET, Chittagong

Member (Co-Supervisor)
Board of Examination

____

Col Md Shahinoor Alam, SSP, PEng
Head of Department
Department of Science & Humanities
MIST, Dhaka

Head of the Department
Member (Ex-Officio)

____

Col Eare Md Morshed Alam, MPhil, PhD
Senior Instructor
Department of Science & Humanities
MIST, Dhaka

Member
Board of Examination

____

Dr A K M Akther Hossain
Professor
Department of Physics
BUET, Dhaka

Member (External)
Board of Examination

____

Dr Mohammed Nazrul Islam Khan
Chief Scientific Officer
Bangladesh Atomic Energy Commission

Member (External)
Board of Examination

Department of Science & Humanities, MIST, Dhaka

INFLUENCE OF Mn SUBSTITUTION ON THE STRUCTURAL, ELECTRICAL AND MAGNETIC PROPERTIES OF Ni-Cu-Cd BULK FERRITES SINTERED FROM NANOCRYSTALLINE POWDER

DECLARATION

I hereby declare that the study reported in this thesis entitled as above is my own original work and has not been submitted before anywhere for my degree or other purposes. Further I certify that the intellectual content of this thesis is the product of my own work and that all the assistance received in preparing this thesis and sources have been acknowledged and / or cited in the reference section.

Mia Md Fakharuddin Ali Mazlobee

Department of Science & Humanities, MIST, Dhaka

INFLUENCE OF Mn SUBSTITUTION ON THE STRUCTURAL, ELECTRICAL AND MAGNETIC PROPERTIES OF Ni-Cu-Cd BULK FERRITES SINTERED FROM NANOCRYSTALLINE POWDER

A Thesis

By

Mia Md Fakharuddin Ali Mazlobee

DEDICATION

Dedicated to my parents for supporting and
encouraging me to believe in myself

ACKNOWLEDGEMENTS

Alhamdulillah, I express my humble gratitude to **Allah Rabbul A’lameen** whose unceasing and everlasting blessings enabled me to complete the research and submit the thesis in time.

I express my profound gratitude to my respected supervisor **Major Md Mahabubar Rahman Shah**, MPhil, PhD, Department of Science and Humanities (Physics Division), Military Institute of Science and Technology (MIST) for his constant advice, constructive criticism and inspiration during the whole period of present investigation. Moreover, I am owed to him for his additional caring and solving different administrative issues related to this experimental work.

With deep respect and honor, I would like to express fervently my earnest gratitude and indebtedness to my respected thesis Co-supervisor **Prof Dr Mohammad Belal Hossen**, Physics Department of Chittagong University of Engineering and Technology (CUET) for rendering me opportunity to perform my research work with all-out support and invaluable guidance throughout this academic journey. He has educated me the execution of research methodology and taught how to present the work in a clear and simple way. I would also like to thank him for his friendship, empathy and mental support in different critical situations.

I am deeply grateful to **Colonel Md Shahinoor Alam**, SPP, PEng, Head, Department of Science and Humanities, Military Institute of Science and Technology (MIST), for his cooperation and coordination at different stages of the work. His valuable suggestions, timely guidance and constructive criticisms are praise-worthy and valuable assets for my life. I am also extremely grateful to the MIST authorities for providing the necessary financial grant for the research.

I would like to thank all the respected teachers of the Department of Science and Humanities, MIST and Department of Physics, CUET, special thanks to **Captain M Ziaul Ahsan**, PhD (Ex Head of the Department), **Lieutenant Colonel Brajalal Sinha**, PhD, **Major Tahmina Rahman** of MIST for their cooperation. My special thank goes to affectionate junior brother **M. Faishal Mahmood**, a PhD student at Department of Physics in CUET who was a co-partner in Functional Nanomaterials Laboratory. I am also thankful to my respected mentor **Colonel Eare Md Morshed Alam**, MPhil, PhD for his consistent mental support. I also would like to convey my thanks to the employees of the department of Physics, CUET and MIST for their co-operation and help specially to **Mr Sohel Rana**.

I would like to acknowledge the moral support and the sustained inspiration of my loving wife **Farhana Rahman** and affectionate son **Fasih Ur Rahman** along with all other members of my family. This dissertation would have never been possible without their love, affection, encouragement and sacrifices.

Finally, I am extremely grateful to my blessed parents, siblings and uncles for their love, caring, sacrifices, and prayers for preparing and educating me for my future.

ABSTRACT

Influence of Mn Substitution on the Structural, Electrical and Magnetic Properties of Ni-Cu-Cd Bulk Ferrites Sintered from Nanocrystalline Powder

Maintaining nanoscale properties in a high-density bulk form of ferrite prepared from powdered nanoparticles is quite desirable in many high frequency applications. Various $Ni_{0.5-x}Mn_xCu_{0.2}Cd_{0.3}Fe_2O_4$ (NMCCFO, x = 0.0, 0.1, 0.2, 0.3, 0.4 and 0.5) dense bulk ferrites were consolidated from nano-crystalline powders by the sol-gel auto-combustion technique. Commercially available different nitrate salts of the ingredients were mixed thoroughly in stoichiometric amount and were calcined at 700°C for 5 h. Pellet and toroid shaped samples prepared from each composition were sintered at 1200°C for 5 h.

X-ray diffraction (XRD) was used to carry out the structural analyses. The XRD data confirm that all compositions are single phase spinel structure. The lattice constant increase with increasing Mn content which is a clear indication of Mn incorporation in spinel structure. The theoretical density and the bulk density decrease but the porosity increases with increasing Mn content. The Rietveld refinement method confirms the goodness of fit with refined XRD data of *NMCCFO* for different Mn content. Rietveld technique is also adopted to determine the cation distribution between tetrahedral and octahedral sites and shows that maximum migration of Fe ions from A to B-sites occurs for x = 0.2 of Mn content.

The Maximum Entropy Map analysis reveals the variation of the electron density with increasing Mn content and the presence of strong covalent bonding. Field emission scanning electron microscopy (FE-SEM) is used to carry out the surface morphology analyses. The average grain sizes increases from 1 μm to 4 μm for all compositions except x = 0.5 of Mn content. Energy dispersive X-ray (EDX) findings confirm the absence of traceable impurities and presence of Ni, Mn, Cu, Cd, Fe, and O in the samples.

The dielectric measurements as a function of frequency and compositions are carried out at room temperature in the frequency range 100 Hz to 100 MHz. The dielectric constant ($\varepsilon^{/}$) and the dielectric loss tangent (tan δ) remains high at low frequency but becomes independent of frequency at higher frequencies for all the compositions of *NMCCFO.* This phenomenon may be explained by the Maxwell–Wagner model. The ac conductivity (σ_{ac}) is derived from the dielectric measurements and it increases with increasing of frequency for all the compositions of *NMCCFO.*

Frequency dependence of real ($M^{/}$) and imaginary ($M^{//}$) parts of the electric modulus and real ($Z^{/}$) and imaginary ($Z^{//}$) parts of the complex impedance for different composition are measured at room temperature. The Cole-Cole plots ($M^{/}$ vs $M^{//}$) of electric modulus exhibit a tendency of formation of a single semicircular arc for all compositions indicates the existence of single-phase nature of the materials as well as the improvement in conductivity. Also, the Cole-Cole plots ($Z^{/}$ vs $Z^{//}$) of complex impedance exhibit a tendency of formation of semicircles end in the high frequency region. It explains the dominancy of the grain boundary.

The vibrating sample magnetometer (VSM) was used for magnetization measurement at room temperature. From the hysteresis loop, the saturation magnetisation (M_s), remanent magnetisation (M_r), coercivity (H_c), the ratio (R) of M_r and M_s, anisotropy constant (K_1), and magnetisation magnetic moment (μ_B) are calculated. All the compositions show the nature of soft ferrite due to the small amount of remanence and coercivity. Theoretical law of approach to saturation (LAS) shows that the values for both the saturation magnetization (M_s) and anisotropy constant (K_1) are lesser than the experimental value.

Therefore, the unique combination of electric and magnetic properties like low dielectric loss tangent, high ac conductivity and soft ferrite like behavior make the *NMCCFO* materials suitable for manufacturing high frequency devices like Multilayer Ferrite Chips Inductor (MLFCI), phase shifters, switches, etc.

সারসংক্ষেপ

Influence of Mn Substitution on the Structural, Electrical and Magnetic Properties of Ni-Cu-Cd Bulk Ferrites Sintered from Nanocrystalline Powder

গুড়ো ন্যানো পার্টিক্যাল (powdered nano particle) থেকে তৈরি উচ্চ ঘনত্বের বাল্ক (bulk) আকৃতির ফেরাইট (ferrite) উপাদানে ন্যানো স্কেল বৈশিষ্ট্যগুলি বজায় রাখা অনেক উচ্চ ফ্রিকোয়েন্সি (high frequency) অ্যাপ্লিকেশনগুলিতে বেশ প্রয়োজনীয়। বিভিন্ন $Ni_{0.5-x}Mn_xCu_{0.2}Cd_{0.3}Fe_2O_4$ (NMCCFO, $x = 0.0, 0.1, 0.2, 0.3, 0.4$ এবং 0.5) ঘন বাল্ক ফেরাইটগুলি সল-জেল (sol-gel) স্বয়ংক্রিয় দহন (auto-combustion) কৌশল দ্বারা ন্যানোক্রিস্টাললাইন পাউডার (nano-crystalline powder) থেকে গঠিত (consolidated) হয়েছিল। বানিজ্যিকভাবে সংগৃহিত উপাদানগুলির বিভিন্ন নাইট্রেট লবণকে স্টোইকিওমেট্রিক (stoichiometric) পরিমাণে পুঙ্খানুপুঙ্খভাবে মিশ্রিত করা হয়েছিল এবং ৫ ঘন্টার জন্য ৭০০ ডিগ্রি সেলসিয়াস তাপমাত্রায় ক্যালসাইন (calcine) করা হয়েছিল। প্রতিটি কম্পোজিশন থেকে তৈরি পেলেট (Pellet) এবং টরয়েড (Toroid) আকৃতির নমুনাগুলি ১২০০ ডিগ্রি সেলসিয়াস তাপমাত্রায় ৫ ঘন্টার জন্য সিন্টার (sinter) করা হয়েছিল।

এক্স-রে ডিফ্রাকশন (XRD) কাঠামোগত বিশ্লেষণ করতে ব্যবহৃত হয়। এক্সআরডি (XRD) ডেটা, সমস্ত নমুনাগুলির একক দশা (phase) স্পিনেল ফেরাইট (spinel ferrite) কাঠামো নিশ্চিত করে। ক্রমবর্ধমান Mn উপাদানের সাথে ল্যাটিস ধ্রুবকের (lattice constant) বৃদ্ধি যা স্পিনেল কাঠামোতে Mn অন্তর্ভূক্তির একটি স্পষ্ট ইঙ্গিত প্রদান করে। ক্রমবর্ধমান Mn সংযুক্তিতে তাত্ত্বিক ঘনত্ব (X-ray density) এবং বাল্ক ঘনত্ব (Bulk density) হ্রাস পায় কিন্তু সরুত্ব (porosity) বৃদ্ধি পায়। রিটভেল্ট রিফাইনমেন্ট (Rietveld refinement) পদ্ধতি বিভিন্ন মাত্রার Mn উপাদানের জন্য NMCCFO এর পরিমার্জিত এক্সআরডি (XRD) ডেটার সাথে Goodness of fit কে নিশ্চিত করে। টেট্রাহেড্রাল এবং অক্টাহেড্রাল সাইটগুলির মধ্যে ধনাত্মক আয়নের (cationic distribution) বন্টন নির্ধারণের জন্যও রিটভেল্ড কৌশল (Rietveld Technique) গৃহিত হয় এবং দেখা যায় যে, এ- সাইটগুলি থেকে বি- সাইটগুলি আয়রন (Fe) আয়নগুলির সর্বাধিক স্থানান্তর ঘটে $x = 0.2$ Mn উপাদানের জন্য।

সর্বাধিক এনট্রপি মানচিত্র (maximum entropy map) বিশ্লেষণ, Mn মাত্রা বৃদ্ধির সাথে ইলেকট্রন ঘনত্বের তারতম্য এবং শক্তিশালী সমযোজী বন্ধনের (Covalent bonding) উপস্থিতি প্রকাশ করে। এফইএসইএম (FESEM)) পৃষ্ঠের রূপবিদ্যা (surface morphology) বিশ্লেষণ করতে ব্যবহৃত হয়। Mn মাত্রার $x = 0.5$ ধাপ ব্যতীত সমস্ত নমুনাগুলির জন্য গড় গ্রেইনের আকার (grain size)

১ মাইক্রোমিটার থেকে ৪ মাইক্রোমিটার পর্যন্ত বৃদ্ধি পায়। এনার্জি ডিসপারসিভ এক্স-রে (EDX) ফলাফল, সনাক্তযোগ্য এমন অপদ্রব্যগুলির অনুপস্থিতি এবং নমুনাগুলিতে Ni, Mn, Cu, Cd, Fe এবং O এর উপস্থিতি নিশ্চিত করে।

ফ্রিকোয়েন্সি এবং কম্পোজিশনের ফাংশন (Function) হিসেবে অন্তরক (dielectric) পরিমাপগুলি ১০০ হার্টজ থেকে ১০০ মেগা হার্টজ এর ফ্রিকোয়েন্সি পরিসীমায় (frequency range) ঘরের তাপমাত্রায় পরিমাপ করা হয়। অন্তরক ধ্রুবক (dielectric constant) এবং অন্তরক ক্ষতির স্পর্শক (dielectric loss) কম ফ্রিকুয়েন্সিতে উচ্চ থাকে কিন্তু NMCCFO এর সমস্ত নমুনাগুলির জন্য উচ্চতর ফ্রিকোয়েন্সিতে ফ্রিকোয়েন্সি ইন্ডিপেন্ডেন্ট হয়ে যায়। এই ঘটনাটি ম্যাক্সওয়েল-ওয়াগনার মডেল দ্বারা ব্যাখ্যা করা যেতে পারে। এসি পরিবাহিতা (ac conductivity) ডাইইলেকট্রিক পরিমাণ থেকে প্রাপ্ত এবং এটি NMCCFO এর সমস্ত কম্পোজিশন জন্য ফ্রিকোয়েন্সি বৃদ্ধির সাথে বৃদ্ধি পায়।

বৈদ্যুতিক মডুলাসের বাস্তব ($M^{/}$) এবং কাল্পনিক ($M^{//}$) অংশগুলির ফ্রিকোয়েন্সি নির্ভরতা এবং বিভিন্ন নমুনার জন্য জটিল ইম্পিডেন্সের (complex impedance) বাস্তব ($Z^{/}$) কাল্পনিক ($Z^{//}$) অংশগুলি ঘরের তাপমাত্রায় পরিমাপ করা হয়। বৈদ্যুতিক মডুলাসের কোলে -কোলে (Cole-Cole) প্লটগুলি সমস্ত নমুনাগুলির জন্য একটি একক অর্ধবৃত্ত তৈরির প্রবণতা প্রদর্শন করে। এটি বিভিন্ন মাত্রার উপকরণগুলির একক দশা (unit-phase) প্রকৃতির অস্তিত্বের পাশাপাশি পরিবাহিতা উন্নতির ইঙ্গিত দেয়। এছাড়াও জটিল ইমপিডেন্সের কোলে-কোলে প্লট (Cole-Cole plote) উচ্চ ফ্রিকোয়েন্সি অঞ্চলে অর্ধবৃত্ত তৈরির প্রবণতা প্রদর্শনের মাধ্যমে গ্রেইন সীমান্তের (grain boundary) প্রাধান্য বর্ণনা করে।

ভিএসএম (VSM) ঘরের তাপমাত্রায় চৌম্বকীয়করণ (Magnatization) পরিমাপের জন্য ব্যবহৃত হয়েছিল। হিস্টেরেসিস লুপ থেকে স্যাচুরেশন ম্যাগনেটাইজেশন (M_s), রিমানেন্ট ম্যাগনেটাইজেশন (M_r) কোয়ারসিভিটি (H_c), M_s / M_r এর হার, অ্যানাইসোট্রপি ধ্রুবক (K_1) এবং ম্যাগনেটাইজেশন ম্যাগনেট্রিক মোমেন্ট (μ_B) গণনা করা হয়। সমস্ত নমুনাগুলি অল্প পরিমাণে রেমিনেন্স (M_r) এবং কোয়ারসিভিটি (H_c) এর কারণে সফট ফেরাইটের (soft ferrite) প্রকৃতি প্রদর্শন করে। তত্ত্বীয় ল অব অ্যাপ্রোচ টু স্যাচুরেশন (LAS) দেখায় যে, স্যাচুরেশন ম্যাগনেটাইজেশন (M) এবং অ্যানাইসোট্রপি ধ্রুবক (K_1) উভয়ের মানই পরীক্ষামূলক মানের চেয়ে কম।

সতরাং বৈদ্যুতিক এবং চৌম্বকীয় বৈশিষ্ট্যগুলির অনন্য সমন্বয়, যেমন নিম্ন ডাইলেকট্রিক লস ট্যানজেন্ট (tan δ), উচ্চ এসি পরিবাহিতা এবং নরম ফেরাইটের মতো আচরণ এনএমসিসিএফও (NMCCFO) উপকরণগুলিকে মাল্টিলেয়ার ফেরাইট চিপস ইনডাকটর (MLFCI), ফেজ শিফটার, সুইচ ইত্যাদির মতো উচ্চ ফ্রিকোয়েন্সি ডিভাইস তৈরির জন্য উপযুক্ত করে তোলে।

LIST OF MAIN NOTATIONS

λ	X-ray wavelength
Ni-Cu-Cd	Nickel-Copper-Cadmium
N	Avogadro’s number
M_W	Molecular weight
M_S	Saturation Magnetization
MLFCI	Multilayer ferrite chip inductor
M	Magnetization
^{o}C	Degree Celsius
(hkl)	Miller index
a	Lattice parameter
B	Octahedral sites
A	Tetrahedral sites
P	Porosity
ρ_x	X-ray density
β	Full width at half maximum of XRD peak
XRD	X-ray diffraction
C	Capacitance
d	Lattice spacing
D_{in}	Inner diameter
D_{od}	Outer diameter
ρ_{exp}	Bulk density
ω	Angular frequency
PVA	Polyvinyl alcohol
Q	Quality factor
RE	Rare earth
RLF	Relative loss factor
D	Crystallite size
t	Thickness

JCPDS	Joint committee on powder diffraction standards
TGA	Thermo gravimetric analysis
VSM	Vibrating sample magnetometer
G	Goodness of fit
MEM	Maximum Entropy Map
LAS	Law of Approach to Saturation
M_r	Remanent magnetization
K_1	Anisotropy constant
FESEM	Field Emission Scanning Electron Microscope
EDX	Energy Dispersive X-ray

LIST OF FIGURES

LIST OF TABLES

TABLE OF CONTENTS

CHAPTER 1: INTRODUCTION

CHAPTER 2: LITERATURE REVIEWS

CHAPTER 3: SYNTHESIS PROCEDURE

CHAPTER 4: EXPERIMENTAL TECHNIQUES

CHAPTER 5: RESULTS AND DISCUSSION

CHAPTER 6: CONCLUSIONS AND RECOMMENDATIONS

CHAPTER 1
INTRODUCTION

1.1 General

The present trend of technological demand is to develop the miniaturization and cost- effective new materials with high performance devices. Thereby, nanoparticles technology draw attention to facilitate and easing these problems and plentiful of research works are going on in these fields. Therefore, the inclusion of nanoparticle technology in preparing nano ferrite has further revolutionized the possibility of invention new materials in the different applied field (Callister, David and Rethwisch, 2013, Devmunde et al., 2016, Valenzuela, 2012, Thakura et al. 2020). In the recent years, spinel nano-ferrite with general formula AB_2O_4 is gaining interest to the electronic industries because of wide variety of applications in different fields (e.g., inductors, high frequency devices, biosciences, low dielectric loss, high ac conductivity, high electrical resistivity, high saturation magnetization etc.). At present, with the inception of high-frequency applications, electronic industries are in need of ferrite-based materials with low dielectric loss and high ac conductivity. In this new criteria, Nickel (Ni) based ferrite with the desirable novel properties along with lower cost and easy processing method would fit itself as a potential candidate for using in various microwave devices e.g. circulators, isolators, phase shifters and antennas (Hossen, Nasrin and Hossen, 2020, Arifuzaman et al. 2016, Tatarchuk et al. 2017, Narang and Pubby, 2021).

In contrast with bulk materials, ferrite nanoparticles exhibit unusual structural and electrical along with magnetic properties, e.g., single domain characteristics, lower curie temperature, super-paramagnetism, and magnetization. It also shows enhanced dielectric properties due to its size and surface effect (Arifuzaman et al., 2016, Hashim et al., 2013). On the other hand, investigating the processing and properties analysis of high dense bulk ferrite synthesized from nano-powder significantly became a complex research objective to material engineers and scientists. In many electronic applications specially in high frequency domain, high density bulk form is required instead of nano powder form. For retaining the unusual electromagnetic properties of nano particles, grain size in polycrystalline solid structure should be maintained in the nanometric range. To consolidate nano-particles into high density bulk solids, the traditional sintering procedures, based on thermal treatments at high temperatures for extended periods of time, are typically used. The transforming of bulk ferrite synthesized from nano-powder retaining nano behavior within the structure significantly differs in functional properties from those of nano-powder and bulk separately (Valenzuela, Gaudisson and Ammar, 2015, Morales et al., 2008).

A spinel ferrite unit cell consists of 8 fcc formula cells. The ionic formula is MFe_2O_4 derived from mineral spinel structure $MgAl_2O_4$ where M represents divalent metal ion. Its basic formula is $(A)[B]_2O_4$ where A and B sites are known as tetrahedral and octahedral sites respectively within a cubic closed-packed arrangement that is formed by oxygen atoms. In cubic unit cell arrangement, total atoms number is 56: out of which 32 oxygen anions and 24 cations (one-eighth of 64 A-sites and half of 32 B-sites). A large part of unoccupied sites remains in crystal structure of spinel ferrites which facilitates migration of cations. Thereby, structural, electrical and magnetic properties are highly influenced by cationic distribution. The metal ions like Co, Ni, Cr tend to occupy B sites, Mn, Zn prefer A sites and Fe occupy at both sites. The crystal makeup of spinel ferrite is explained by formula $(Me^{2+}_{1-x}Fe^{3+}_{x})_A$ $[Me^{2+}_{x}Fe^{3+}_{2-x}]_B\,O_4$, where x = 0 for normal spinel and x = 1 for inverse structure and x is called inversion parameter which varies with synthesis methods. The occupancy of larger cations and expansion of A and B sites are characterized by oxygen parameter (u) which refers to oxygen movement during the substitution process of cations (Devmunde et al., 2016, Tatarchuk et al., 2017, Narang and Pubby, 2021). Thus, the substitution of transition metals such as Mn, Cu, Cd, Co causes significant change in physical and electromagnetic properties in spinel ferrite materials (Singh, Srinivas and Tirupanyam, 2016).

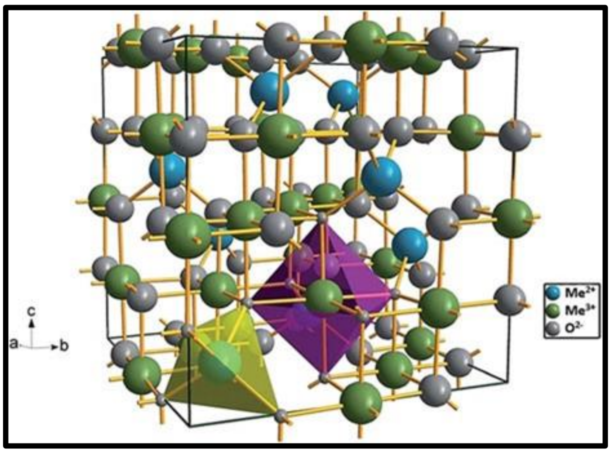

Fig. 1.1: Unit cell of spinel ferrite with general formula $MeFe_2O_4$ (Thakura et al., 2020).

Currently, as a point of interest, many research groups have been focusing on investigating the influence of Mn substitution on various compositions of Ni-based spinel ferrite materials to modify the synthesis routes as well as structural and electromagnetic characteristics and find the possibility to improve upon (Shelar et al., 2009, Raju, Balaji and Reddy, 2014, Siddique et al., 2003, Zhao et al., 2007, Kumar and Jayaprakash, 2013, Hassan et al., 2013). The substitution of Mn^{2+} ion at Ni^{2+} sites affect spinel chemical composition significantly and improves magnetic properties along with increased electrical resistivity because of its large magnetic moment (5 μ_B) and controlled distribution of cations in both the sites which ultimately facilitates high-frequency applications (Callister, David and Rethwisch,2013, Shelar et al., 2009, Raju, Balaji and Reddy, 2014).

Furthermore, the preparation condition and synthesis route have a direct effect on composition, morphology, and crystallite size which are being correlated with physical and chemical makeup (Mokdad, Hassan and Awad, 2019). The basic operational principle of producing nanoparticles is ‘the synchronization of a high rate of nucleation with a low rate of growth (Lyakishev, Alymov and Dobatkin, 2003). Moreover, the economical aspect also needs to be considered. Thus, it is very important to employ a feasible synthesis method for expected properties. To produce high-quality ferrite nanoparticles, the sol-gel auto-combustion technique is appropriate for our study (Hossen and Hossen, 2019) due to its required advantages significantly lower cost, non-toxicity, easy control etc.

Till today, various research works have been carried out on the different compositions of Ni ferrites with various substitutions to enhance the electrical and magnetic properties. But a little research work is observed on Mn substituted $Ni_{0.5-x}Mn_xCu_{0.2}Cd_{0.3}Fe_2O_4$ (NMCCFO) dense bulk ferrite. The present work focus on observing nanoscale effect in bulk form and the changes in structural, electrical and magnetic properties of Mn substituted NMCCFO high dense bulk ferrite sintered at 1200°C for future applicability. In this study, the sol-gel auto-combustion synthesis route are employed. The structural analysis, surface morphology, elemental study, electrical and magnetic properties of the dense bulk ferrite are investigated.

1.2 Objectives of the Present Research

The main objectives are as follows:

- Synthesis of $Ni_{0.5-x}Mn_xCu_{0.2}Cd_{0.3}Fe_2O_4$ (x = 0.0, 0.1, 0.2, 0.3, 0.4 and 0.5) ferrite nanoparticles by using sol-gel auto-combustion technique and sintered at 1200°C.
- Study of structural characterization, surface morphology, saturation magnetization (Ms) and frequency dependent transport properties.

1.3 Possible Outcome

The sol-gel auto combustion technique is expected to produce high purity ultrafine nanoparticles by controlling the stoichiometric amount. Cation like manganese (Mn^{2+}) substituting in the parent component of $NiCuCdFe_2O_4$ may change the various properties like dielectric, electric, magnetic etc. Therefore, the present high density bulk samples with low dielectric loss and high ac conductivity may be used as a raw material for manufacturing frequency dependent communication devices like multilayer ferrite chip inductor's (MLFCI), sensors, circulators, isolators, phase shifters and antennas in high frequency applications.

1.4 Outline of the Thesis

This thesis consists of six chapters. These are:

Chapter 1: Introduction (Motivation and objectives of the present work)

This chapter begins with a general introduction to give a clear idea of the present research work chronologically. Therefore, it mentions the objectives of this research along with possible outcome in Bangladeshi perspective. Lastly, it draws the outline of the research.

Chapter 2: Literature Reviews

This chapter presents the theoretical background of ferrite, its compositions, types in addition to crystal structure of spinel ferrite and its cation distribution. Besides, it discusses Ni-Cu-Cd ferrite, effect of substitution and synthesis of magnetic nanoparticles from different scientific literatures.

Chapter 3: Synthesis

It describes details of the preparation methods with related apparatus and shows production of powder and bulk sample from raw materials.

Chapter 4: Experimental Techniques

Structural characterization by XRD and data analysis by Reitveld refinement method, morphological study and elemental discussion explained by FESEM and EDX analysis are discussed in this chapter. Electric and magnetic parameters measurement are also explained.

Chapter 5: Results and Discussion

Here, results of different experiments and their minute discussions related to present study are thoroughly explained with different tables and diagrams.

Chapter 6: Conclusions and Recommendations

Concluding remarks are drawn from overall experimental study and recommendations for future scope are the containment of this chapter.

CHAPTER 2
LITERATURE REVIEWS

2.1 Introduction

Modern civilization stands on the solid foundation which has been created and strengthened with the contributions of past and continuing science and technological development found in the history. Ferrite itself has its own historical development inside the world of magnetism. The significant properties of ferrites could be varied by tailoring their complex magnetic structure to make it useful for high frequency applications. This chapter describes sequentially origin, types, crystal structure, synthesis method, cation distribution inside ferrite and effect of substitution of divalent cation from the literatures of other investigators working in this experimental field.

2.2 Overview of the Ferrites

Ferrites which are also known as magnetic oxides are members of ferrimagnetic material. These materials contain iron oxide as main constituent elements. The ferrites are commonly expressed by general chemical formula $M_eO.M_tO_3$ where M_e depicts as Fe^{2+}, Ni^{2+}, Mg^{2+}, Cu^{2+}, Mn^{2+}, or Zn^{2+} and M_t is represented as Fe^{3+}, Mn^{3+}, Co^{3+}, Al^{3+}, Ga^{3+} etc. Here O is oxygen ions. Besides, mixed ferrites can be produced e.g. (Mg-Mn) Fe_2O_4, (Ni-Zn) Fe_2O_4, (Mg-Ni) Fe_2O_4 The different crystal structures of ferrites are shown in Figure 2.1.

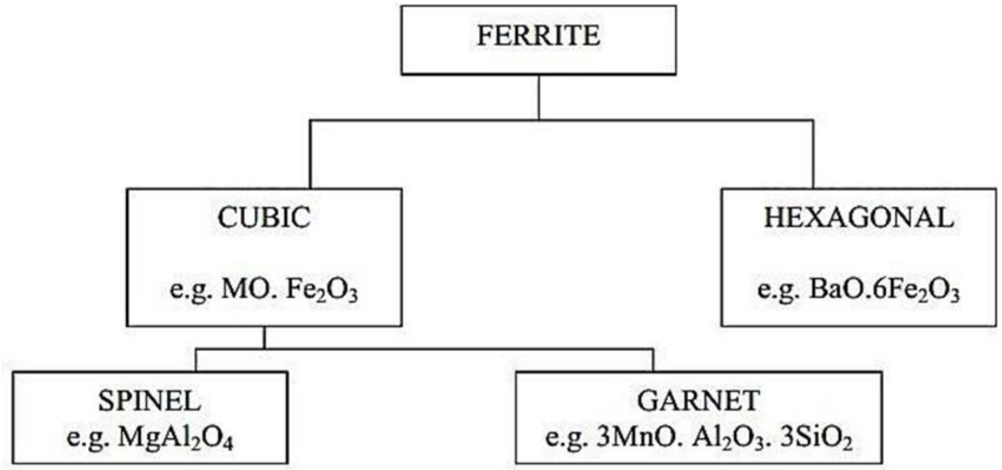

Fig. 2.1: Different types of ferrites.

The ferrites first drew the public attention when Hilpert (1909) focused on their applications at high frequency range (Suzuki, Tanaka and Ikemizu, 2001). A comprehensive research work was initiated by Snoek (1946) at Philips Research Lab (Ohta and Kobayshi,1964). Takai (1937) in Japan started serious investigation on the same materials concurrently (Suzuki, Tanaka and Ikemizu, 2001). Snoek's contribution on ferrite materials exposed many hidden mysteries of magnetic properties of ferrite. He was interested on high permeability(μ) materials of cubic structure. This specific structure supports low crystalline anisotropy due to symmetry reason. He could successfully find desired material in mixed spinel ferrite of $M_eZnFe_2O_4$ where μ were ranged up to 4000 (Suzuki, Tanaka and Ikemizu, 2001, Ohta and Kobayshi,1964, Tsunekawa et al.,1979). Now if we focus on our present study, we see the development of nickel-based ferrite materials. Ni-based magnetic spinel ferrites have been drawn attraction to researchers, investigators and a large number of applied science students due to their significant properties and varied application in technological field specially in electronics and biomedical field during the last 80 years (Cruickshank, 2003).

Ni-Cu ferrite has already shown its established position and potentiality in tech-world because of high saturation magnetization, resistivity and non-conductivity with lesser loss energy over a broader frequency range (Hossen, Nasrin and Hossen, 2020). Ni-Cu-Cd spinel ferrite, although its attention is in elemental level, generates interest in practical field due to its multiplicity scope of uses (Hankare et al., 2010). In addition, Mn substituted Ni based spinel ferrite materials shows their possibility to change structural, and electro-magnetic properties which is a strong motivation for researchers to work further on Mn substituted Ni-Cu-Cd ferrite presently.

The sintering process is also marked as an important step in preparing ferrite and often shows a dominant role in many magnetic properties. Tatarchuk et al. (2017), investigated the influence of sintering environment on magnetic properties. They observed the effect of high density on increasing permeability (Hoque, Choudhury and Islam, 2002).

2.3 Overview of Spinel Structure

Spinel ferrite is a group of magnetic materials that takes its name from the $MgAl_2O_4$ mineral named 'spinel', which occurs naturally. The spinel structure was first determined by Bragg (1915) and Nishikawa (1915). Since their discovery, these ferrites, also called 'cubic ferrites', have drawn the attention of material scientists. The general formula for the 'spinel' structure is

AB_2O_4, where A stands for a divalent cation and B for a trivalent cation. The full structural formula of spinel ferrites is AFe_2O_4, which can be defined as tightly packed cubic structures with iron as a trivalent cation (Fe^{3+}). Divalent cation (A) can be iron, nickel, zinc, cobalt, manganese, magnesium, copper, cadmium, or their combinations etc.

A spinel ferrite, MFe_2O_4 cubic unit cell has 8 formula units with 56 ions. There are 32 (8 formula units *4 ions) oxygen anions, 8 (8 formula units*1 ion) M^{2+} cations and 16 (8 formula units*2 ions) Fe^{3+} cations. As delineated by the ferrite researchers (Figure 2.2 (a), (b) and (c)), large sized oxygen ions form a closely packed face centered cubic (fcc) structure with smaller divalent metal cations occupying the interstitial positions with space group $Fd_{3m}O_k^7(227)$. The spinel unit cell maintains its electrical neutrality overall.

$$\begin{aligned}
&Charge\ on\ unit\ cell\\
&= Q_{unit\ cell}\\
&= Q_{Oxizen\ anion} + Q_{Divalent\ cation} + Q_{Ferric\ ion}\\
&= 32 \times (-2) + 8 \times (+2) + 16 \times (+3)\\
&= -64 + 16 + 48\\
&= 0
\end{aligned}$$

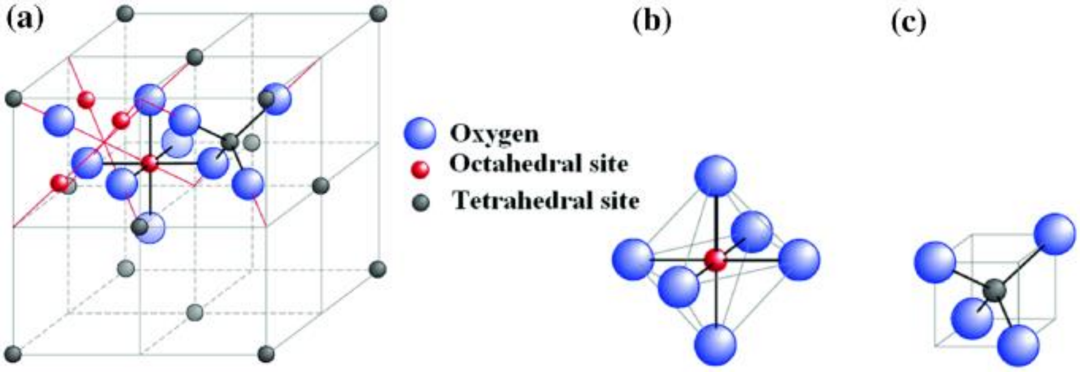

Fig. 2.2: Structure of spinel ferrite (a) formula cell, (b) B site and (c) A site.

Since, two different valence cations (+2 and +3) are available, two types of crystallographic sites are present in the spinel structure. One is the tetrahedral ‘A’ site, surrounded by four oxygen ions and the other is the octahedral ‘B’ site, surrounded by six oxygen ions as shown in Figure 2.2. There are 8 A-sites and 16 B-sites in a spinel unit cell. Ions located at the tetrahedral sites are known as ‘network formers’, while those located at the octahedral sites are known as ‘network’ modifiers. Such a structure endows the spinel ferrites with unique electromagnetic properties.

The crystal makeup of spinel ferrite is explained by formula $(Me^{2+}_{1-x}Fe^{3+}_{x})_A\,[Me^{2+}_{x}Fe^{3+}_{2-x}]_B\,O_4$, where x = 0 for normal spinel and x = 1 for inverse structure and x is called inversion parameter which varies with synthesis methods. The occupancy of larger cations and expansion of A and B sites are characterized by oxygen parameter (u) which refers to oxygen movement during the substitution process of cations. Thus, the substitution of transition metals such as Mn, Cu, Cd, Co causes significant change in physical and electromagnetic properties in spinel ferrite materials (Tatarchuk et al., 2017, Narang and Pubby, 2021). Some of the novel applications of spinel ferrite are shown in Figure 2.3.

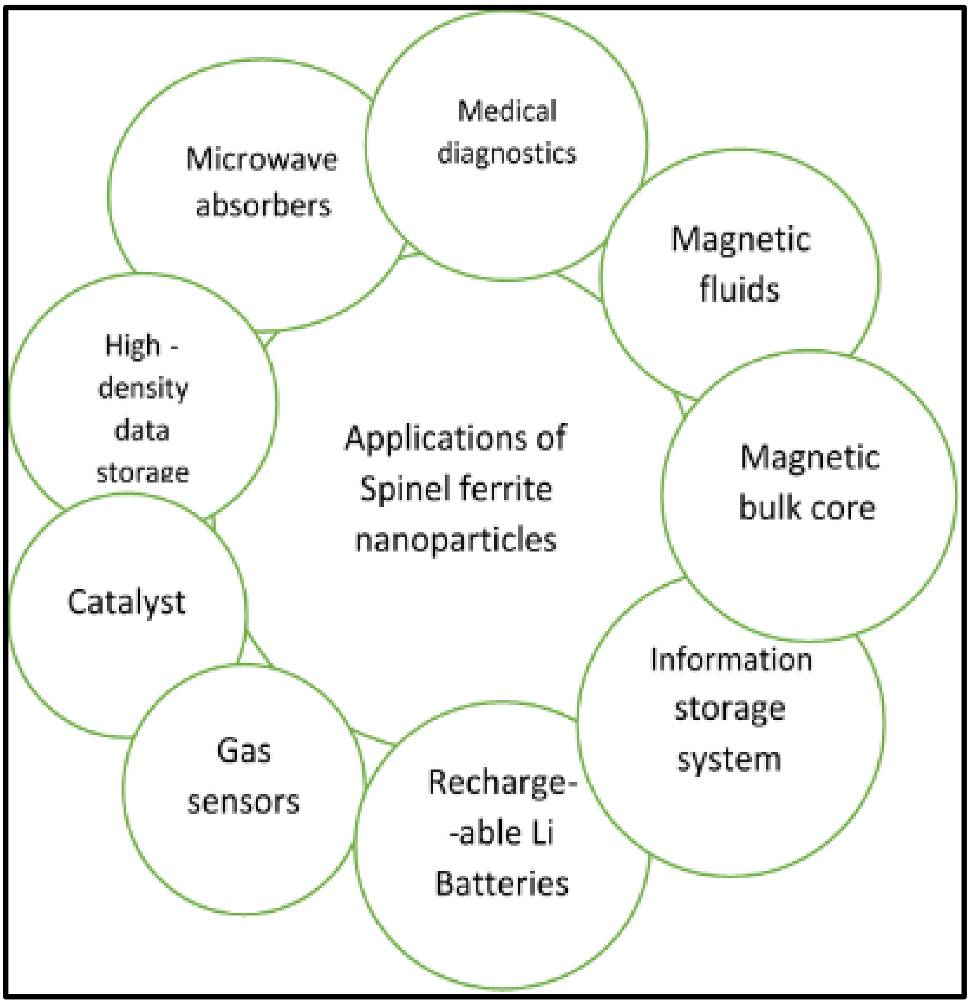

Fig. 2.3: Applications of spinel ferrite nanoparticles (Tatarchuk et al., 2017).

2.4 Methods of Compacting Nano Powders

Production of bulk or dense ceramic materials from nano powders are obtained by the methods of compacting at room temperature which possibly falls under subsequent sintering process (standard sintering and pressure induced sintering). The methods types are as follows:

i. Pressing nano powders
ii. Sintering nano powder without pressing
iii. Pressure induced sintering

In present study we applied the first case (i) and this case is only discussed here. In powder metallurgy, variety of pressing methods are used to produce high dense and porous materials. The parameters affecting density are particle size, impurity surface morphology, particle- shape and the method of pressing.

To press nano-powders following uniaxial pressing are used:

a. Static pressing (mold pressing, forging)
b. Dynamic pressing (magneto-impulse, explosive)
c. Vibration pressing (ultrasonic)

Besides, to obtained high dense homogeneous materials uniform (isostatic) pressing (hydrostatic, gasostatic and quasi-static) are used. At present extreme plastic deformation method is also used.

In case of ii type, sintering of nano powders without pressure which is also called ‘conventional sintering’ does not allow to produce a pore free small grained materials at low temperature. On the other hand, at high temperature, the grain size increases with density extension. This problem solved by high-speed microwave sintering and controlled sintering method.

In case of iii type, it is a promising method to prepare bulk nanocrystalline materials. Here a low density (30-40%) pre form is pressed, heated at oxide reduction temperature and pressed at the theoretical pressure. In this case grain size reduce significantly with sintering temperature (Lyakishev, Alymov and Dobatkin, 2003).

2.5 Review of Relevant Works

2.5.1 Synthesis of Ni-Cu-Cd Ferrites Nanoparticles

The general operational principle of producing nanoparticles is ‘the combination of a high rate of nucleation with a low rate of growth. To provide necessary environment, solutions could be different. The size distribution of particles and their structure and properties are mostly influenced by conditions of formation, synthesis route and time (Lyakishev, Alymov and Dobatkin, 2003). Therefore, it is often critical to find a particular synthesis technique to obtain the desired properties of nano-particles. Over the past few decades, several methods have been employed for synthesize high quality spinel ferrite nanoparticles, among them, co-precipitation, sol-gel auto combustion, sol-gel and solid-state reaction route (Hossen, Nasrin and Hossen, 2020), hydrothermal (Kang, 2003, Ai, Zhang and Chen, 2011) are well mentioned and have been used extensively.

Solid state method was used by many investigators (Hossen, Nasrin and Hossen, 2020, Tatarchuk et al., 2017) to prepare Ni based spinel ferrite nanoparticles. In this process, various metal oxides are mixed and calcined to obtain ferrite powders. Main disadvantages are homogeneity and mechanical mixing of oxides could hardly intimate which causes in composition fluctuation at every stage of processing. Calcination temperature is more than 750°C and sintering temperature is more than 1000°C. Chemical methods could solve the limitations of this method. Belavi *et al.* (2012) employed an ideal double sintering ceramic method to investigate $Ni_{0.95-x}Cd_xCu_{0.05}Fe_2O_4$. They reported structural properties with fine particles and semiconducting nature. They also found a variation of dielectric constant for the low and high-frequency region along with magnetic properties. Marinca et al. (2013) synthesized $Ni_{1-x}Mn_xFe_2O_4$ nano particles by heat treatment and following mechanical milling in a combined way. The crystallite size decreases with increasing milling time up to 120 minutes and particle size found less than 25 nm. They have also observed variation of saturation magnetization within the structure as shown in Figure 2.4.

Co-precipitation method was extensively employed to synthesis Ni based spinel ferrites by many researchers. It is convenient, time saving, economic with high production rate and could produce uniform-sized particles (Tatarchuk et al., 2017). In this route, aqueous solutions of di and trivalent transition metal salts are mixed together in 1:2 mole ratios in alkaline medium with a setup of continuous stirring. A careful observation on pH is must for better result.

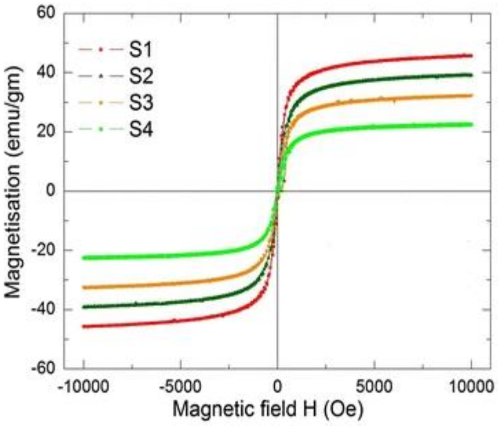

Fig. 2.4: VSM analysis of $Ni_{0.95-x}Cd_xCu_{0.05}Fe_2O_4$ ferrite.

The common disadvantage is comparatively low crystallinity and requirement of subsequent thermal treatment. Mirazaee et al. (2020) made Mn substituted Ni nano ferrite particles by using a customized co-precipitation scheme. They examined structural and magnetic properties by analyzing XRD, FESEM, FT-IR, and VSM data output. They also found spin canting following doping Mn ion. Tirupanyum et al. (2015) synthesize $Mn_xNi_{1-x}Fe_2O_4$ by this process and obtained crystalline ferrite particles with particle size of about 30 nm. They observed that crystallite size had influenced on saturation magnetization and coercivity with addition of Mn contents. Akash et al. (2016) prepared $Ni_{1-x}Mn_xFe_2O_4$ nanocrystalline ferrite powder by chemical co-precipitation method. They possess low magneto-crystalline anisotropy at a particle size of 50 nm. Khan et al. (2017) synthesized nanoplates of $M_{0.8}Ni_{0.2}Fe_2O_4$ by the co-precipitation route with side-length 8+ / -2 nm. They verified the single-phase crystalline nanoparticles with plate-like morphology.

NMCC ferrite has been also synthesized by through sol-gel auto-combustion technique due to its simplicity in process, lower cost, wide range of materials processability, refined particles, acute control on the doping level, and homogeneity (Tatarchuk et al., 2017, Thakura et al. 2020, Hossen and Hossen, 2019). A good number of investigators have used the process and observed nano-sized spherical ferrite having particle size 17-37 nm. Moazzem et al. (2020) prepared Ni-Cu-Cd ferrite by sol-gel auto-combustion route with annealing temperature at 700°C for 5hrs. They observed increased lattice constant and decreased saturation magnetization while adding Mn content. The same results were also reported by Shirsath et al. (2010) while preparing $Ni_{0.5-x}Mn_xZn0_{.5}Fe_2O_4$. Arifuzzaman et al. (2016) synthesized $Ni_{0.7-x}Cu_xCd_{0.3}Fe_2O_4$ by sol-gel auto-combustion process calcined at 550°C. They investigated physical and electrical properties at room temperature and the rising of ac conductivity with increased frequency reported. The hopping mechanism was applied to explain the phenomenon. The average crystallite size was 11 nm and 17 nm at 550°C and 700°C. Devmunde *et al.* (2016) synthesized $Ni_{1-x}Cd_xFe_2O_4$ by sol-gel method where citric acid was used as fuel at a low ignition temperature of 200-250°C. Particle's size was counted in the range of 46-58 nm.

Batoo et. al. (2009) investigated the finite size effect and influence of temperature on electrical properties of nanocrystalline Ni–Cd ferrites. They successfully synthesized single-phase polycrystalline cubic spinel $Ni_{0.2}Cd_{0.3}Fe_{2.5x}Al_xO_4$ with an average crystallite size of 5 nm through sol-gel technique. Complex impedance spectra showed only one semi-circle corresponding to the grain boundary volume suggesting that contribution to the conductivity is solely by grain boundary volume. The ac conductivity is found to increase with increase in grain size. The dielectric constant and loss tangent both showed normal behavior with respect to frequency. This technique yields single phase spinel type cubical structure of ferrites.

The solvo-thermal method (or Hydrothermal if water is used) is another eco-friendly synthesis route where aqueous or non-aqueous solvents are used with better control on particle size (Tatarchuk et al., 2017). A wide range of spinel ferrites have been synthesized with it e.g., $MgFe_2O_4$.

Sol-gel auto-combustion method has been proved to be best one due to its simplicity in process and economic way to produce nano scale ferrite powder with high purity. Nano crystalline structured material offer novel properties. By proper modifying and tuning of the particle size it is possible to optimize the expected properties like structural, physical, electromagnetic etc. (Das et al., 2009).

2.5.2 Effect of Substitution by Divalent Cation

A good number of researchers are working on the enrichment of physical and electro-magnetic properties of ferrites with the process of substitution and doping by divalent ions. In a general sense, the divalent metal ions (which is denoted by M_e^{2+}) i.e., Ni, Zn, Cu, Mg, Mn, Cd, Co, or mixtures of these act as substituent or dopant and are also substituted in different spinel ferrites

Usually, these substitutes maintain a critical characteristic which is known as "site occupancy" or "site preference" in between two sites i.e., Tetrahedral-A site and Octahedral-B site in the spinel structure. All of them have different site affinity towards A and B site and significantly contribute in changing the properties by modifying cation distribution in crystal structure. The influence of M_e^{2+} substitution over the electro-magnetic properties is studied basing on two important factors i.e., site preference of M_e^{2+} ions and the strength of exchange interaction among magnetic ions. The influence of divalent substitution in NiCuCd and some Ni based ferrite are reviewed bellow:

Shirsath et al. (2010) investigated Mn ion influence while preparing $Ni_{0.5-x} Mn_xZn0_{.5}Fe_2O_4$ at 600°C temperature. They have observed increased lattice constant and decreased saturation magnetization with addition of Mn ion. Same result was also observed by Moazzem *et al.* (2020) prepared Ni-Cu-Cd ferrite by sol-gel auto-combustion route with annealing temperature at 700°C for 5 h.

Devmunde et al. (2016) synthesized $Ni_{1-x}Cd_xFe_2O_4$ by sol-gel method and examined the influence of Cd^{2+} (nonmagnetic) ions over Ni^{2+} and Fe ions (magnetic). They observed frequency-dependent dielectric properties. It was also seen that magnetic parameters decrease as a function of Cd content.

Hussain et al. (2013) synthesized $Ni_{1-x}Mn_xFe_2O_4$ applying sol-gel auto combustion process and they also examined similar modification in the lattice parameter with increase manganese content the same as Shirsath *et al*. (2010).

Manjura et al. (2002) worked on the structural and electro-magnetic properties of $Ni_{1-x}Cu_xFe_2O_4$ nanoparticles by sol-gel technique and examined the effect of Cu on electromagnetic characteristics. Pandav et al. (2016) observed the alteration in the structural and magnetic properties of $NiFe_{2-x}Mn_xO_4$ ferrite with the substitution of Mn ion.

Zn^{2+} is used to improve electro-magnetic properties as well as densification in ferrite. It is substituted in spinel ferrite to increase magnetization. It also lowers magnetostriction and anisotropy in ferrites. Cu is also conventionally used in NiCuZn ferrite to improve densification, electrical resistivity and saturation magnetization (Roy, Nayak and Bera, 2008).

S. K. Nath et al. (2012) investigated the magnetic ordering of Ni-Cd ferrite along with substitution of Cd ion. XRD results indicate the single phase of pure cubic spinel structure. The magnetic moment increases with Cd content up to $x = 0.3$ at room temperature and thereafter decreases.

Many researchers work on Mg substitution in different ferrite systems and found it significant changes on structural, electrical and magnetic properties. Besides MgO is also a stable oxide which frequently used in different electronics applications. Mg ion substitution and its effect on structural and electrical properties along with magnetic properties of $Ni_{0.5-x}Mg_xCu_{0.2}Cd_{0.3}Fe_2O_4$ was studied by Moazzam et al. (2019). They found lattice constant, grain resistance, and grain boundary resistance increases with the substitution of Mg^{2+}. A rise of ac conductivity is also observed with increasing frequency. Akash et al. (2016) observed $Ni_{1-x}Mn_xFe_2O_4$ sample possess low magneto-crystalline anisotropy due to substitution of Mn ion.

2.6 Origin of magnetism in spinel ferrite

Magnetism originates from the number of unpaired spins in electron. In spinel ferrite lattice, cations are separated by O^{2-} ions which has zero magnetic moment due to its filled shells with p-type orbitals. Ni^{2+} (d^8), Cu^{2+} (d^9), Cd^{2+} (d^{10}), Mn^{2+} (d^5) and Fe^{3+} (d^5) cations of the ferrite have 2, 1, 0, 5, and 5 unpaired electrons respectively. As a result of unfilled 3d sub shell of divalent Ni, Cu, Mn, and trivalent Fe ions, have magnetic moments. But Cd ion by contrast is diamagnetic due to filled outer sub shell.

As in ferrite structure, cations are intervened by oxygen, cation-cation direct interaction s are negligible. When cations are bonded covalently to oxygen, p-orbital of oxygen interact with d-orbital of cations with; C-↑-↓-O-↑-↓-C (where C is for cation and O is for oxygen) anti-parallel spins of cations. This indirect interaction is called ‘super exchange’ interaction. There could be three types of interactions: A-O-A, B-O-B, and A-O-B. `Out of them, A-O-B is significantly strongest in nature. Since the unpaired electrons number vary in different cations, the total magnetization i.e. moment / unit volume is caused from the difference between the magnetic moments of A-sites and B-sites. This magnetism is known as ferrimagnetism and NiCuCd bulk ferrite is a ferrimagnetic material.

Further, the magnetic properties of ferrite could be modified through substitution process by proper distribution of cations among tetrahedral and octahedral lattice sites. In present study, Ni is substituted by Mn. When Mn is substituted for Ni, there would be a several migration occurrences among Fe^{3+} and other transitional divalent cations with a proportionate in between A-site and B-site which results significant change in saturation magnetization (Roy, Nayak and Bera, 2008).

CHAPTER 3
SYNTHESIS PROCEDURE

3.1 Introduction

The general formula of Mn substituted NiMnCuCd ferrite is $Ni_{0.5-x}Mn_xCu_{0.2}Cd_{0.3}Fe_2O_4$ (NMCCFO) where x = 0.0, 0.1, 0.2, 0.3, 0.4 and 0.5. The following compositions were synthesized, characterized and discussed all through.

- $Ni_{0.5}Cu_{0.2}Cd_{0.3}Fe_2O_4$
- $Ni_{0.4}Mn_{0.1}Cu_{0.2}Cd_{0.3}Fe_2O_4$
- $Ni_{0.3}Mn_{0.2}Cu_{0.2}Cd_{0.3}Fe_2O_4$
- $Ni_{0.2}Mn_{0.3}Cu_{0.2}Cd_{0.3}Fe_2O_4$
- $Ni_{0.1}Mn_{0.4}Cu_{0.2}Cd_{0.3}Fe_2O_4$
- $Mn_{0.5}Cu_{0.2}Cd_{0.3}Fe_2O_4$

3.2 Synthesis Techniques

In the present study, the sol-gel auto-combustion technique was employed to synthesis samples of $Ni_{0.5-x}Mn_xCu_{0.2}Cd_{0.3}Fe_2O_4$ (x = 0.0, 0.1, 0.2, 0.3, 0.4 and 0.5) mixed nanocrystalline ferrite powders. This process which is also called “self-propagating synthesis” was first coined by a Russian named Merzhanov (Nersesyan, Peresada and Merzhanov, 1998).

3.2.1 Sol-gel auto-combustion method

The sol-gel auto-combustion synthesis process is a renowned route to form novel nanoparticles and nano composites. It has significant dominion on the textural and surface properties of the material. Moreover, this sol-gel route has the advantages of lower cost precursors, low external energy consumption, simplicity in preparation process, non-toxicity as well as simple apparatus requirement that produce nano-sized, homogeneous, fine crystalline powders. A comparative state of different synthesis routes is given in Table 3.1.

Table-3.1: Comparative state of major synthesis methods (Tatarchuk et al., 2017, Thakura et al. 2020, Hossen and Hossen, 2019)

Synthesis Techniques	**Temperature (°C)**	**Advantages**	**Disadvantages**
Coprecipitation technique	30-140	• Easy method • Low cost • Control on size • High mass production	• Low crystallinity • Extended reaction time • Additional thermal treatment
Hydrothermal	100-200	• Eco friendly • Scalable • Controlled on particle • Simplicity	• Special Reactor needed • High pressure needed • Long reaction time
Conventional Solid-state reaction technique	-140 to 200	• The toxic-free and cheap solvent used • Simple and economically viable	• Formation of toxic waste products • Not suitable for mass production
Sol-gel	20-200	• Simplicity in process • Lower cost • Wide range of materials processable • Refined particles • Acute control on the doping level • Homogeneity	• Thermal treatment for high purity

Combustion process provides a unique synthesis technique through which a strong exothermic redox reaction is occurred between nitrate salts and organic fuel to obtain multi element oxides. In this process, the auto-combustion reaction itself supplies the necessary energy instead of using a high temperature furnace. Mainly, sol-gel process undergoes in few steps to provide the resultant metal oxide protocol and those are hydrolysis, condensation and drying process. Figure 3.1 shows the process briefly but a flow chart is given in Figure 3.5 to explain the total process elaborately.

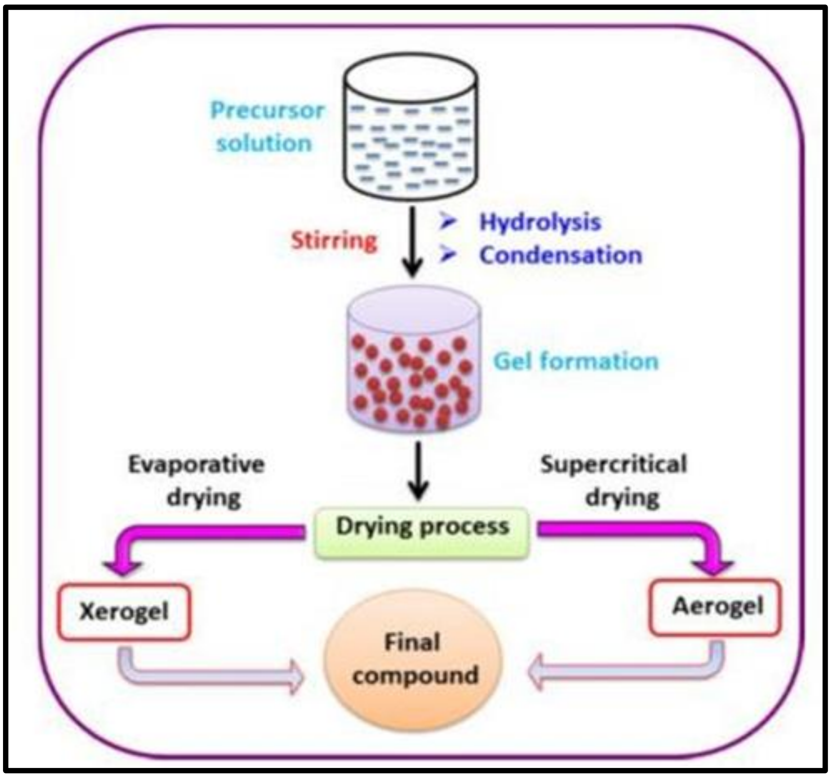

Fig. 3.1: Block diagram of Sol-Gel process.

3.2.2 Raw materials and its weighting

Commercially available nitrate salts of Merck Germany: nickel nitrate hexahydrate ($Ni(NO_3)_2 6H_2O$) (99.8%), manganese nitrate hexahydrate ($Mn(NO_3)_2 6H_2O$) (99.5%), copper nitrate trihydrate ($Cu(NO_3)_2 3H_2O$) (99.7%), cadmium nitrate tetrahydrate ($Cd(NO_3)_2 4H_2O$) (99.5%), and ferric nitrate nonahydrate ($Fe(NO_3)_3 9H_2O$) (99%) were taken as precursor materials. The mass calculation of all the NMCCFO samples with different Mn contents are shown in Table 3.2.

Table 3.2: Compositions of NMCCFO.

Mn content, x	Composition	**$Ni(NO_3)_2$ $.6H_2O$**	**$Mn(NO_3)_2$ $.6H_2O$**	**$Cu(NO_3)_2$ $.3H_2O$**	**$Cd(NO_3)_2$ $.4H_2O$**	**$Fe(NO_3)_3$ $.9H_2O$**
0.0	**$Ni_{0.5}$ $Cu_{0.2}$ $Cd_{0.3}$ Fe_2O_4**	11.5639	0.0	3.8430	7.3603	64.2625
0.1	**$Ni_{0.4}Mn_{.1}Cu_{0.2}Cd_{0.3}Fe_2O_4$**	9.2649	2.28633	3.8488	7.3713	64.3586
0.2	**$Ni_{0.3}Mn_{.2}Cu_{0.2}Cd_{0.3}Fe_2O_4$**	6.9591	4.5795	3.8545	7.3531	64.4550
0.3	**$Ni_{0.2}Mn_{.3}Cu_{0.2}Cd_{0.3}Fe_2O_4$**	4.6463	6.8796	3.8603	7.3935	64.5517
0.4	**$Ni_{0.1}Mn_{.4}Cu_{0.2}Cd_{0.3}Fe_2O_4$**	2.3266	9.1866	3.8661	7.4046	64.6487
0.5	**$Ni_{0.0}Mn_{.5}Cu_{0.2}Cd_{0.3}Fe_2O_4$**	0.0	11.5042	3.8719	7.4157	64.7459

3.2.3 Instruments

The apparatus required to produce Mn substituted NMCCFO dense bulk ferrite from nanoparticles are balance, stirrer, mortar and pestle, crucibles, furnaces, dies, hydraulic press, ceramic tray etc. All these instruments are available at the Department of Physic, CUET.

Fig. 3.2: Apparatus related to Sol-gel process.

3.2.4 Synthesis of nanocrystalline powder

To obtain “sol” (a colloidal or a molecular suspension form), a homogeneous mixture was prepared by dissolving a stoichiometric proportion of analytic grade nitrate salts (precursor mentioned above materials) in ethanol (C_2H_6O). A magnetic stirrer was employed for continuous stirring, and pH value was maintained seven by adding ammonia solution. This sol was kept on a hot plate at 70°C to transform into xerogel under constant stirring. Further burning up to 200°C temperature in the air caused the explosion of dried gel, and consequently, soft loose ferrite nanocrystalline powder was produced through a self-ignition process. Product nano powder was calcined at 700°C, which lasted five h, and the rate of heating-cooling was 10°C and 5°C per minute, respectively.

Fig. 3.3: Nano-powder of pure and Mn substituted NMCCFO.

3.2.5 Milling, annealing, pressing and sintering

Calcination is the process in which appropriate number of mixture-materials is transformed into required crystalline phase with a thermal treatment. In this process high temperature is raised under certain restricted supply of oxygen without melting the product elements. The main purpose of calcination is to remove unwanted air molecules and impurities by evaporation.

On the other hand, sintering is also a heat treatment process which is occurred at a higher temperature than calcination. Sintering is applied for better densification and its temperature is lower than melting point. Different sintering temperatures produce different grain size. Homogeneous and compact solid are obtained after sintering. In our case, calcination was occurred at 700°C and time was taken 5 hours. Besides, sintering temperature was 1200°C for another 5 hours.

In hand milling method, mortar and pestle are used for grinding the samples. In the present case, after calcination at 700°C the product powders were crushed for 3 hours in mortar to obtain fine particles. Before sintering, again the powdered samples were mixed with binder and then granulated by mortar and pestle (hand milling) for 30 minutes.

In the process of compaction, the NMCCFO samples of calcined nano powders were converted to pallet and toroid by pressing with hydraulic press.

3.2.6 Bulk sample preparation

The resultant calcined ferrite powder was milled by hand in a mortar for 3 hours to form fine particles. In addition, for granulation, the powder was blended thoroughly with a proper amount of 5 wt% polyvinyl alcohol (PVA) for 30 min (as a binder). After that, the granulated ferrite particles were uniaxially pressed with a hydraulic press to form desired shape samples. The pressure for toroid-shaped and pallet-shaped specimens was 1600 psi and 6000 psi, respectively. The samples were then sintered at 1200°C in an electrical furnace for 5 hours, where the heating -cooling rate was 10°C and 5°C per minutes, respectively. The surfaces of the product samples were polished with both rough and fine grinding papers. Finally, finished product were produced for further investigations.

Fig. 3.4: Bulk samples of pure and Mn substituted NMCCFO.

A flow chart of the synthesis process is given in Figure 3.5. The specimen in this experiment was prepared by following two stages.

Stage-1

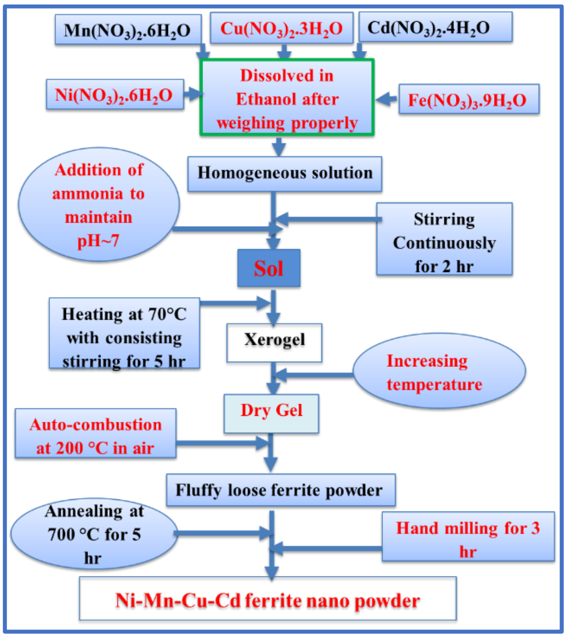

Stage-2

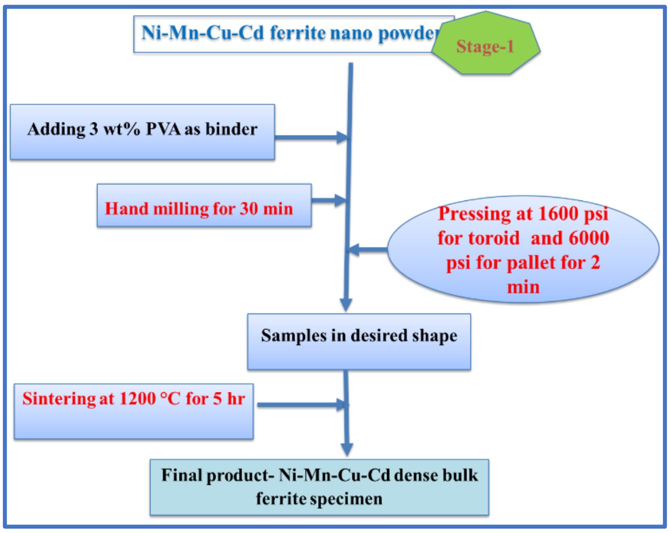

Fig. 3.5: Flaw chart for preparation of different NMCCFO compositions from nanoparticles with sol-gel auto-combustion technique.

CHAPTER 4
EXPERIMENTAL TECHNIQUES

In this chapter we describe basic experimental techniques to measure different parameters. X-ray Diffraction was used to determine the crystal structure and lattice parameters. Surface morphology and microstructure measurements were carried out by Field Emission Scanning Electron Microscopy. Elemental analysis was done by Energy Dispersive X-ray (EDX). Saturation magnetization measurements were carried out using Vibrating Sample Magnetometer. Impedance Analyzer with frequency range of 100 Hz-100 MHz was employed to investigate dielectric properties along with dielectric loss and other responses of electrical parameters. Different essential equations for measuring structural, magnetic and electrical properties are also given below.

4.1 Structural Characterization

4.1.1 X-ray diffraction

The X-ray diffraction (XRD) technique is used for the structural/phase analysis of the material under investigation by employing Philips X'Pert Pro diffractometer using CuKα wavelength, λ =1.54 Å.

The basic principle is that for a fixed wavelength (λ), the constructive interference occurs for a fixed set of an interplaner spacing (d) and incidence angle (θ) (Fig. 4.1). According to Bragg's condition of diffraction:

$$n\lambda = 2d sin\theta \qquad (4.1)$$

where *d* is the distance between crystal planes and *n* is the positive integer which represents the order of reflection. Equation (4.1) is known as Bragg law. This Bragg law suggests that the diffraction is only possible when $\lambda \leq 2d$ (Cullity, 1959). For this reason, we cannot use the visible light to determine the crystal structure of a material. The X-ray diffraction (XRD) provides substantial information on the crystal structure.

For cubic spinel structure, lattice parameter is measured by

$$na = d\sqrt{h^2 + k^2 + l^2} \qquad (4.2)$$

where h,k,l are called Miller indices. This technique is primarily used for phase identification of crystallize material and provide information related to unit cell dimension.

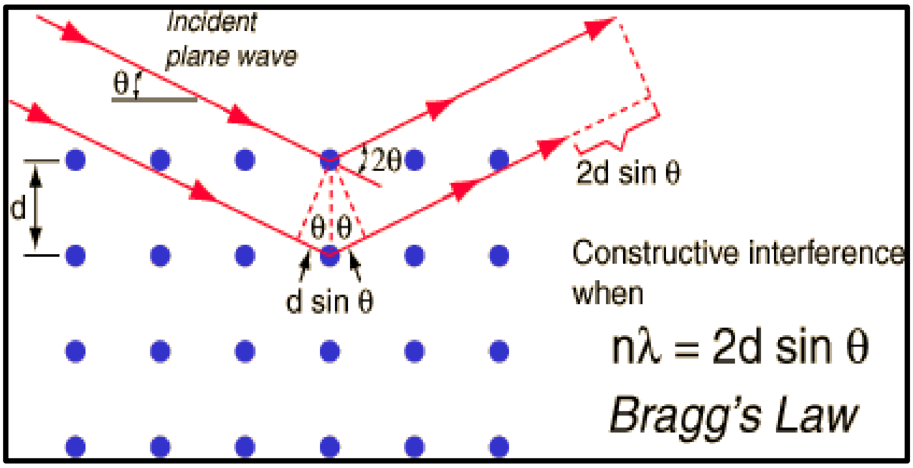

Fig. 4.1: Bragg's law of XRD.

4.2.2 Philips X'Pert pro diffractometer

Figure 4.2 is the photography of X'pert pro diffraction system. It is employed for various application of diffraction ranges starting from routine work to in depth research analysis. It is programed with software from Philips. In XRD analysis, a range of diffraction angles are calculated from the reflected X ray beams off (with specific wavelength) from parallel atomic planes. All the mechanism of the system is set to produce a peak on "diffractogram", Just like 'fingerprint' which identify the minerals with its own set of peaks.

Fig. 4.2: Philips PW 3040 X pert pro XRD.

The specification of the diffractometer is:

1. **XRD source**: 3 kW copper tube
2. **Software and database**: Pro-Fit line analysis software, X'Pert Plus analysis software (with Rietveld Capability), data collector.
3. **Apparatus statistics**: The machine uses Cu K alpha with wavelength of 1.54 Å. A 40 kilo-volt 45 milli-amp X-ray tube is used for common analysis. Slits of various dimension are applied e.g. 0.04 degree soller slit, 1 degree divergence and anti-scatter slits, ½ degree and ¼ degree receiving slits etc.
4. **Temperature capacity**: Anton-par 77-725 K and 300-1475 K cameras.
5. **Detectors**: Xe proportional counter and SS X'cellerator.
6. **Objectives**: PreFix optics, programmable slits and monochromator**.**

4.2.3 Crystallite size measurement

Crystallite size (D)**:** Measuring the size of particle has wide implications in property analysis of ferrite nanocrystalline Materials.

$$D = \frac{0.9\lambda}{\beta\cos\theta} \tag{4.3}$$

here λ is the wavelength of X-ray whose value is 1.54 Å, θ and β are Bragg's angle and the full width at half maxima value respectively. This equation is called Scherrer's formula and used to calculated particle size from XRD peak graph (Cullity, 1959).

4.2.4 Lattice parameter, bond length, and hopping length

Lattice constant (a): Both *experimental and theoretical lattice constants* were measured by the following formula (Hossen, Nasrin and Hossen, 2020):

Experimental lattice constant, $a_{exp} = \frac{d_{hkl}}{\sqrt{h^2+k^2+l^2}}$ (4.4)

Measurement of bond length and ionic radii: Standley's relations have been employed for estimation (Standely, 1972):

$$Tetrahedral\ bond\ length,\quad A-O=\left(u-\frac{1}{4}\right)\mathrm{a}\sqrt{3} \qquad (4.5)$$

$$Octahedral\ bond\ length,\quad B-O=\left(\frac{5}{8}-u\right)\mathrm{a} \qquad (4.6)$$

$$Ionic\ radius\ of\ A-site, r_A=\left(u-\frac{1}{4}\right)\mathrm{a}\sqrt{3}-R_O \qquad (4.7)$$

$$Ionic\ radius\ of\ B-site, r_B=\left(\frac{5}{8}-u\right)\mathrm{a}-R_O \qquad (4.8)$$

where u is the O_2 ion parameter having ideal value for spinal ferrite = 3/8.

Hopping Length measurement: The Hopping length was determined by following equation (Mirzaee, Shayesteh and Mahdavifar 2014):

$$L_A=\mathrm{a}\left(\frac{\sqrt{3}}{4}\right) \qquad (4.9)$$

$$L_B=\mathrm{a}\left(\frac{\sqrt{2}}{4}\right) \qquad (4.10)$$

4.2.5 Determination of theoretical lattice constant

Theoretical lattice constant, $a_{th}=\frac{8}{3\sqrt{3}}\left[(r_A+R_0)+\sqrt{3}\ (r_B+R_0)\right]$ (4.11)

where ionic radius of oxygen, R_0= 1.32 **Å**. The values of r_A and r_B were calculated from cation distribution.

4.2.6 Density and porosity

Experimental density (ρ_{exp}) measurement (Bulk density): The bulk density of was measured by using the formula:

$$\rho_{exp}=\frac{mass}{volume} \qquad (4.12)$$

The theoretical density (X-ray density) $\rho_x$was calculated using following expression:

$$\rho_x = \frac{ZM}{N_A V} \ g/cm^3 \qquad (4.13)$$

where M is the molecular weight, Z is the number of molecules per unit cell (Z = 8), N_A is the Avogadro's number (6.02×10^{23} mol^{-1}), V is the unit cell volume. (For cubic cell V= a^3; for tetragonal cell V = a^2c and for orthorhombic cell V = abc, where a, b and c are the lattice parameters).

The porosity was calculated from the relation (Cheng,1999).

$$P(\%) = \left(1 - \frac{\rho_{exp}}{\rho_x}\right) \times 100 \qquad (4.14)$$

where ρ_{exp} is the bulk density and $\rho_x$is the theoretical density.

4.3 Data Analysis by Reitveld refinement method

Rietveld technique was adopted for structure refinement using XRD data and Fullprof Suite software package was used to process data for analysis. XRD patterns were analyzed under Pseudo Voigt peak shape in Fd-3m space group and background was also refined. Diffraction patterns, cation distribution, electron density and maximum entropy map (MEM) were studied and analyzed precisely. Moreover, Vesta software was utilized for forming crystal structures of investigated ferrite samples.

4.4 Morphological Characterization

The study of microstructure is necessary to obtain a deeper image of grain structure. For this purpose, the sintered NiCuCd ferrite and its substituted samples were used. In present study, the microstructure was examined by field emission scanning electron microscope (FESEM), where an electron beam with prob was used to create images at 5 kV. Originally the experimental data were collected from FESEM, (JEOL JSM 7600F, Japan) at BCSIR Laboratories, Dhaka. The average grain diameter (size) of the samples were measured by linear intercept method where photo-image of FESEM were used. Besides, the EDX study was introduced to analyze chemical makeup of the sample where the accelerating voltage was at 10 kV.

4.4.1 Field Emission Scanning Electron Microscope (FESEM) and its function

The electron microscope in short EM is one of the very routinely applied investigative tools in the field of surface characterization in micro/nanomaterials. The major steps belong to all EMs regardless of variety are as follows:

- Generation of primary electron stream from a source and acceleration towards an anode under vacuum.
- Transforming stream of electron into narrow and focused beam passing through condenser lens (actually electro-magnet).
- Striking of fine electron beam over the sample passing through magnetic objective lens where beam act as scanning beam.
- Interaction of primary beam with sample in different ranges of energy which is detected as electric signal and ultimately results as image production.

Basically, Field Emission Scanning Electron Microscope (FESEM) is an advanced technology applied to create the micro or nanostructure image. It is more capable than SEM in terms of resolution (1 nm VS 50 to100 nm in order) and focusing in depth permits the former one more 3D information provider than the latter.

In a typical FESEM, an electron beam is produced from a field emission source and a high vacuum environment is kept to avoid disturbance of gas molecules interaction with electron beam. The emitted electrons are accelerated with electric potential range of 0.5V to 30 kV towards the samples. These primary electrons are transformed into fine narrow scanning beam after passing through a series of electromagnetic lenses (condenser, scan coil, objective lens etc.) which is ultimately undergoing interaction with the solid sample. The affect of interaction is the result in emission of Secondary e^- (SE), backscattered e^- (BE), X-ray excitation beam, Auger electron, cathode luminescence and electron transmission. A detector collected SEs and converts them into electric signals which in process amplified and transform into digital images for further investigation. A schematic diagram is shown in Figure 4.3.

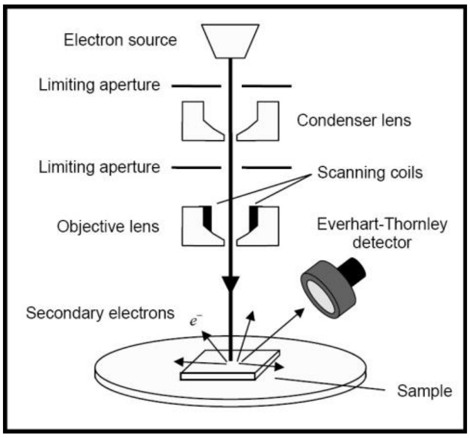

Fig. 4.3: Schematic diagram of FESEM.

4.4.2 Energy dispersive X-ray (EDX) spectroscopy

EDX was examined on the same samples to identify the elemental composition. In addition to FE-SEM instrument, these systems are attached within. The basic principle of EDX was first observed by Mosely to identify composition. He found the changes of X-ray frequency emitted from different elemental targets which also varied linearly with atomic number.

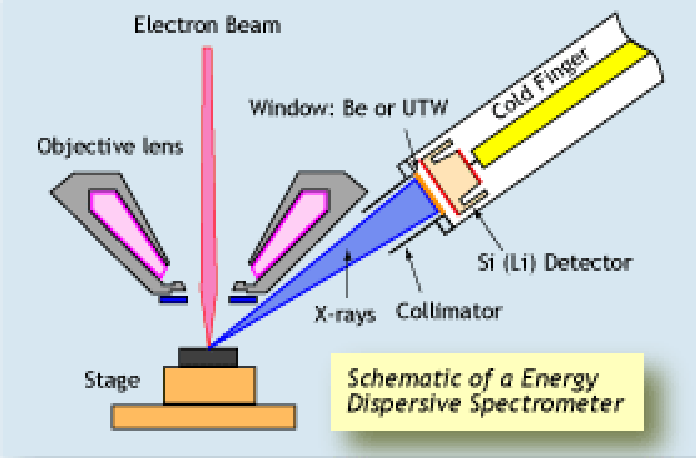

Fig. 4.4: Schematic diagram of EDX.

4.5 Electric and Dielectric Properties Measurement

The data of different parameters such as dielectric constant, loss tangent, electric modulus, complex impedance and ac conductivity for studied ferrite samples have been collected as a function of frequency by using WK (Wayne-Kerr) model- 6500B Impedance Analyzer. In all cases, the frequency ranges were maintained between 100 Hz to 100 MHz at room temperature. Disk-shaped samples with thickness about 0.16 cm - 0.18 cm and radius about 0.60 cm - 0.61 cm were used in the experiment.

Dielectric constant ($\varepsilon^{/}, \varepsilon^{//}$): Permittivity is a measure of how an applied electric field affects and affected by a dielectric material. Dielectric constant or relative permittivity is an important tool to explain the characteristics of ferrite as multifunctional material. Dielectric permittivity is often treated as a complex function of the frequency of the applied field. Following equations are used to calculate dielectric parameters (Bagum, Hossen and Chowdhury, 2016):

$$\varepsilon^{*} = \varepsilon^{/} - j\varepsilon^{//} \tag{4.17}$$

$$Real\,part\,, \varepsilon^{/} = \frac{C_p\, t}{\varepsilon_o A} \tag{4.18}$$

where C_p, t, A and ε_o are capacitance, thickness, cross-sectional area and permittivity in vacuum respectively. The value of ε_o is 8.854×10^{-4} F/cm.

Loss Tangent (tan δ) is calculated from the following equation (patil et al., 2019):

$$tan\delta = \frac{\varepsilon^{//}}{\varepsilon^{/}} \tag{4.19}$$

here, $\varepsilon^{/}$ explains stored energy in materials and $\varepsilon^{//}$ is the imaginary part which express energy loss.

Electric modulus ($M^{/}$, $M^{//}$): The frequency dependent electric modulus can be calculated through the expressions (Zulqarnain et al., 2021):

$$M^{*}(f) = M^{/} + jM^{//} = \frac{1}{\epsilon^{*}} \tag{4.20}$$

$$M^{/} = \omega C_g X \tag{4.21}$$

$$M^{//} = \omega C_g R \tag{4.22}$$

where geometrical capacitance $C_g = \frac{\varepsilon_o A}{d}$ and ω is angular frequency.

Impedance ($Z^{/},\ Z^{//}$) : The impedance is a more general circuit parameter which estimates the ability of a circuit to resist the flow of electrical current. Following equations were used to calculate the impedance parameters:

$$Effective\ \ resistance\ , Z = Z^{/} + jZ^{//} \tag{4.23}$$

$$Resistance\ , Z^{/} = |Z| \cos\theta \tag{4.24}$$

$$Reactance\ , Z^{//} = |Z| \sin\theta \tag{4.25}$$

where θ is phase shift.

AC conductivity (σ): Conductivity acts as a measuring tool for the analyzing of density and porosity (Blum, 1958). Following formula was used to express the frequency dependent ac conductivity of a ferrite bulk ceramic samples.

$$\sigma_{ac} = \varepsilon^{/}\varepsilon_0 \omega tan\delta \tag{4.26}$$

where ω is the angular frequency .

4.6 Magnetization measurement

Magnetic moment per unit volume is called magnetization. It can be measured with different methods. In this present study, the vibrating sample magnetometer (VSM) was used for magnetization measurement at room temperature. This VSM was first introduced by S. Foner in 1956 and well accepted as standard approach by worldwide due to its simplicity and relatively high sensitivity in the study of low temperature and high magnetic field. The basic functional principle of VSM is founded on Faraday’s law of induction. In a typical VSM, a vibrating rod is placed in a static and uniform magnetic field. The magnetic sample is usually attached to this rod and allowed to vibrate at a constant frequency. Finally, the induced electro motive force by the sample is measured as voltage signal through a process of amplification. The resultant induced signal is directly proportional to the magnetization of the specimen. It is also independent of external field intensity. A block diagram and picture are shown in Figure 4.5 and 4.6.

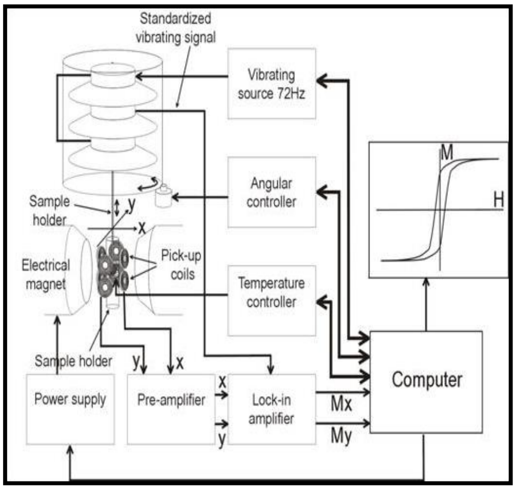

Fig. 4.5: Block diagram of VSM.

Fig. 4.6: Vibrating Sample Magnetometer (VSM).

4.6.1 Magnetic moment and anisotropy constant calculations

In the present study significant changes have been observed in magnetic properties due to the substitution of Mn^{2+} in NiCuCd bulk ferrite sintered at 1200°C. VSM testing of all the samples was done at room temperature (VSM, Lakeshore 7400 series) to record magnetisation data and magnetic flux density. These measuring data were collected at Atomic Energy Commission, Dhaka. Besides, magnetisation curves were also analysed by the Law of Approach to Saturation (LAS) method, widely applied on polycrystalline soft ferrite. The magnetic moment (μ_B) has been measured with the following formula:

$$\mu_B = \frac{M \times M_S}{5585} \tag{4.15}$$

where M and M_s are molecular weight and saturation magnetization, respectively. The anisotropy constant has been computed through the equation:

$$K_1 = \frac{M_s \times H_c}{2} \times 10^4 \left(\frac{erg}{cm^3}\right) \tag{4.16}$$

CHAPTER 5
RESULTS AND DISCUSSION

5.1 Introduction

The dense $Ni_{0.5-x}Mn_xCu_{0.2}Cd_{0.3}Fe_2O_4$ (NMCCFO, x = 0.0, 0.1,0.2, 0.3,0.4, and 0.5) bulk compositions were prepared by the sol-gel auto-combustion technique and were sintered at 1200°C with the duration of 5 hours. XRD and FESEM were used to carry out the structural analysis and surface morphology. The effects of microstructure and sintering temperature on the properties of NMCCFO were studied. A possible correlation between grain size, density and porosity were also discussed. MEM analysis was introduced to observe electron density. The dielectric and electrical properties of these compositions were measured at room temperature in the frequency range 100 Hz to 100 MHz with Impedance Analyzer. Electrical properties of all the compositions were studied by complex impedance plot and analyzed by the Cole-Cole plot. VSM was applied to investigate the M_s and LAS was used to calculate anisotropy constant as well as M_s results theoretically for critical analysis.

5.2 XRD study of *NMCCFO*

The XRD pattern is the structural fingerprint that figures out the atomic arrangement in the sample elements. Figure 5.1 (a) shows the XRD spectrum of various $Ni_{0.5-x}Mn_xCu_{0.2}Cd_{0.3}Fe_2O_4$ samples within the range from 20° to 70°. In investigating the plots, the results reveal that the peaks are at (220), (311), (222), (400), (422), (511) and (440) which confirms the presence of single-phase cubic spinel ferrite structure with no trace of impurity peaks in all the samples. This reflects homogeneity and purity of the product samples which also indicates complete dissolution of Mn into NMCCFO. Peaks are confirmed by XRD card – JCPDS no-019-0692 (Hossen, Nasrin and Hossen, 2020).

The magnified plot of XRD peak at the (311) are shown in Figure 5.1 (b). It is observed that with the addition of Mn content, the peaks of XRD get broader. The broadened peak pattern confirms the fine particle nature of the studying specimens in the nano-scale range. It is also noticed from the graph that within 35° to 36° of the position, 2θ, highest intense planes are seen which confirms the formation of ferrite structure. Moreover, the positions of the peaks are shifted towards lower angles with the increase of Mn content. This is due to the increase in d-spacing caused by the internal stress in lattice constant which is explained in different scientific literature (Cheng et al., 1999, Rezlescu et al., 1994).

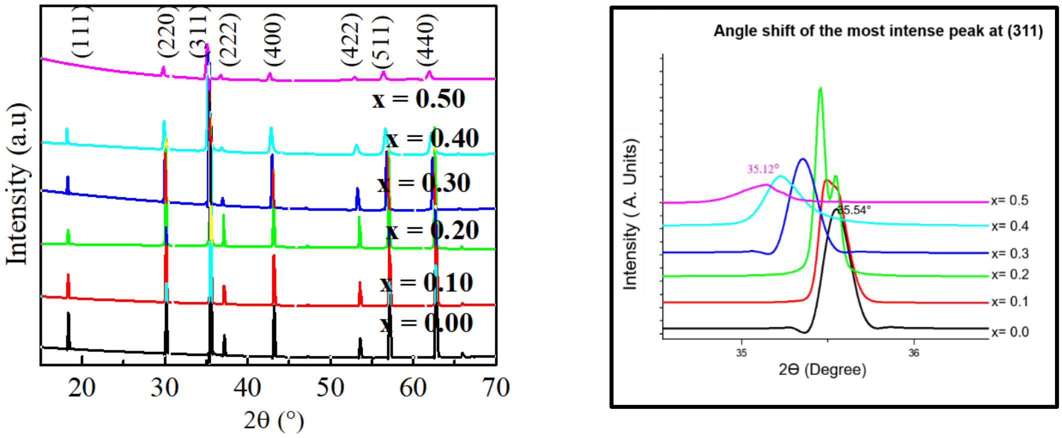

Fig. (a)

Fig. (b)

Fig. 5.1: (a) XRD spectra of *NMCCFO* for different Mn contents and (b) Magnified XRD spectra of the most intense peak at (311) of *NMCCFO* for different Mn contents results between 35° to 36°.

The crystallite size value was measured with the help of the highest intense XRD peak at (311). Well known Scherrer formula, i.e., equation (4.3), was used for calculation, and resultant data are presented in Table 5.1. The output shows that the particle sizes are in the ranges of 34 nm to 58 nm. This crystallite size study is found suitable in other reports (Hossen, Nasrin and Hossen, 2020). In high-density recording media, these crystallite sizes are helpful to record an optimized signal-to-noise ratio.

Table 5.1: Various parameters calculated from XRD data of *NMCCFO.*

Mn content, (x)	**Crystallite Size, D (nm)**	**Lattice constant, a (Å)**	
		Experimental	**Theoretical**
0.0	34	8.37	8.46
0.1	44	8.38	8.47
0.2	48	8.39	8.49
0.3	50	8.42	8.51
0.4	51	8.43	8.53
0.5	58	8.47	8.55

The average crystallite size increases with the increase of Mn content as shown in Figure 5.2. In this case, lattice strain could be induced due to the dissimilarity in ionic radius of Ni^{+2} (0.69 Å) and substituted Mn^{+2} (0.83 Å). In this regard, effect of site preference of cations in ferrite system could play as an additional factor. Another explanation may be cited from crystal growth point of view. Variation of crystallite size as a function of Mn content might be related to the effect of heat treatment on molecular concentration of elements coming for nucleation on crystal surface during the crystal growth process. The increasing Mn content in ferrite system causes liberation of less latent heat due to exothermic reaction at crystal surface which enhanced the crystallite growth (Upadhyay, Verma and Anand, 2004).

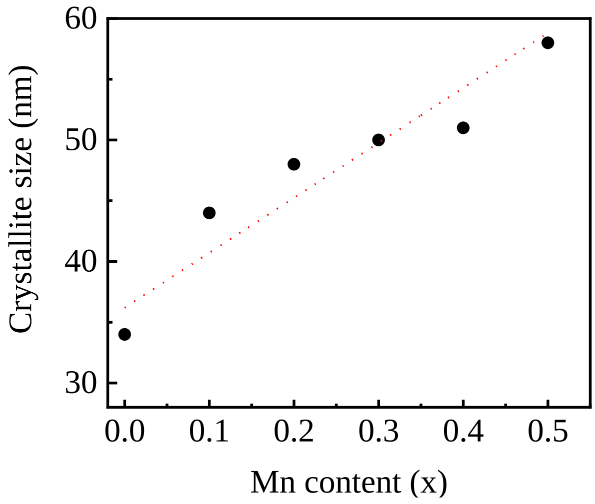

Fig. 5.2: Crystallite size of *NMCCFO* for different Mn contents (x).

5.2.1 Determination of lattice constant of *NMCCFO*

The theoretical lattice constant (a_{th}) and the experimental lattice constant (a_{exp}) were calculated by using the equation (4.11) and (4.4) respectively and are given in Table 5.1. For easy assimilation, the calculation of one of the samples is shown below:

For x = 0.0 : $Ni_{0.5}Cu_{0.2}Cd_{0.3}Fe_2O_4$

Cation distribution: $(Ni_{0.094}Cu_{0.015}Cd_{0.195}Fe_{0.696})_A[Ni_{0.406}\ Cu_{0.185}Cd_{0.105}Fe_{1.304}]_B$

$$\begin{aligned} r_A &= C_{ANi}r(Ni^{2+}) + C_{ACu}r(Cu^{2+}) + C_{ACd}r(Cd^{2+}) + C_{AFe}r(Fe^{3+}) \\ &= (0.094 \times 0.69) + (0.015 \times 0.72) + (0.195 \times 0.97) + (0.696 \times 0.645) \\ &= 0.7137\text{Å} \end{aligned}$$

$$\begin{aligned} r_B &= \frac{1}{2}[C_{BNi}r(Ni^{2+}) + C_{BCu}r(Cu^{2+}) + C_{BCd}r(Cd^{2+}) + C_{BFe}r(Fe^{3+})] \\ &= \frac{1}{2}[(0.406 \times 0.69) + (0.185 \times 0.72) + (0.105 \times 0.97) + (1.304 \\ &\qquad \times 0.645)] \\ &= 0.6780\text{Å} \\ a_{th} &= \frac{8}{3\sqrt{3}}\left[(r_A + R_0) + \sqrt{3}\ (r_B + R_0)\right] \\ &= \frac{8}{3\sqrt{3}}\left[(0.7137 + 1.32) + \sqrt{3}\,(0.6780 + 1.32)\right] \\ &= 8.4591\text{Å} \end{aligned}$$

Where $r(Ni^{2+})$, $r(Cu^{2+})$, $r(Cd^{2+})$, and $r(Fe^{3+})$ are the ionic radii of Ni (0.69Å), Cu (0.72Å), Cd (0.97Å), and Fe (0.645Å) respectively. C_{ANi}, C_{ACu} C_{ACd}, and C_{AFe} are the concentrations of A- sites and C_{BNi}, C_{BCu}, C_{BCd}, and C_{BFe} for B-sites respectively.

The calculation shows that the theoretical lattice constant (a_{th}) of the sample, 8.46 Å is closer to that of experimental lattice constant (a_{exp}) i.e., 8.37 Å. Similar way all substituted values of investigated samples were measured and exhibited in Table 5.1. It is to be noted that the result of both lattice parameters in present work matched quite well and variance recorded up to 1.5% which is also supported by the other research works (Hossen, Nasrin and Hossen, 2020). This indicates a realistic estimation of cation distribution by Reitveld technique that we applied for refinement of XRD data. Moreover, reasonable causes for the above-mentioned deviation between a_{th} and a_{exp} may be related to the formation of Fe^{2+} and crystal imperfections along with different measuring techniques of ionic radius (Akash et al., 2016).

The plot of experimental and theoretical lattice constant against Mn content are shown in Figure 5.3. The graph shows that both the values of lattice constant are increased as Mn content increases. From the Table 5.1 and Figure 5.3, it is also found that both the lattice constant of pure Ni-Cu-Cd (8.37 Å) is less than that of the substituted sample (8.48 Å) and both (experimental and theoretical) the values of lattice constant increase linearly with the increase of Mn content. Vegard's Law of linearity explains the result which is the increase of lattice constant is proportional to the increase of ionic radius (Deraz and Alarifi 2012). Here, in the $Ni_{0.5-x}Mn_xCu_{0.2}Cd_{0.3}Fe_2O_4$, the ionic radius of Mn^{2+} (r_{Mn}= 0.83 Å) is larger in than that of Ni^{2+} (r_{Ni}=0.69 Å) and Fe^{3+} (r_{Fe}=0.65 Å) respectively. As the smaller ionic radius of Ni^{2+} is substituted successively by the larger ionic radius of Mn^{2+}, the unit cell length gets extended to preserve the overall cubic symmetry which results in increasing lattice constant linearly (Hossen, Nasrin and Hossen, 2020, Muhammad and Maqsood, 2008).

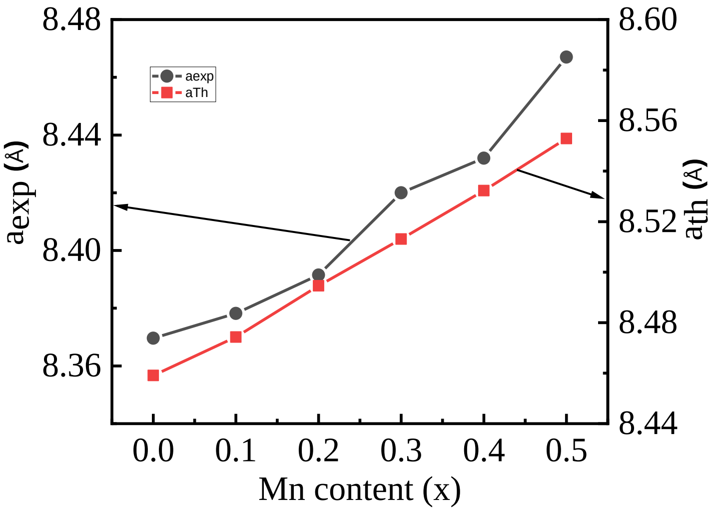

Fig. 5.3: Variation of experimental and theoretical lattice constant with Mn content of *NMCCFO.*

This can also be explained with the formula of mean ionic radii of variant ions (Smit and Wijn, 1959).

$$r_{(variant)} = (0.5 - x)r_{Ni} + xr_{Mn} + 2r_{Fe} \qquad (5.1)$$

It is observed from the above equation that $r_{(variant)}$ increases with the addition of Mn content.

5.2.2 Bond length, hopping length and ionic radii of *NMCCFO*

The bond lengths (A—O, B—O), hopping lengths (L_A, L_B) of tetrahedral (A site) and octahedral (B site) and the Ionic radii of tetrahedral (r_A) and octahedral (r_B) sites are calculated by using the equation of 4.5, 4.6, 4.9, 4.10, 4.7 and 4.8 respectively and are shown in Table 5.2. The variation of bond lengths (A—O, B—O) and hopping lengths (L_A, L_B) with Mn content are shown in Figure 5.4. It is observed from the figure that both the values are increased with the increase of Mn content which establish a direct relation among them (Hossen, Nasrin and Hossen, 2020, Arifuzzaman et al., 2020).

From Table 5.2, it is found clearly in experimental samples that r_A varies from 0.46 Å to 0.48 Å which are less than that of Mn^{2+} and Ni^{2+}. Thus, to give space for these ions (Mn, Ni) in tetrahedral sites, r_A needs to be expanded and hence lengths between anions related to A-sites will be increased. This causes increasing of bond length (A—O) at tetrahedral sites. On the other hand, when r_B decreases, bond length (B—O) also decreases. It is because, when ionic radius at octahedral site (r_B) decreases, the associated anions will move towards B-sites and thus reducing bond length (B—O). This reduction explains that anions associated with B-sites will shift away from A-sites and will result in increasing oxygen positional parameter (u) (Raghuvanshi, Mazaleyrat and Kane, 2018). The larger value of B—O than A—O may indicate larger orbital overlapping of Fe and O ions at the A-sites.

Table 5.2: Various bond length, hoping length and ionic radius of *NMCCFO.*

Mn content, (x)	**Bond Length, Å**		**Hoping Length, Å**		**Ionic radius of A and B sites, Å**	
	A — O	**B — O**	**L_A**	**L_B**	**r_A**	**r_B**
0.0	1.811	2.091	3.622	2.953	0.461	0.741
0.1	1.812	2.092	3.624	2.954	0.462	0.742
0.2	1.815	2.095	3.629	2.959	0.465	0.745
0.3	1.823	2.105	3.646	2.972	0.473	0.755
0.4	1.826	2.108	3.651	2.976	0.476	0.758
0.5	1.833	2.116	3.666	2.989	0.483	0.766

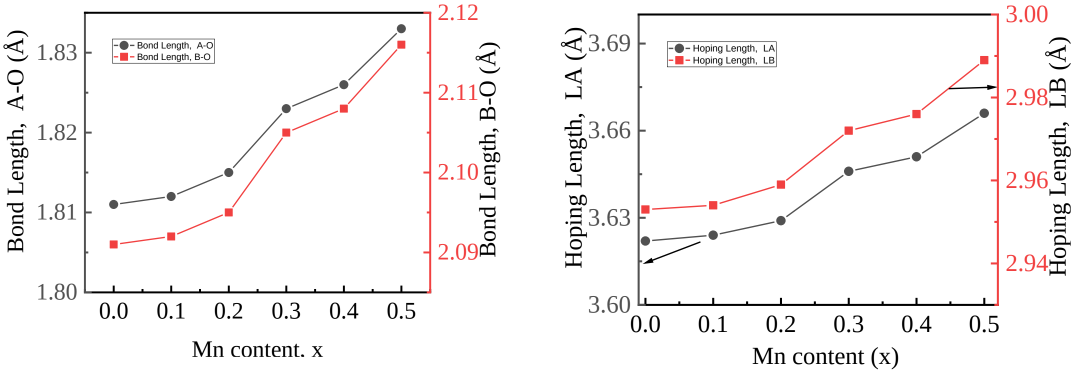

Fig. (a) Fig. (b)

Fig. 5.4: Variation of (a) Bond length and (b) Hopping length with Mn content of *NMCCFO.*

5.2.3 Goodness of fit of *NMCCFO*

Refined XRD patterns through Rietveld refinement process are shown in Figure 5.5. Red lines and black lines are representing the observed data and calculated data respectively for all samples. The values of chi square (χ^2) are found below 2 for all investigated samples. Hence, the fitting process can be termed as the good fitting (Kumar et al., 2013) which can also be seen from the patterns as both experimental and calculated curves are fitted perfectly and almost coincide with each other.

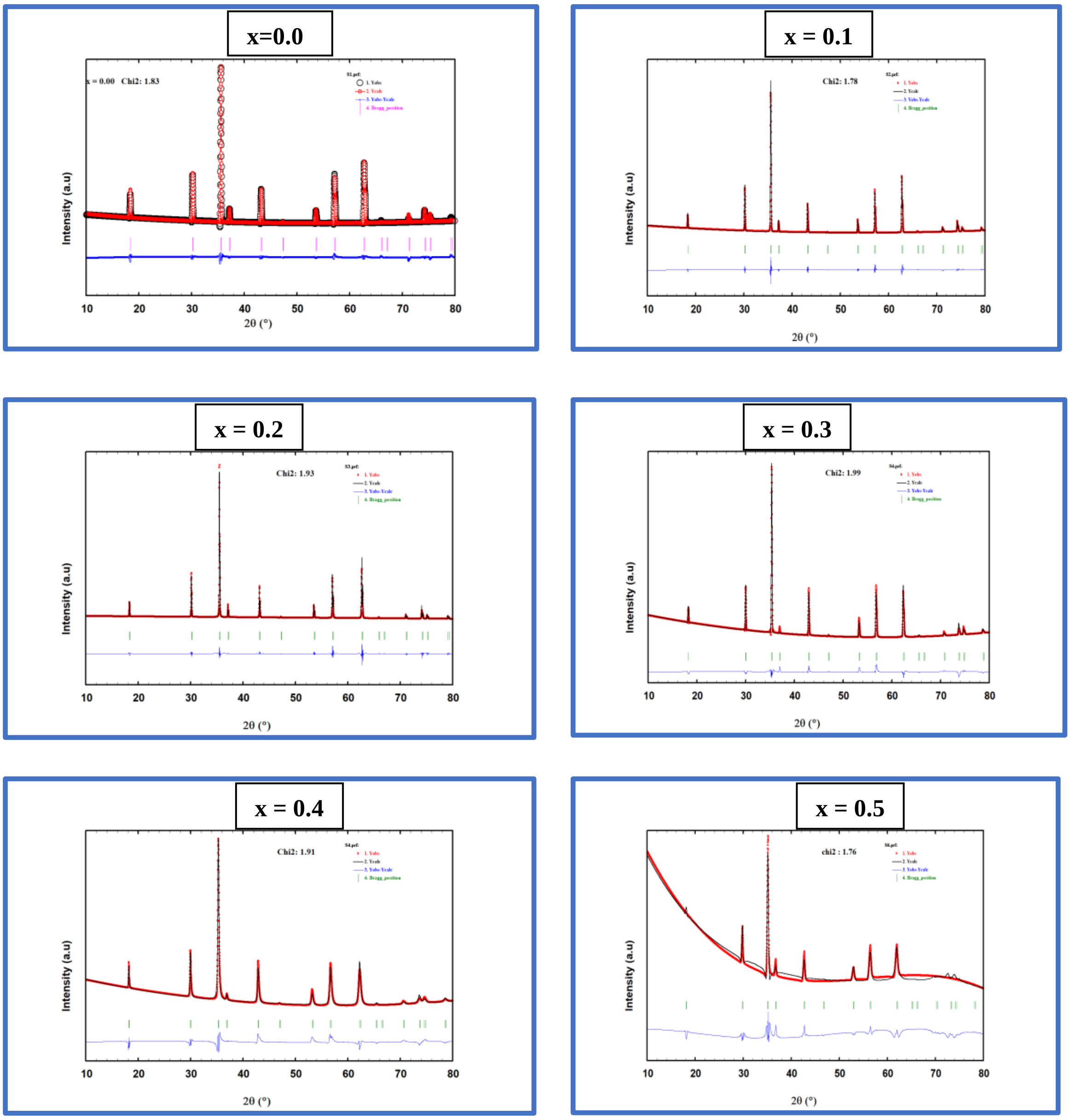

Fig. 5.5: Refined XRD data of *NMCCFO* for different Mn contents by Reitveld refinement method.

As a result, the line at the bottom which is denoted as the difference between experimental and calculated pattern is found almost linear in every case. The refinement was done within in the diffracted angle between 10° and 80° and found only the major peaks as found in the XRD patterns without any extra peaks. Similar results were found in previous reported work for dense ceramics (Mahmood and Hossen, 2021).

5.2.4 Cation distribution of *NMCCFO*

In case of spinel ferrite samples, the influence of cations and their distributions in interstitial sites plays a key role on investigating properties and their suitability for application in technology. Site occupancy of cations is a multifaceted step by step process and depends on certain specific factors comprises of internal (i.e., size, valency, presence of other ions etc.) and external (i.e. preparation method, preparation environment etc.) factors (Raghuvanshi, Mazaleyrat and Kane, 2018). This cation distribution can be extracted by processing XRD diffraction data. In this present study, Rietveld technique is adopted to determine the cation distribution. The final allocation of cations on tetrahedral and octahedral sites, basing on fraction concentration and site preference, is presented in Table 5.3.

Table 5.3: Cations distribution of *NMCCFO*.

x	Composition	Tetrahedral A-sites	Octahedral B-sites
0.0	$Ni_{0.5}Cu_{0.2}Cd_{0.3}Fe_2O_4$	$Ni_{0.094}Cu_{0.015}Cd_{0.195}Fe_{0.696}$	$Ni_{0.406}Cu_{0.185}Cd_{0.105}Fe_{1.304}$
0.1	$Ni_{0.4}Mn_{0.1}Cu_{0.2}Cd_{0.3}Fe_2O_4$	$Ni_{0.157}Cu_{0.058}Cd_{0.068}Mn_{0.098}Fe_{0.619}$	$Ni_{0.243}Cu_{0.142}Cd_{0.232}Mn_{0.002}Fe_{1.381}$
0.2	$Ni_{0.3}Mn_{0.2}Cu_{0.2}Cd_{0.3}Fe_2O_4$	$Ni_{0.146}Cu_{0.056}Cd_{0.066}Mn_{0.140}Fe_{0.591}$	$Ni_{0.154}Cu_{0.144}Cd_{0.234}Mn_{0.060}Fe_{1.409}$
0.3	$Ni_{0.2}Mn_{0.3}Cu_{0.2}Cd_{0.3}Fe_2O_4$	$Ni_{0.124}Cu_{0.061}Cd_{0.079}Mn_{0.132}Fe_{0.604}$	$Ni_{0.076}Cu_{0.139}Cd_{0.221}Mn_{0.168}Fe_{1.396}$
0.4	$Ni_{0.1}Mn_{0.4}Cu_{0.2}Cd_{0.3}Fe_2O_4$	$Ni_{0.095}Cu_{0.064}Cd_{0.076}Mn_{0.141}Fe_{0.625}$	$Ni_{0.005}Cu_{0.136}Cd_{0.224}Mn_{0.259}Fe_{1.375}$
0.5	$Mn_{0.5}Cu_{0.2}Cd_{0.3}Fe_2O_4$	$Cu_{0.088}Cd_{0.100}Mn_{0.186}Fe_{0.626}$	$Cu_{0.112}Cd_{0.200}Mn_{0.314}Fe_{1.373}$

Moreover, the graphical demonstration is also illustrated clearly in Figure 5.6 against increasing Mn content. This figure depicts the occupation of Ni, Mn, Cu, Cd and Fe ions on tetrahedral A-sites and octahedral B-sites respectively for studied samples basing on XRD data analysis. Figure 5.6 (a) explains the main features related to Fe^{3+} where it occupies both A and B-sites. Up to x = 0.2, Fe ions has a increasing trend of occupying at B-sites where as at A-sites it decreases. Maximum value of Fe concentration is recorded at x = 0.2 i.e.

maximum migration of Fe ions from A-sites to B-sites occurs. With further increase in Mn ion, a slow reverse result is found. This would affect overall magnetization.

In Figure 5.6 (b) a major shift is observed in Cd^{2+} in A-site to B-site which has an impact in changes among lattice constant and other structural parameters. In Figure 5.6 (c) and (d), similar pattern of transition from B-site to A-site can be marked up to x = 0.1 among Ni and Cu ions.

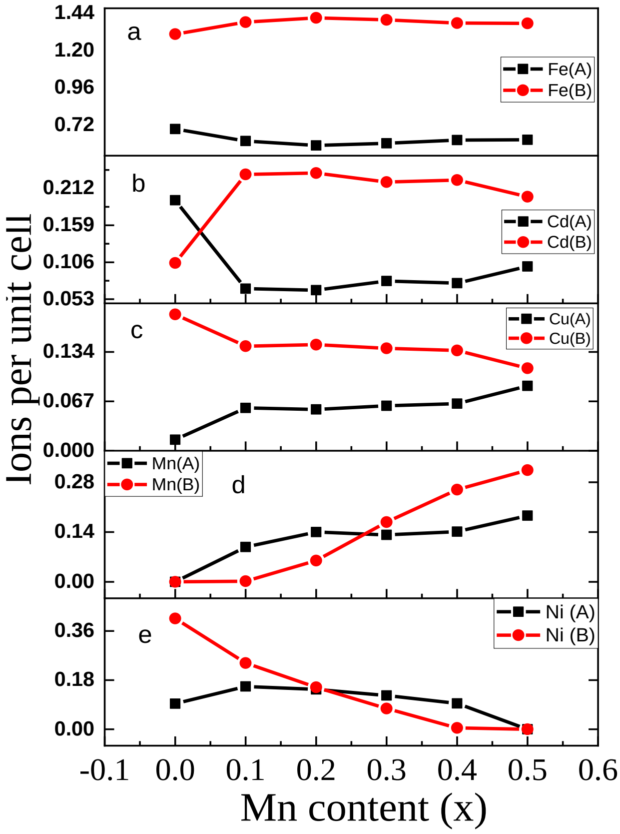

Fig. 5.6: Cationic distribution both in A-site (tetrahedral) and B-sites (octahedral) of *NMCCFO* for different Mn contents (x) by Rietveld refinement.

In Figure 5.6 (d), Mn ion remains more populated at A-site up to x = 0.3, then it alters its course due to more contents. Similar result is also seen in case of Ni ions which explain major substitutions are observed at B-site. Here it is to be noted that with increasing Mn contents and due to the presence of different ions, sites-A and sites-B get affected and non-equilibrium cation distribution is observed. These findings are also reported earlier (Hossen, Nasrin and Hossen, 2020).

5.2.5 Maximum Entropy Map (MEM) of *NMCCFO*

The maximum entropy map (MEM) method was applied to study electron density distribution with the software named *Fullprof*, which is usually used for Rietveld analysis. This method is a robust statistical tool for determining electron density from a limited number of structure factors. The main idea of MEM is to introduce the thermo-dynamical concept of entropy into informational or statistical data due to solving problems that are suffering from incomplete or noisy information by reconstructing the problem itself. It creates the basis for statistical mechanics and plays a significant role in characterizing experimental / laboratory data in astronomy, economics, crystallography, medicine etc. The MEM provides a distribution that matches the given data, is least biased with missing information, and does not put correlations in expected results from data. In short, the MEM provides the most probable result out of the least input data with the best fit map. Here, in the present study, "image" consist of mapping electron-density and structure factors of Bragg reflection is the source of "data". Certain basic equations and algorithms are developed to develop the MEM (Magdysyuk, Smaalen, and Dinnebier, 2019). MEM helps to visualize the redistribution and localization of charge density. In Figure 5.7, MEM of different compositions of studied samples are delineated, and 2D and 3D maps are projected with colour code and value range. These MEM calculations have provided an approximated mapping of the charge density of crystal phases. Maximum charge density is depicted with a positive value in yellow color. The minimum value is represented by light sky blue with a negative sign. These indicators show types of bonding between different elements in the samples. Positive values demonstrate a covalent bond, whereas ionic and metallic bonds are denoted by negative values in which the exchange of charges forms bonds.

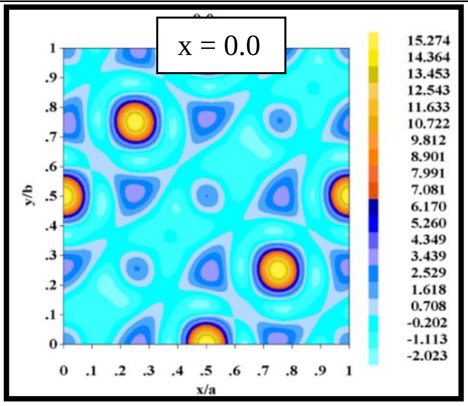

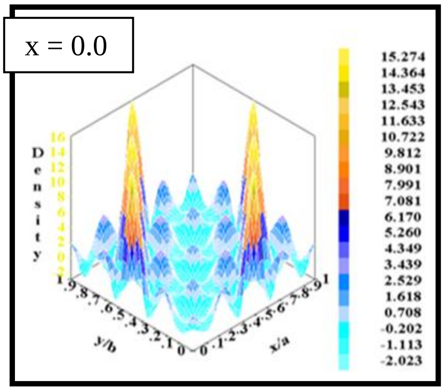

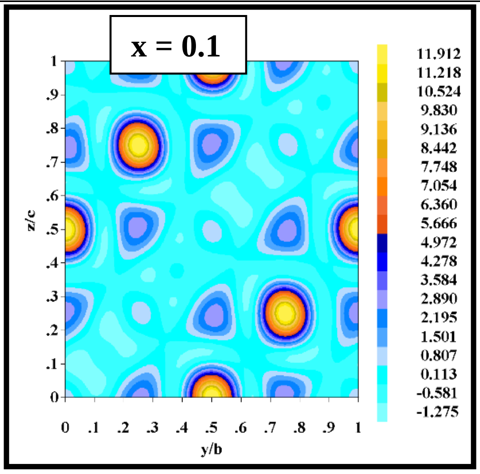
x = 0.1
z/c
y/b
0 .1 .2 .3 .4 .5 .6 .7 .8 .9 1
11.912
11.218
10.524
9.830
9.136
8.442
7.748
7.054
6.360
5.666
4.972
4.278
3.584
2.890
2.195
1.501
0.807
0.113
-0.581
-1.275

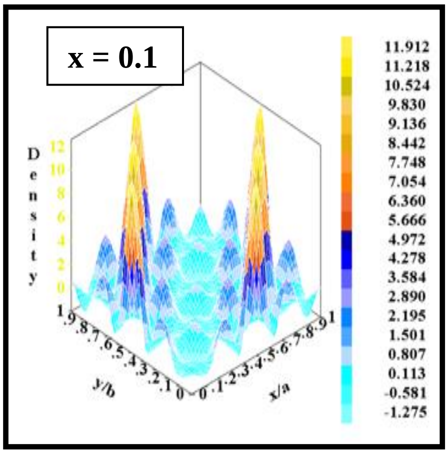
x = 0.1
Density
y/b
x/a
11.912
11.218
10.524
9.830
9.136
8.442
7.748
7.054
6.360
5.666
4.972
4.278
3.584
2.890
2.195
1.501
0.807
0.113
-0.581
-1.275

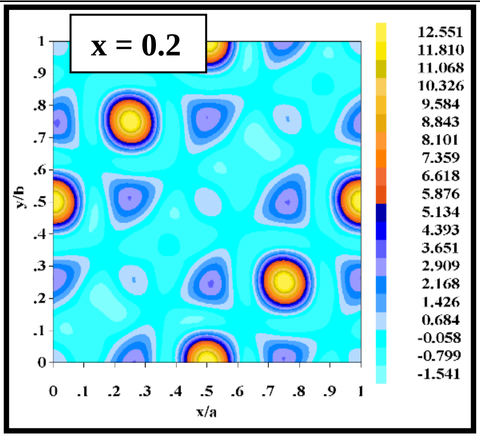
x = 0.2
y/b
x/a
0 .1 .2 .3 .4 .5 .6 .7 .8 .9 1
12.551
11.810
11.068
10.326
9.584
8.843
8.101
7.359
6.618
5.876
5.134
4.393
3.651
2.909
2.168
1.426
0.684
-0.058
-0.799
-1.541

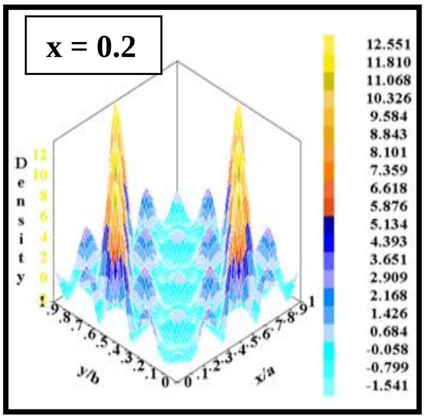
x = 0.2
Density
y/b
x/a
12.551
11.810
11.068
10.326
9.584
8.843
8.101
7.359
6.618
5.876
5.134
4.393
3.651
2.909
2.168
1.426
0.684
-0.058
-0.799
-1.541

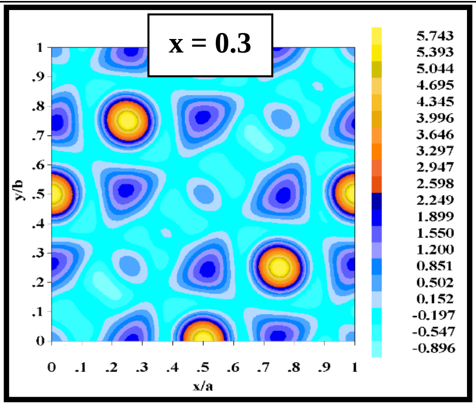
x = 0.3
y/b
x/a
0 .1 .2 .3 .4 .5 .6 .7 .8 .9 1
5.743
5.393
5.044
4.695
4.345
3.996
3.646
3.297
2.947
2.598
2.249
1.899
1.550
1.200
0.851
0.502
0.152
-0.197
-0.547
-0.896

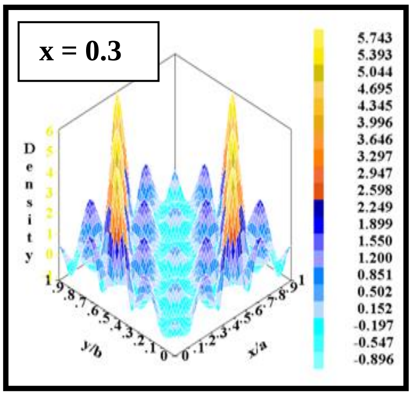
x = 0.3
Density
y/b
x/a
5.743
5.393
5.044
4.695
4.345
3.996
3.646
3.297
2.947
2.598
2.249
1.899
1.550
1.200
0.851
0.502
0.152
-0.197
-0.547
-0.896

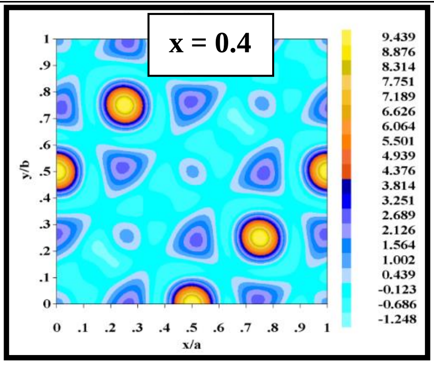
x = 0.4
y/b
x/a
0 .1 .2 .3 .4 .5 .6 .7 .8 .9 1
9.439
8.876
8.314
7.751
7.189
6.626
6.064
5.501
4.939
4.376
3.814
3.251
2.689
2.126
1.564
1.002
0.439
-0.123
-0.686
-1.248

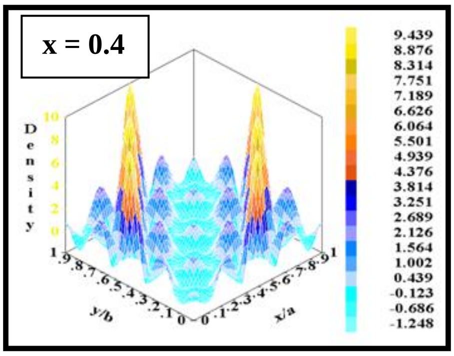
x = 0.4
Density
y/b
x/a
9.439
8.876
8.314
7.751
7.189
6.626
6.064
5.501
4.939
4.376
3.814
3.251
2.689
2.126
1.564
1.002
0.439
-0.123
-0.686
-1.248

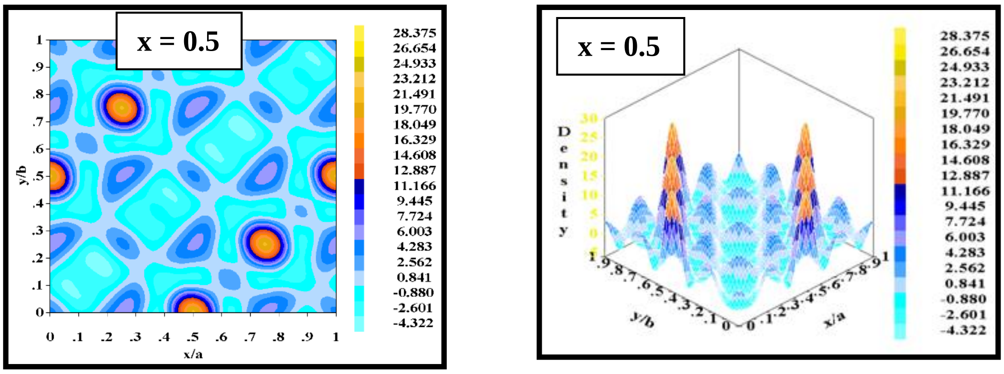

(a) (b)

Fig. 5.7: MEM map of Mn substituted NMCCFO bulk ferrites (a) 2D images and (b) 3D images.

Delocalized charges with covalent bonds have been observed in the maps. Since covalent bonds are created through the imbrication of electron densities, the bond between Fe^{3+} and O^{2+} is of this type with isotropic nature. It is also known that strong covalent and ionic bonds have a direct impact on stiffness. Additionally, a metal-metal covalent connection regulates the tolerance of damage caused by simple shear deformation. Strong covalent bonds are observed in the atoms of various combinations in this investigation. The most intriguing finding of this analysis is the reduction of ionic forms in ferrite dense ceramics caused by the emerging Mn substitution on the ferrite sites. As more manganese is added, the covalent bonds have grown stronger as a result.

5.2.6 Densification and porosity of *NMCCFO*

Study of density is significant because of its influence over the properties of materials specially in structural and electromagnetic properties which are highly affected by densification process. The bulk density (ρ_{exp}) and the theoretical density (ρ_x) were determined by using the equation of 4.12 and 4.13 respectively and included in Table 5.4. The ρ_{exp} depends on mass and volume but the ρ_x is influenced by both the molar mass (M) and the experimental lattice constant (a_{exp}). It is observed that the molar mass of non-substituted *NMCCFO* sample is 251.47 g/mol and maximum substituted one is 249.59 g/mol that is a decreasing pattern. The value of a_{exp} varies from 8.37 Å up to 8.47 Å that is a rising trend.

Table 5.4: Molar mass, bulk density, theory density and porosity of *NMCCFO*.

Mn content, x	Molar mass, M, (g/mol)	Bulk density, ρ_{exp}, (g/cc)	Theory density, ρ_x, (g/cc)	Porosity, P (%)
0.0	251.47	4.62	5.70	18.95
0.1	251.09	4.45	5.69	21.79
0.2	250.72	4.31	5.65	23.72
0.3	250.34	4.23	5.57	24.06
0.4	249.95	4.18	5.54	24.55
0.5	249.59	4.10	5.46	24.91

Figure 5.8 shows the variation of density and porosity of *NMCCFO*. It is observed from graph that both the theoretical, ρ_x and bulk, ρ_{exp} densities decrease with increasing Mn content. The decrease of ρ_x may be due to reduction in molar mass, M which outgrows the cell volume. Moreover, in the Table 5.3, the bulk density, ρ_{exp} is found decreasing from 4.62 g/cc to 4.01 g/cc while Mn content increasing. This may be explained with the fact that the atomic weight and density of Mn^{2+} (7.43 g/cc) are lower than those of Ni^{2+} (8.91 g/cc). This substitution causes the structural distortion and results in decreasing of bulk density, ρ_{exp}.

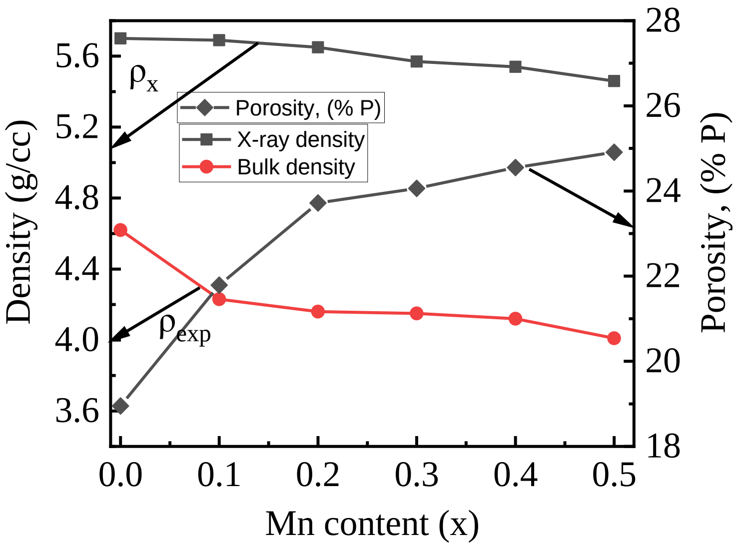

Fig. 5.8 : Variation of density and porosity with Mn content of *NMCCFO*.

It is also observed from Table 5.4 that the ρ_x is higher than ρ_{exp}. The reasons may be the presence of pores which are grown during the preparation of compositions or due to sintering process (Hossen, Nasrin and Hossen, 2020, Muhammad and Maqsood, 2008).

In fabrication process, bulk ferrites are produced from nanocrystalline powders and during compaction process for shaping, pores or void spaces present between nano particles. After sintering, total pore elimination process often remain incomplete and some residual porosity exist. This porosity has a significant effect on structural (elasticity and strength) and electromagnetic properties of ferrites. The porosity (%) was calculated by equation 4.17 and included in Table 5.4.

The existence of significant porosity is identified in the results. Maximum porosity, P (%) is found for x = 0.5. The porosity of the studied ferrite sample is mainly the product of two sources (i) P_{intra} (intragranular) and (ii) P_{inter} (intergranular) porosity. The 2nd one is grain size-dependent (Das, Bhattacharya, Sen and Maiti, 2009). The graph of porosity change with Mn contents is demonstrated in Figure 5.5. It is found that up to x = 0.5, porosity increases and maintains an opposite trend of bulk density.

5.3 Microstructure and surface morphology

Microstructure strongly affects the magnetic and electric properties of nano crystalline materials where grain size plays a key role. Figure 5.9 shows the micrographs of FESEM for different NMCCFO samples sintered at 1200°C. The average grain sizes were measured by linear intercept method. These images reveal the chronological changes in grain distribution due to the substitution of Mn addition in structure and the texture turns into lesser homogeneity. The closer scanning of the micrographs illustrates the presence of grains with clearly visible grain boundaries. Due to magnetic nature of transitional metals such textures are usually observed. This type of result is also seen in other research works (Lodhi, 2014).

Average grain sizes (d) and Mn content (x) are tabulated in the Table 5.5 which is also projected graphically in Figure 5.10. The size varies from 1 μm to 4 μm except x = 0.5 of Mn content. It is observed that the grain size increases with the increase of Mn content. This means that microstructure of NMCCFO is strongly dependent on Mn presence. Yan and Johnson reported the influence of Mn^{2+} addition and had shown that Mn act as a slight accelerator of grain growth (Shirsath et al., 2010). Moreover, the unit cell of Ni (0.69 Å) may be enlarged when it is replaced by Mn (0.83 Å), higher ionic radius ultimately encouraged atomic diffusion in the crystal lattice (Roy, Nayak and Bera, 2008). The melting point of Mn (1246°C) is lower than that of Ni (1455°C) which may also contribute in enhancing the grain size (Shah and Hossain, 2013). Besides, the interaction of grain boundary and pores is also contributing shaping the average sizes. The nature of grain growth reflects the race between the driving force for the grain boundary movement and the retarding force exerted by pores.

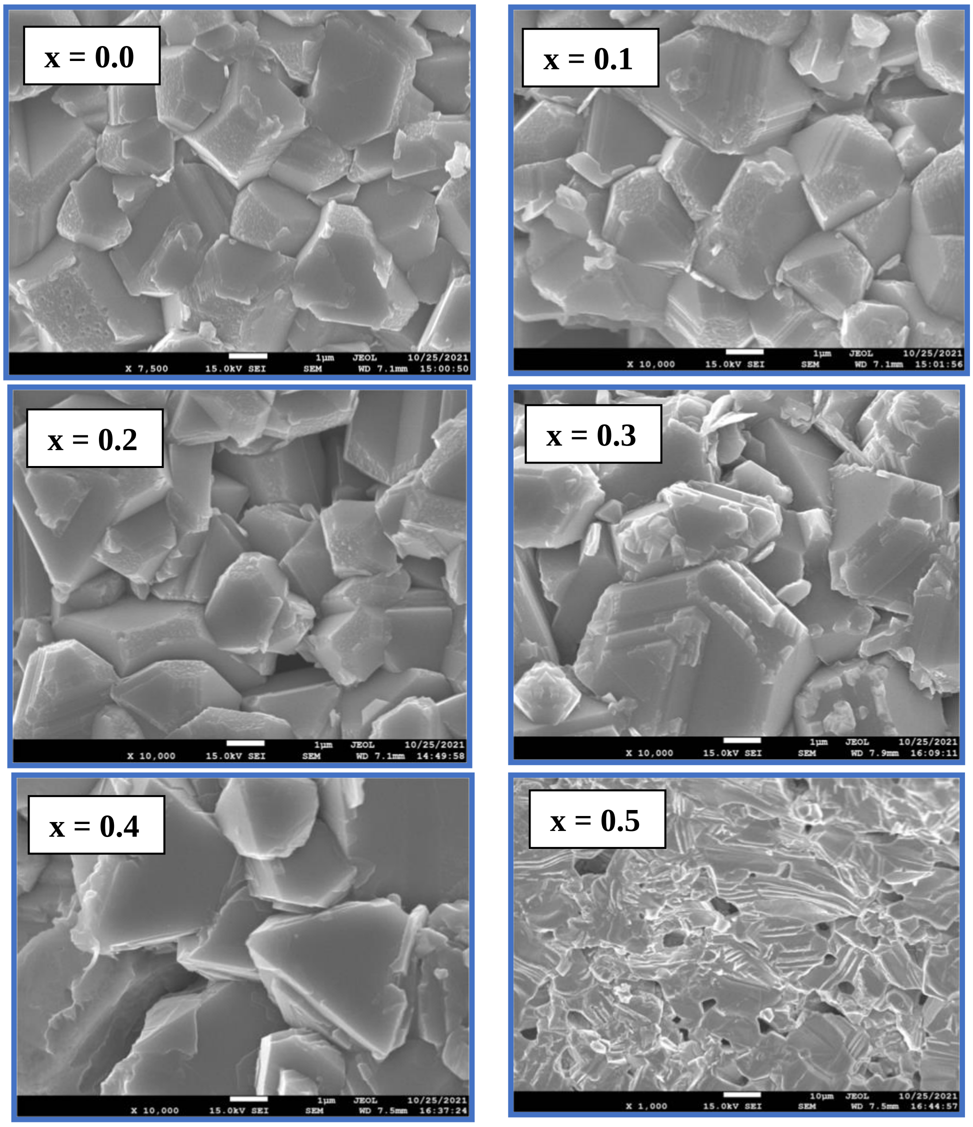

Fig. 5.9: The micrograph of FESEM images of *NMCCFO* for different Mn content sintered at 1200°C.

Table 5.5: Average grain sizes of NMCCFO sintered at 1200°C.

Mn content, (x)	**Crystallite size, D (nm)**	**Average grain sizes, d (μm)**
0.0	34	1.13
0.1	44	2.28
0.2	48	2.49
0.3	50	3.91
0.4	51	4.16
0.5	58	-

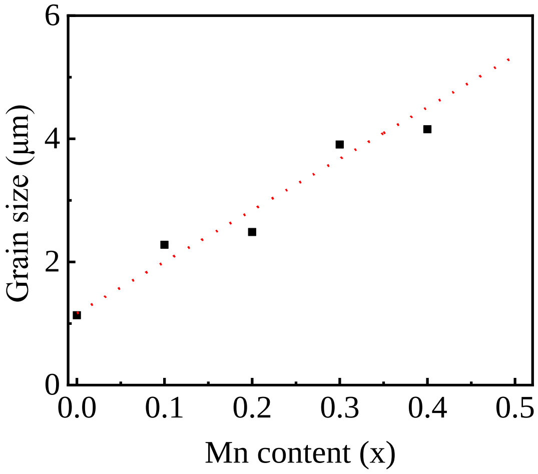

Fig. 5.10: Average grain sizes of *NMCCFO* for different Mn contents.

5.4 Elemental analysis of *NMCCFO*

The EDX study is applied to analyze chemical make-up of the sample and thereby investigates its purity calculating the percentages of various elements on surface area. The EDX spectra of NMCCFO bulk ferrite specimens is shown in Figure 5.11 at 0-20 keV energy range. The results support the presence of Ni, Mn, Cu, Cd, Fe, and O as well as the absence of any detectable impurities in the samples. Due to applying carbon coating for FE-SEM study prior to the measurement, the existence of carbon atoms is observed.

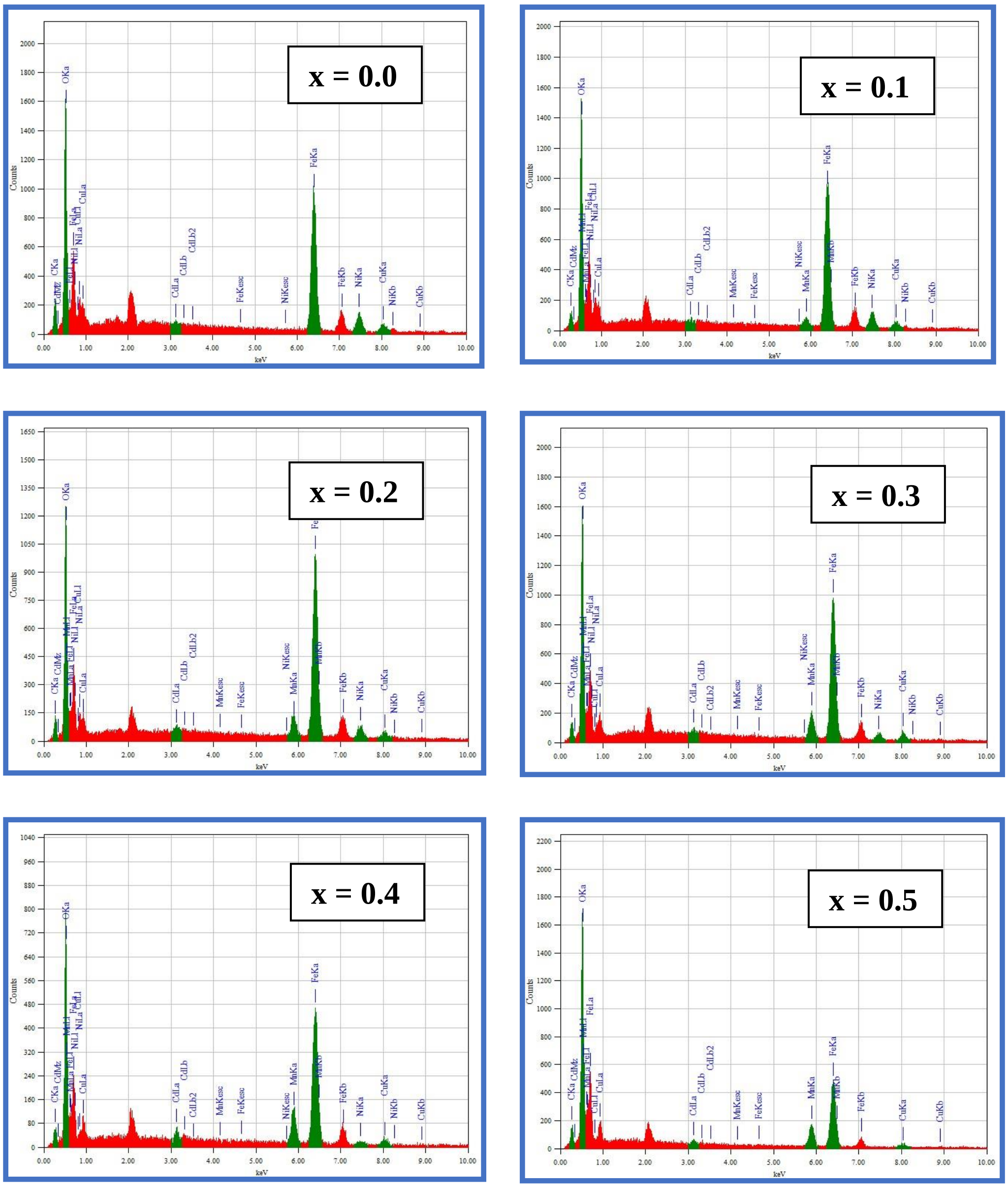

Fig. 5.11: EDX graphs of *NMCCFO* for different Mn contents.

Both the mass % and the element % of different compositions of NMCCFO samples are shown in Table 5.6. The result percentages indicate the absence of chemical reaction or ingredient loss.

Table 5.6: The EDX elemental (chemical composition) data analysis of NMCCFO.

x	**Mass %**							**Atomic%**						
	Ni	**Mn**	**Cu**	**Cd**	**C**	**Fe**	**O**	**Ni**	**Mn**	**Cu**	**Cd**	**C**	**Fe**	**O**
0.0	12.48	-	6.95	0.68	7.29	53.46	19.15	6.88	-	3.54	0.19	19.65	30.99	38.74
0.1	11.31	2.69	6.19	0.69	3.57	58.04	17.59	6.93	1.71	3.50	0.22	10.69	37.39	39.56
0.2	6.72	5.82	5.43	0.99	4.20	61.12	15.71	4.18	3.86	3.11	0.32	12.77	39.92	35.83
0.3	4.56	7.92	7.15	1.21	4.71	56.22	18.23	2.69	5.00	3.90	0.37	13.59	34.92	39.51
0.4	1.72	11.62	6.22	2.44	3.65	56.10	18.19	1.04	7.58	3.49	0.77	10.82	35.79	40.51
0.5	-	12.04	5.14	1.54	6.84	43.97	30.46	-	6.13	2.26	0.38	15.94	22.02	53.26

5.5 Dielectric properties study of $Ni_{0.5-x}Mn_xCu_{0.2}Cd_{0.3}Fe_2O_4$

5.5.1 Frequency dependent dielectric studies of NMCCFO

There are certain factors which modify the dielectric properties in polycrystalline materials namely cationic substitution or nature of dopants, preparation route, grain size etc. The NMCCFO samples is inhomogeneous in nature due to the polycrystalline structure where high conducting grains are separated by high resistive grain boundaries and pores. Frequency dependent dielectric real part, $\varepsilon^{/}$, imaginary part, $\varepsilon^{//}$ and loss tangent, $tan\delta$ of the different NMCCFO samples measured within 100 Hz to 100 MHz by impedance analyzer at room temperature are projected graphically in Figure 5.12. Distinct variations are observed with increasing frequency range along x-axis. In Figure 5.12 (a) and (b), both $\varepsilon^{/}$ and $\varepsilon^{//}$ graph show declining trends with increasing applied frequency which is a typical characteristic of the spinel ferrite. At lower frequency range, both $\varepsilon^{/}$ and $\varepsilon^{//}$ exhibit usual dispersion attitude but with increasing frequency domain, they tend to fall sharply and finally, becomes frequency independent after 1 MHz at higher range. In comparison between Figure 5.12 (a) and (b), it is found that $\varepsilon^{//}$drops more sharply than $\varepsilon^{/}$ which points out loss tangent, $tan\delta$ would decrease rapidly with addition of Mn content. The lowest dispersion occurred at x = 0.1 sample.

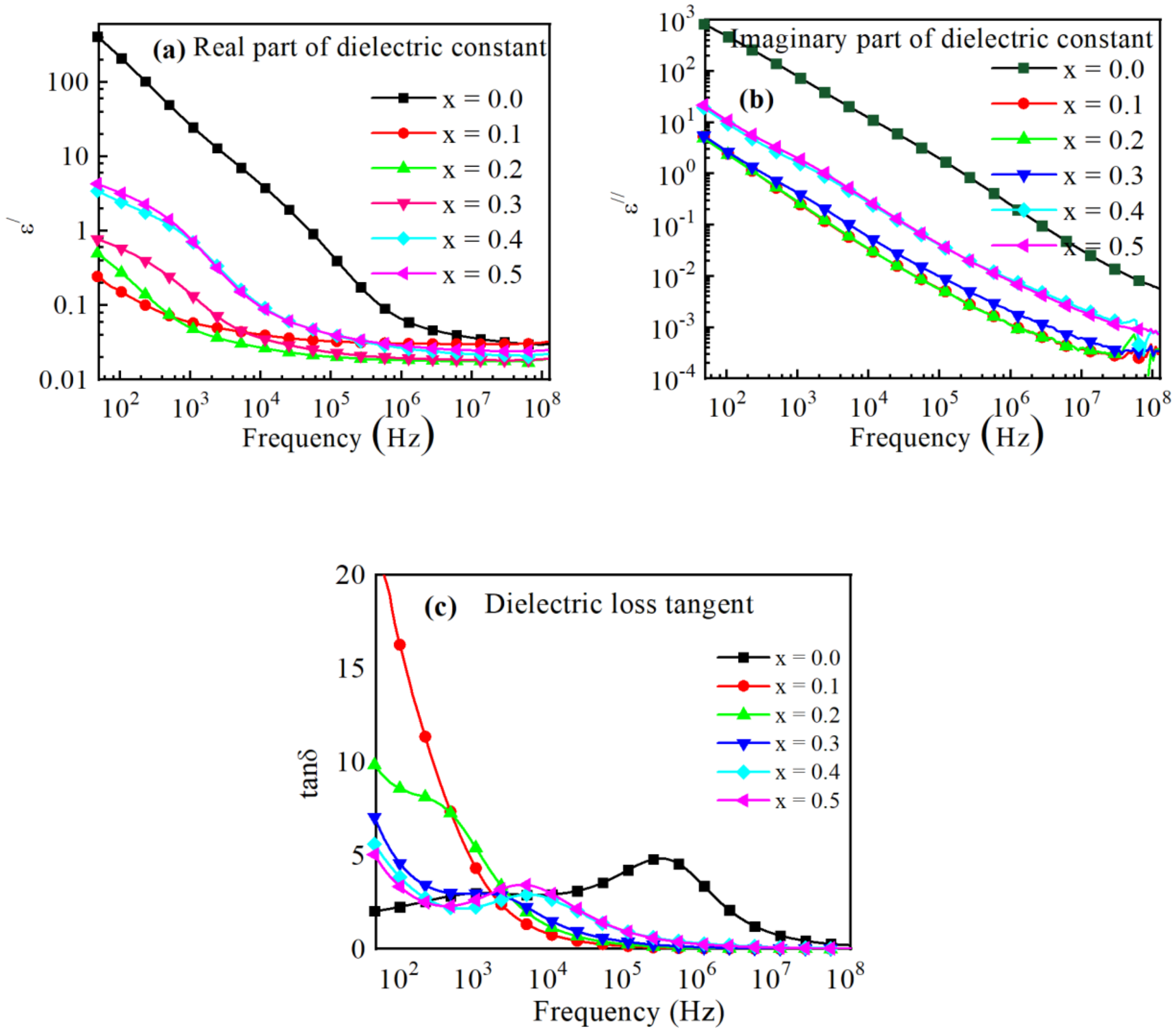

Fig. 5.12: Frequency dependent of (a) real part, (b) imaginary part and (c) loss tangent of dielectric constant of *NMCCFO* bulk ferrites for different Mn contents.

As polarization depends on valence state of ions and variation of space-charge polarization, so changes may occur in two different frequency regions. This phenomenon may be explained by two-layer model of Maxwell-Wagner Interfacial polarization in inhomogeneous condition along with Koop's theory (Maxwell,1954, Koops,1951). According to this theory, in heterogeneous ferrite samples, they could act as two layers conductor i.e., grain boundary with greater resistance (first layer) and grains itself as conductors (second layer). At low frequencies, first layer is activated with the applied electric field and number of accumulated charges becomes higher at grain boundary region due to its high resistance. Subsequently, the hopping mechanism occurs in ferrous and ferric ions pair, i.e., $Fe^{2+} \leftrightarrow Fe^{3+}$ which produces interfacial polarization. In addition, the charges obtain sufficient time to be aligned themselves with applied field. As a result, interfacial polarization increases and in turn relative permittivity or dielectric constant is also increases (Arifuzzaman et al., 2020). In the case of high frequency ranges, the second layer that is grains as conductors becomes activated. Due to the high applied frequency, electric dipoles are unable to synchronize with changes in the applied field and exhibit lag in tracking. With applying further higher frequency, frequency independent behavior is also observed. As a result, space charges cannot accumulate on grain boundary and causes rapid decrease in dielectric constant (Hossen, and Hossen, 2019). The variation among dielectric values in different frequency range could also be explained with different polarization process. At lower frequencies, all the four types polarization (electronic, ionic, orientational and space charge) contribute to the higher values of $\varepsilon^{/}$ and $\varepsilon^{//}$. But at higher range of frequencies, some of them are stopped to contribute in the lower values of $\varepsilon^{/}$ and $\varepsilon^{//}$ (Shah and Hossain, 2013).

Loss factor explains the loss of energy in the dielectric mechanism. Frequency dependent $tan\delta$ undergoes similar dispersion like dielectric constant except a peaking effect which are observed in Figure 5.12 (c). This occurrence may be explained in light of the Maxwell-Wagner (two layers) Model and Koop's theory. Because of the high resistance at grain boundaries, the Fe^{2+} ions require more energy for conversion into Fe^{3+} which ultimately results a higher value in tangent loss in lower frequency ranges. On the other side, at high frequency due to higher conductivity in grains, loss is minimum in transforming ferrites. There are peaks in $tan\delta$ graph of different samples which could be explained basing on relaxation condition (Mahmood and Hossen, 2021). The peaks are appeared when the hopping frequency of metal ions becomes equal to that of the applied electric field. Thus, the maximum electrical energy transfers to the oscillating dipoles at the resonance frequency and due to the maximum power loss, highest peaks are observed (Arifuzzaman et al., 2020). The dielectric loss are causes of impurity, moisture, crystal defects, and inhomogeneous nature. Low loss factor at higher frequency exposes the potentiality of the present samples in high frequency applications.

It also reveals that tangent loss, $tan\delta$ declines significantly with addition of Mn ions between steps $x = 0.1$ to $x = 0.5$. In dielectric samples, oxygen vacancies, grain size, density and porosity play a significant role in variating polarization and managing dielectric losses. As density decreased due to the substitution of Mn in present NMCCFO samples and porosity increased (Figure 5.8), so number of polarizing elements also decreased simultaneously; which in turn causing the declining value of $tan\delta$ (Hossen, Nasrin and Hossen, 2020, Hossen, and Hossen, 2019).

5.5.2 Electric modulus analysis of *NMCCFO*

The complex modulus is an effective tool to confirm the occurrence of dielectric relaxation in the ferrite materials and explain the relaxation process by considering space-modification of charge carriers (Hashim, Alimuddin, Shirsath, 2013). This analysis also reveals information about poly crystalline structure and the dynamics of electric response in ferrite samples. The frequency (f) dependent real part ($M^{/}$) and imaginary part ($M^{//}$) of electrical modulus for different Mn^{2+} contents are shown in Figure 5.13.

At low frequency zone ($<10^3$ Hz) in Figure 5.13 (a), $M^{/}$ seems to approach zero value whereas at high frequency region, it approaches sharply to saturation with highest value and becomes frequency independent. The reasons behind this consistent increasing value of $M^{/}$ from low to higher frequency range may be due to (i) long range conduction at low frequency range and (ii) short range conduction of mobile charges at high frequency (Hossen, Nasrin and Hossen, 2020). Approaching towards zero value at low frequency might be the deficiency of restoring force for the mobility of charge carriers under the influence of induced electric field. Generally, the mobility of charge carriers depends on the restoring force induced by applied field (Arifuzzaman, 2020).

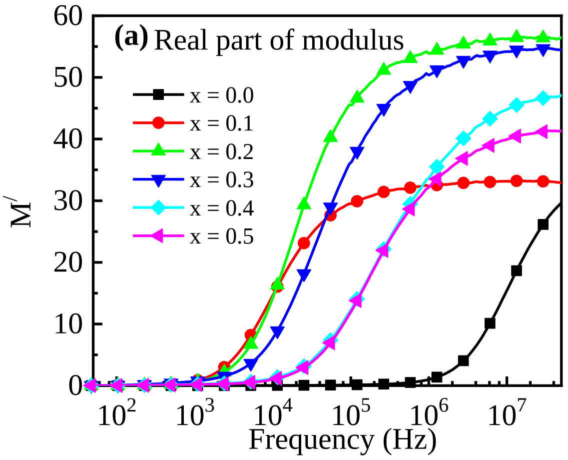

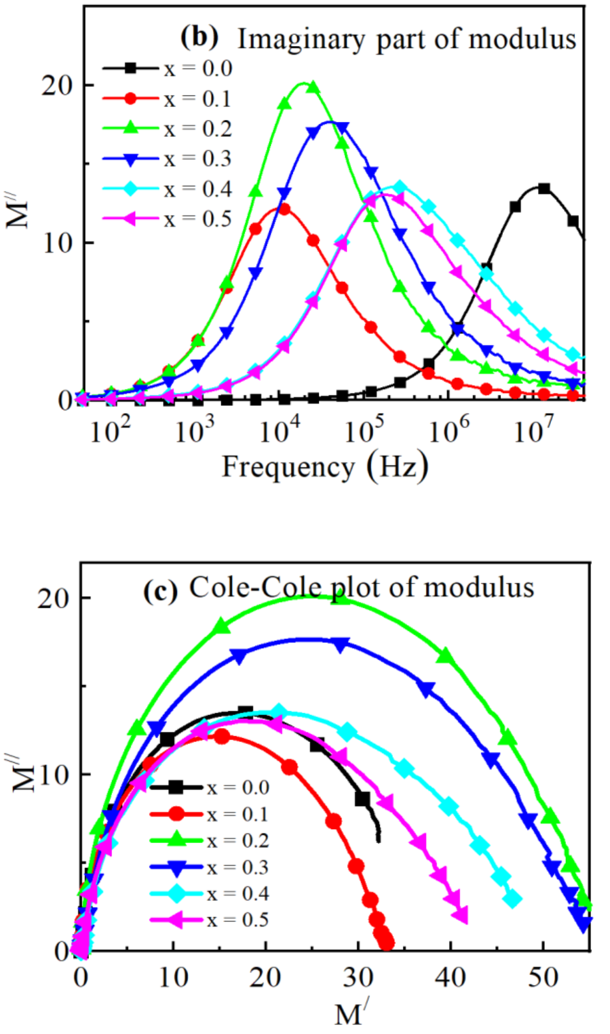

Fig. 5.13: Frequency dependent of (a) real part, (b) imaginary part of electric modulus and (c) the Cole-Cole plot of *NMCCFO* bulk ferrites for different Mn contents.

On the other side, in Figure 5.13 (b), the graphical representation of imaginary part, $M^{//}$ against frequency clearly shows a peaking nature. The peaks are shifted towards higher frequency range with the increasing of Mn content except x = 0.0. These peaks reveal different electrical parameters like ion dynamics, electrical transport and relaxation mechanism. The wider peak explains larger relaxation conductivity. The peaks for different compositions of the NMCCFO sample divide the frequency region into two parts clearly. The left side of the individual peak falls in low frequency region in which charge transporters have their long-range mobility where they can jump between two neighboring sites to accomplish hopping mechanism. Again, on the right side of the peak, short-range mobility occurs among charge carriers that means they continue their movement within the potential well (Hossen, Nasrin and Hossen, 2020).

The Cole-Cole plot ($M^{//}$ vs $M^{/}$) of electric complex modulus is illustrated in Figure 5.13 (c). The presence of semi-circular arcs indicates the existence of single-phase nature of the materials. The variation in diameters of the semi-circles due to the addition of Mn contents indicates significant improvement in conductivity. Such graphical representation suggested that the conduction phenomenon is due to non-Debye relaxation mechanism (Zulqarnain, 2021).

5.5.3 Impedance spectra study of *NMCCFO*

The frequency dependent impedance analysis is a crucial method to obtain information regarding the resistive ($Z^{/}$, real part) and the reactive ($Z^{//}$, imaginary part) elements of a magnetic material which facilitate understanding the conduction route, the structure of the material and defects. It is also an essential tool to differentiate the contribution of resistance among the grain and grain boundary of *NMCCFO*.

Impedance spectroscopy was carried out in the frequency range of 100 Hz to 100 MHz at room temperature. Figure 5.14 (a) illustrates the variation of the real part of impedance, $Z^{/}$, with frequency for different Mn contents. In this Figure, higher values of $Z^{/}$ are observed at lower frequencies. This might be the result of space charge polarization and low conduction mechanism in the materials. It is also observed that the value of $Z^{/}$ declines steadily up to a certain frequency and after that $Z^{/}$ is independent of frequency with lower values of $Z^{/}$ at higher frequencies. It means that when frequency increases, the internal resistance of the materials reduces, causes increase of conduction (Miah and Hossain, 2016).

Figure 5.14 (b) illustrates the frequency-dependent imaginary part of impedance, $Z^{//}$ for different compositions of Mn. All compositions show peaking nature except x = 0.0. At higher frequency range, a declining trend of $Z^{//}$ is also observed with independent of frequency.

Moreover, it is observed from both figures 5.14 (a) and 5.14 (b), the values of $Z^{/}$ and $Z^{//}$ are decreased gradually with the increase of Mn content except x = 0.0. The values of $Z^{/}$ and $Z^{//}$ for the substituted compositions are higher than the parent composition.

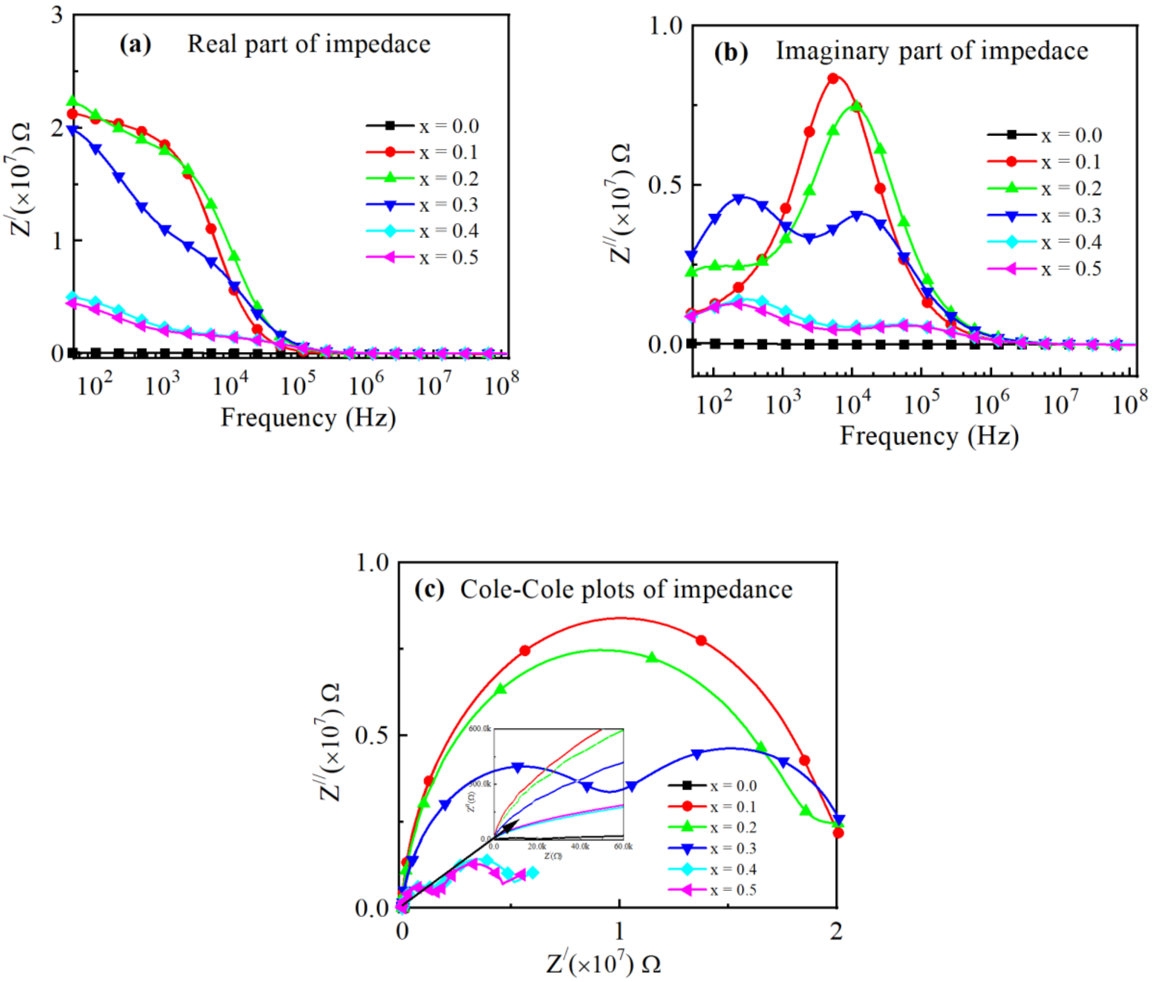

Fig. 5.14: Frequency dependent of (a) real part, (b) imaginary part of impedance and corresponding (c) the Cole-Cole plot of *NMCCFO* bulk ferrites for different Mn contents.

The Figure 5.14 (c) represents the Cole-Cole plots ($Z^{/}$ vs $Z^{//}$) which is also known as Nyquist diagram. The result from this plot may support the changes which are observed in dielectric property and ac conductivity measurement. Also, this plot is very useful to identify the contribution of grain boundary resistance and grain resistance. In this diagram, it is seen that all the semicircles end in the high frequency region of real impedance axis, $Z^{/}$. It explains the existence of grain resistance with disappearance of typical Debye nature (Arjunwadkar and Patil, 2014). Additionally, this graph explains the role conduction mechanism at grain boundaries. Plots with overlapping semicircular arcs show grain conduction at higher frequencies and semiconducting grain boundary conduction at lower frequencies. These may be explained with the help of brick-layer model.

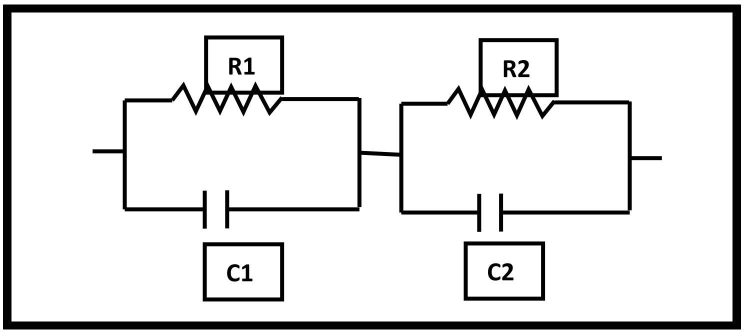

Fig. 5.15: Equivalent RC circuit.

According to the brick-layer model, which is typically used to examine the structural properties of nanocrystalline ferrite materials, each of these conductions can be represented by an ideal equivalent RC circuit as shown in Figure 5.15 (Behera et al., 2014). It may be assumed that a polycrystalline ferrite consists of large domains of fairly well conducting material (R_1 and C_1) which are separated by thin layers of relatively poorly conducting substances (R_2 and C_2). By using impedance spectroscopy, the equivalent RC circuit are used to determine the resistance and capacitance of the grain and grain boundary. The contribution of the grain boundary in ferrite materials is more significant than the grain resistance brought on by the presence of defects.

5.5.4 Frequency dependent AC conductivity of NCCFO

Figure 5.16 shows the frequency dependent ac electrical conductivity (σ_{ac}) for different Mn contents of NMCCFO ferrites. The frequency ranges were taken from 100 Hz to 10 MHz. Generally, a rising tendency of σ_{ac} with increasing frequency is observed for ferrite materials. Figure 5.16 demonstrates that at low frequency range, σ_{ac} remains nearly steady but at higher frequency range, it rises smoothly. This means, with increasing frequency, the conductivity becomes more dependent on frequency. In ferrite materials, conductivity develops through hopping mechanism of Fe^{3+} to Fe^{2+} ions at octahedral sites. The increase of σ_{ac} means the increase of rate of hopping between ferrous and ferric ions, not the increase of number of charge carriers. The rate of hopping of the electrons is increased with the increase of frequency. Therefore, the conductivity increases but resistivity decreases (Jonscher,1977).

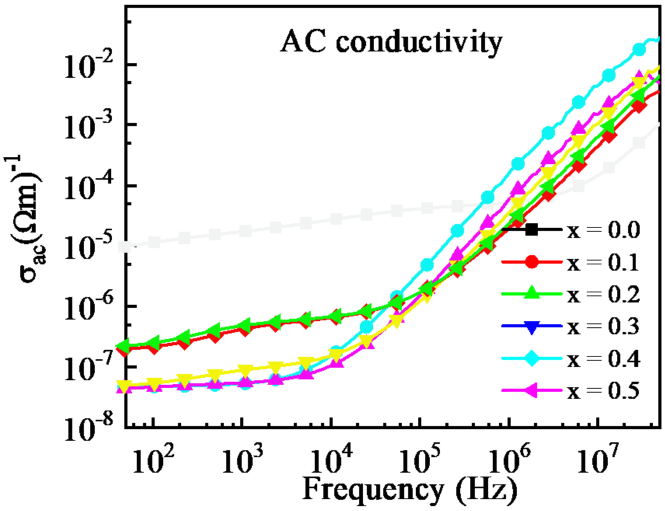

Fig. 5.16: Frequency dependence of ac conductivity (σ_{ac}) of dense NMCCFO bulk ferrites for different Mn contents.

The Fe^{3+}/Fe^{2+} ions concentration at B-sites depends on sintering conditions, temperature etc. The Maxwell-Wagner two-layer theory may also be used to describe how ac conductivity changes (Patil et al., 2000). According to this theory, at higher frequency domain, conduction is activated through the grains (highly conducting) which ultimately increases hopping of electrons between neighboring sites. On the other hand, at low frequency range, conduction is activated through high resistive grain boundaries which produce a smaller number of hopping electrons and causes high energy loss. Another reason for increasing conductivity may be conversion of σ_{dc} to σ_{ac} (Ram and Chakrabarti, 2008). The detailed hopping model is explained by Austin and Mott (Hossen, Nasrin and Hossen, 2020).

5.6 Magnetic properties of *NMCCFO*: VSM analysis

The magnetic properties of a material depend on how many permanent dipoles it has or not and the orientation of these dipoles to each other. Additionally, these properties are affected by anisotropy, density, compositions, cation distribution, and exchange interactions between tetrahedral A sites and octahedral B sites. The vibrating sample magnetometer (VSM) was used for magnetisation measurement at room temperature. The magnetic parameters of the Mn substituted *NMCCFO* ferrites are presented in Table 5.7 and Figure 5.17 shows the related hysteresis curve. From this hysteresis curve, the saturation magnetisation (M_s), remanent magnetisation (M_r), coercivity (H_c), the ratio (R) of M_r and M_s, anisotropy constant (K_1), and magnetisation magnetic moment (μ_B) are calculated at room temperature. All the compositions in the curve show the soft nature of ferrite due to the existence of small amount of M_r and H_c (Amri et al., 2021).

It is observed from Table 5.7, the highest and lowest values of M_s are noticed for x = 0.0 and x = 0.5 compositions of Mn respectively. The value of M_s decreases continuously from 65 emu/g (x = 0) to 30 emu/g (x = 0.5) with the increase of Mn content. This type of result is also seen in other research work (Mirzaee, Shayesteh and Mahdavifar, 2014). It is also evident from the Table 5.7, the calculated value of μ_B (magnetic moment) declines from 2.91 to 1.34 with the addition of Mn content. The variation of M_s and μ_B with Mn content is shown in Figure 5.18 (a).

Table 5.7: Magnetic parameters along with LAS fitted parameters of NMCCFO.

Mn content, (x)	K_1 from LAS (erg/cm^3)	M_s from LAS (emu/g)	M_S (emu/g)	M_r (emu/g)	R = M_r/M_S	μ_B (Bohr mag.)	K_1 (erg/cm^3)
0.0	0.25	65	65	7.76	0.12	2.91	0.25
0.1	0.22	58	59	7.06	0.12	2.64	0.23
0.2	0.17	54	55	2.18	0.04	2.45	0.18
0.3	0.12	38	39	0.77	0.02	1.74	0.11
0.4	0.10	30	31	0.61	0.02	1.36	0.08
0.5	0.10	29	30	0.30	0.01	1.34	0.08

Due to the addition of Mn ions in NMCCFO samples, both the crystallinity and uniformity changes, which in turn causes the change value of M_s. According to the different research works, the reasons for the decreasing trend in M_s are manifold. The substitution of Mn ions creates strain in the spinel structure, which influences spin cantin and may cause to lowering the value of M_s (Hossen, Nasrin and Hossen, 2020). It is known that Mn is paramagnetic in nature. The magnetic moments of Mn^{2+} and Fe^{3+} are same. The value of μ_B in case of Mn^{2+} (5.0 μ_B) > Ni (2.3 μ_B) (Ghodake et al., 2016). Cation distribution and exchange interaction in between tetrahedral sites and octahedral sites play a strong role in controlling and changing the amount of magnetisation possession in ferrite. According to the Table 5.3 (Cations distribution of NMCCFO), it is observed that Ni^{2+} has a strong tendency to occupy B (octahedral) sites, whereas Mn^{2+} ion shows the partial distribution between A and B sites. In addition, Fe^{3+} and Cu^{2+} ions prefer to exist in tetrahedral and octahedral sites but have more affinity towards B-sites (Smit and Wijn, 1959).

The lower value of M_s due to Mn substitution may be attributed from the existence of weakening A-B exchange interaction owing to the migration of Fe^{3+} ions between tetrahedral and octahedral sites. Furthermore, the formation of more vacancies occurs at B-site due to its lower formation energy than A-site during sintering. These vacancies reduce super-exchange interaction and resist the rotation of the domain wall (Aakash et al., 2016, Eshraghi, Rahimi and Kameli, 2014, Barathiraja et al., 2016).

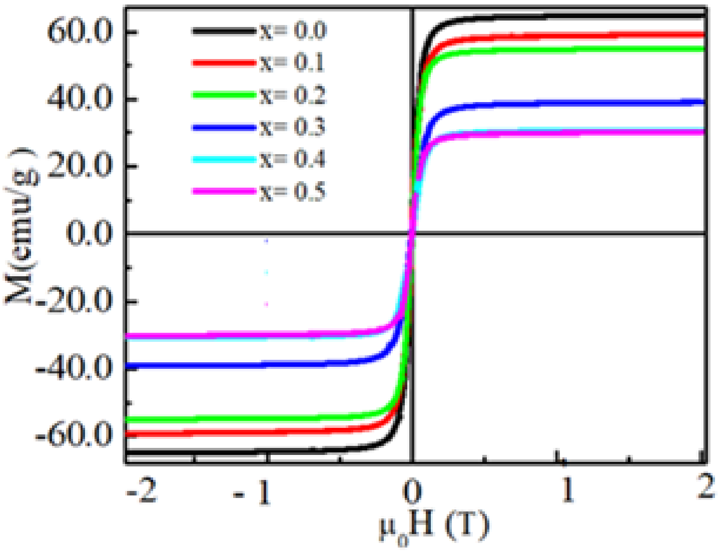

Fig. 5.17: Magnetic Hysteresis Loops of *NMCCFO* for different values of Mn contents.

The decreasing magnetisation may also be explained in terms of densification with Mn content. Generally, a decrease in the material’s density is associated with a decline in magnetization value (Roy, Nayak and Bera, 2008), which could be explained by the following equation:

$$M = \rho_{exp} \times \sigma \tag{5.2}$$

where M = magnetisation, ρ_{exp} = bulk density, and σ = emu/g. Here, ρ_{exp} decrease with the increase of Mn content as shown in Table 5.4.

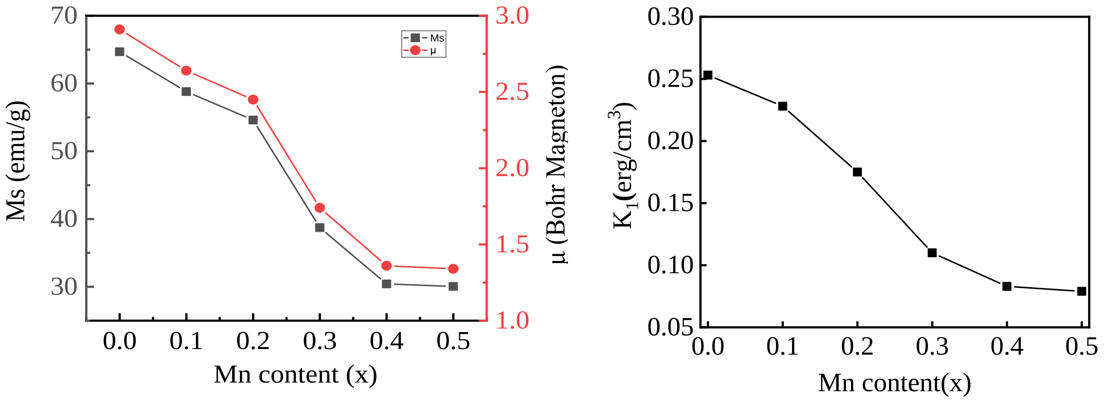

Fig. (a) Fig. (b)

Fig. 5.18: Changes of (a) saturation magnetisation and magnetic moments, (b) anisotropy constant with Mn addition of *NMCCFO* bulk ferrites.

The remanent ratio (R = M_r/M_S), also known as squareness ratio (SQ), measures the quantity of anisotropy present in the sample element. This ratio represents the variation in the magnetisation orientation along the easy axis after removing of the applied magnetic field (Hossen and Hossen, 2019). In the present study, the value of R decreases with the increase of Mn content and the value changes from 0.12 to 0.01 as shown in Table 5.7. The lower value of R indicates the contribution of interactions between the grains and also indicates the random orientation of domains (Amri et al., 2021). The values of effective anisotropy constant (K_1) of *NMCCFO* are tabulated in Table 5.7 for different Mn content. The value of K_1 decreases with the addition of Mn are also shown in Figure 5.18 (b). The decrease of K_1 may be due to the decrease of M_s and M_r with the increase of Mn.

Moreover, the law of approach to saturation (LAS) was applied to analyze the magnetisation curve with the help of Origin-19a software. The saturation magnetisation (M_S) and anisotropy constant (K_1) were measured from the M-H curve by fitting the high field magnetisation data. The obtained results are presented in Table 5.7 and LAS fitted carves are shown in Figure 5.19. The values for both the parameters in different compositions of pure and substituted Ni-Cu-Cd ferrite samples are lesser than the experimental value (Vazquez, Fernengel and Kronmuller, 1987).

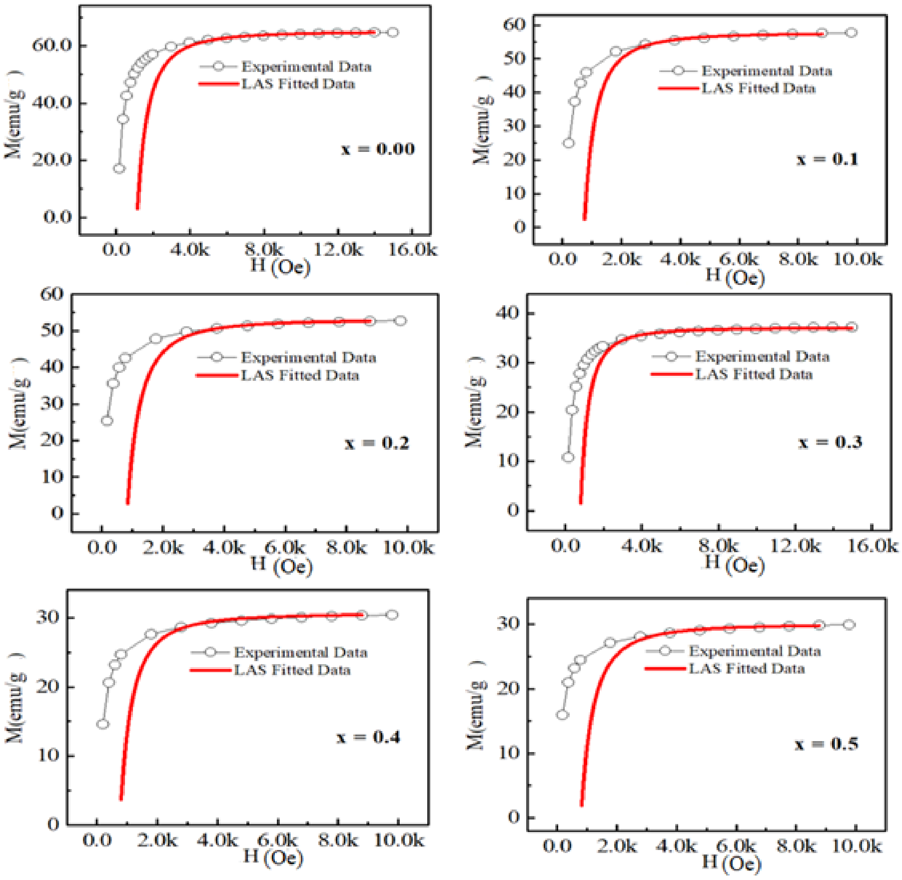

Figure 5.19: LAS curves of Mn substituted *NMCCFO* bulk ferrites.

CHAPTER 6

CONCLUSIONS AND RECOMMENDATIONS

6.1 Conclusions

In the present study, high-density bulk form of various $Ni_{0.5-x}Mn_xCu_{0.2}Cd_{0.3}Fe_2O_4$ (NMCCFO, x = 0.0, 0.1, 0.2, 0.3, 0.4 and 0.5) compositions was prepared from nano-crystalline powders. A simple and cost-effective sol-gel auto-combustion synthesis technique was employed. The effect on the structural, electrical and magnetic properties due to Mn substitution were investigated. From the systematic study, the following conclusions are drawn:

(i) High-density bulk form of NMCCFO nano crystalline compositions was successfully synthesized from commercially available different nitrate salts of the ingredients and were calcined at 700°C for 5 h. Pellet and toroid shaped samples prepared from each composition were sintered at 1200°C for 5 h.

(ii) The XRD pattern confirms the formation of a single-phase cubic spinel structure for all composition with lattice constant 'a' in the range of 8.37 Å – 8.47 Å. The lattice constant increases linearly with Mn^{2+} content. The increase may be attributed to the ionic size differences because the unit cell has to expand when substituted by ions with larger ionic size. The crystallite sizes are in the range of 34 nm -58 nm.

(iii) The Rietveld refinement approach confirms that the refined XRD data of NMCCFO fits well for various Mn content. Additionally, the Rietveld method is used to calculate cation distribution between tetrahedral and octahedral sites. The highest transfer of Fe ions from A-sites to B-sites is found when the Mn content is x = 0.2. Moreover, partial occupancy tendency of Ni^{2+}, Mn^{2+}, Cu^{2+}, Cd^{2+} and Fe^{3+} are observed in both sites.

(iv) The 2D and 3D images of Maximum Entropy Map (MEM) demonstrate the variation of electron density with Mn addition. It also indicates the dominancy of the covalent bonding and the reduction of ionic forms due to the Mn substitution.

(v) The values of X-rays density and bulk density indicate a declining trend with increasing Mn^{2+}. The bulk density is reduced from 4.62 g/cc to 4.01 g/cc. The reason may be due to the substitution of higher density of Ni^{2+} (8.91 g/cc) by lesser density of Mn^{2+} (7.43 g/cc) ion which causes the structural distortion. The porosity is inversely related to the density and is found in the range of 18 % to 26%.

(vi) The field emission scanning electron microscopy (FE-SEM) images reveal the chronological changes in grain distribution due to the substitution of Mn content in the structure as well as the texture turns into lesser homogeneity. The result indicates that the average grain sizes increases from 1 μm to 4 μm for all compositions, except Mn, x = 0.5 content. The presence of Ni, Mn, Cu, Cd, Fe, and O in the samples and also the absence of any traceable impurities in the compositions are confirmed through energy dispersive X-ray (EDX) study.

(vii) The frequency dependence of dielectric analysis is carried out at room temperature in the frequency range 100 Hz to 100 MHz. The result shows that the dielectric constant (ε/) and dielectric loss tangent (tan δ) are high at lower frequencies but became independent of frequency in the higher frequency range for all the compositions of NMCCFO. This behaviour may be explained by the Maxwell-Wagner model.

(viii) The electric modulus ($M^{/}$ and $M^{//}$) spectra exhibit the dynamics of conduction mechanism. At lower frequency region, the real part of $M^{/}$ seems to approach zero value but at higher frequency region, it approaches sharply to saturation value. The imaginary part, $M^{//}$ clearly shows peaking nature. The wider peak explains larger relaxation conductivity. The Cole-Cole plot confirms the existence of single-phase nature of the materials and suggest that the conduction phenomenon is due to non-Debye relaxation mechanism.

(ix) The real part of complex impedance, $Z^{/}$ is high at lower frequency region and decreases with the increase of frequency. This might be the result of the space charge polarization. Different broader peaks of $Z^{//}$ are observed which shows the relaxation behavior in the compositions. The Cole-Cole fitted curves show the contribution of grain and grain boundary resistance in the impedance spectroscopy.

(x) The ac conductivity (σ_{ac}) increases with increasing of frequency for all the compositions of NMCCFO whereas it decreases with increasing Mn content at low frequency region. This dispersive behaviour is mainly affected by manganese ions.

(xi) The magnetization was measured by vibrating sample magnetometer (VSM) at room temperature. The magnetic parameters like hysteresis loop, the saturation magnetisation (M_s), remanent magnetisation (M_r), coercivity (H_c), the ratio (R) of M_r and M_s, anisotropy constant (K_1), and magnetisation magnetic moment (μ_B) are calculated. All the compositions show the nature of soft ferrite due to the small amount of remanence and coercivity. M_s decreases gradually from 51.71 emu/g to 36.34 emu/g with the increase of Mn contents. Theoretical law of approach to saturation (LAS) shows that the values for both the saturation magnetization (M_s) and anisotropy constant (K_1) are lesser than the experimental value.

From the above point, we may conclude that the compositions of Mn = 0.1 and 0.2 show optimum results in terms of lightly changed saturation magnetization as well as reduces K_1, $tan\delta$ at higher frequencies, low grain resistances. Therefore, these compositions may be used as a raw material for manufacturing frequency dependent communication devices like multilayer chip inductor's (MLCI), sensors, phase shifters, switches, etc.

6.2 Suggestions for future work

With the inception of nanotechnology, a raising trend is established in the field of research on miniaturization and high efficiency electronic devices. Besides, consolidating nano-powders into dense bulk form with a view to retaining nano effect along with the advantages of electromagnetic properties is also desirable in many electronic applications. Soft magnetic materials are found promising as the basic magnetic component of these modern gadgets.

6.2.1 Future applicability of NMCCFO

The results of the investigation over a broad frequency range have demonstrated the capability of synthesized dense bulk ferrite for the operation in multifunctional electrical appliances as well as technical equipment in miniaturized versions. Soft ferrite materials are extensively used in multi-layer ferrite chip inductors (MLFCI) which form a basic requirement in high technology areas. The electrical, dielectric and magnetic property analysis reveals the improve nature of investigated samples for the application of high frequency devices in the field of communication like sensors, circulators, and antennas etc which could be a prospective identity in a wide variety of applications to shape the future of advanced technology.

6.2.2 Future scope of improving NMCCFO

However, the scopes of the future works are proposed as:

- The temperature dependent electrical and dielectric properties of the samples may be studied.
- Temperature dependent magnetic permeability and Curie temperature (T_C) of the samples may be determined.
- The optical properties and band gap of the samples may be investigated.
- Other techniques (microwave sintering, spark plasma sintering) may be adopted to obtain less porosity of the samples.
- Ferroelectric hysteresis of the samples may be studied.

REFERENCES

Arifuzaman, M., Abden, M. J., Ahmed, S. K. and Hossen, M. B., (2016). Structural, dielectric and conductivity studies of Ni-Cu-Cd ferrite nanoparticles, Int. Conf. on Innovations in Sci., Eng. Tech. DOI: 10.1109/ICISET.2016.7856511

Ai, L., Zhang, C. and Chen, Z., (2011). Removal of methylene blue from aqueous solution by a solvothermal-synthesized graphene/magnetite composite. J. hazardous mat., 192, 1515-1524. https://doi.org/10.1016/j.jhazmat.2011.06.068

Aakash, Choubey, R., Das, D., and Mukherjee, S., (2016). Effect of doping of manganese ions on the structural and magnetic properties of nickel ferrite, J. Alloys Compd. 668, 33-39. http://doi.org/10.1016/j.jallcom.2016.01.198

Arifuzzaman, M., Hossen, M. B., Afroze, J. D. and Abden, M. J., (2020). Structural and electrical properties of Cu substituted Ni-Cd nano ferrites for microwave applications, Physica B : Cond. Matt., 588, 412170. https://doi.org/10.1016/j.physb.2020.412170

Arjunwadkar, P. R. and Patil, R. R., (2014). Characterization of Al^{3+} substituted lithium ferrite prepared by chemical method, J. Alloys Compd., 611, 273-277. https://doi.org/10.1016/j.jallcom.2014.05.054

Austin, I. G., and Mott, N. F., (1967). Electrons in disordered structures. Adv. Phys. 16 (61), 49-144. https://doi.org/10.1080/00018736700101265

Amri, N., Massoudi, J., Nouri, K. and Triki, M., (2021). Influence of neodymium substitution on structural, magnetic and spectroscopic properties of Ni–Zn–Al nano-ferrites, RSC advances, 11, 13256-13268. DOI:10.1039/d0ra10140k

Belavi, P. B., Chavan, G. N., Naik, L. R., Somashekar, R. and Kotnala, R. K, (2012). Structural, electrical and magnetic properties of cadmium substituted nickel-copper ferrites, Mat. Chem. Phys., 132, 138–144. https://doi.org/10.1016/j.matchemphys.2011.11.009

Batoo, K.M., Kumar, S., Lee, C.G. and Alimuddin, S., (2009). Influence of Al doping on electrical properties of Ni–Cd nano ferrites, Curr. App. Phys., 9, 826-832. DOI:10.1016/j.cap.2008.08.001

Bagum, A., Hossen, M.B. and Chowdhury, F.U.Z. (2016). Complex impedance and electric modulus studies of Al substituted $Co_{0.4}Cu_{0.2}Zn_{0.4}Al_xFe_{2-x}O_4$ ferrites prepared by auto combustion technique, Ferroelectrics 494 (1), 19–32.

Blum, S.L., (1958). Microstructure and Properties of Ferrites, J. Am. Ceram. Soc., 41 (11), 489–493. https://doi.org/10.1111/j.1151-2916.1958.tb12902.x

Behera, A., Mohanty, N., Satpathy, S., Behera, B. and Nayak, P., (2014). Investigation of complex impedance and modulus properties of Nd doped $0.5BiFeO_30.5PbTiO_3$ multiferroic Composites, Cent. Eur. J. Phys., 12 (12), 851-861. https://doi.org/10.2478/s11534-014-0523-2

Barathiraja, C., Manikandan, A., Mohideen, A. M. U., Jayasree, S. and Antony, S. A., (2016). Magnetically recyclable spinel $Mn_xNi_{1-x}Fe_2O_4$ (x = 0.0-0.5) nano-photocatalysts: structural, morphological and opto- magnetic properties, J. Supercond. Nov. Magn., 29, 477–486. DOI: 10.1007/S10948-015-3312-2

Callister, W. D., David, J. and Rethwisch, G., (2013). Materials Science and Engineering an introduction, 9th Ed., John Wiley & Sons, USA.

Cruickshank, D., (2003). 1–2 GHz dielectrics and ferrites: overview and perspectives, J. Eur. Ceram. Soc., 23, 2721-2726. DOI:10.1016/S0955-2219(03)00145-6

Cullity, B. D., (1959). The Elements of X-ray Diffraction, Addison-Wesley, London.

Cheng, F., Liao, C., Kuang, J., Xu, Z., Yan, C., Chen, L. and Liu. Z., (1999). Nanostructure magneto-optical thin films of rare earth (RE = Gd, Tb, Dy) doped cobalt spinel by sol-gel synthesis, J. Appl. Phys., 85(5), 2782–2786. DOI : 10.1063/1.369594

Devmunde, B. H., Raut, A. V., Birajdar, S. D., Shukla, S. J., Shengule, D. R. and Jadhav, K. M., (2016). Structural, Electrical, Dielectric, and Magnetic Properties of Cd^{2+} Substituted Nickel Ferrite Nanoparticles, J. Nanoparticles, Volume 2016 Article ID 4709687. https://doi.org/10.1155/2016/4709687

Das, N., Bhattacharya, D., Sen, A. and Maiti, H. S., (2009). Sonochemical synthesis of $LaMnO_3$ nano-powder, Cera. Intern., 35, 21-24. https://doi.org/10.1016/j.ceramint.2007.09.002

Deraz, N. and Alarifi, M. A., (2012). Structural, morphological and magnetic properties of nanocrystalline zinc substituted cobalt ferrite system, J. Anal. Appl. Pyrolysis, 94, 41-47. https://doi.org/10.1016/j.jaap.2011.10.004

Eshraghi, M., Rahimi, M. and Kameli, P., (2014). Structural and magnetic characterizations of Cd-substituted nickel ferrite nanoparticles, Ceram. Int. 40 (10), 15569–15575. https://doi.org/10.1016/j.ceramint.2014.07.033

Ghodake, U. R., Chaudhari, N. D., Kambale, R. C., Patil, J. Y. and Suryavanshi, S. S., (2016). Effect of Mn^{2+} substitution on structural, magnetic, electric and dielectric properties of Mg–Zn ferrites, J. Magn. Magn. Mater., 407, 60-68. https://doi.org/10.1016/j.jmmm.2016.01.022

Hashim, M., Alimuddin, S., Shirsath, E., Kumar, S., Kumar, R., Roy, A. S., Shah, J. and Kotnala, R.K., (2013). Preparation and characterization chemistry of nano-crystalline Ni–Cu–Zn ferrite, J. Alloy Compd., 549, 348–357. https://doi.org/10.1016/j.jallcom.2012.08.039

Hashim, M., (2012). Structural, magnetic and electrical properties of Al^{3+} substituted Ni-Zn ferrite nanoparticles, J. Alloys Compd., 511 (1), 107–114. https://doi.org/10.1016/j.jallcom.2011.08.096

Hassan, H. E., Sharshar, T., Hessien, M. M. and Hemeda, O. M., (2013). Effect of X-rays irradiation on Mn–Ni ferrites: Structure, magnetic properties, and positron annihilation studies, Nucl. Instrum. Method. Phys. Research. B, 304, 72–79. https://doi.org/10.1016/j.nimb.2013.03.05

Hossen, M. M. and Hossen, M. B., (2019). Study of structural and electrical properties along with magnetic properties of $Ni_{0.5-x}Mg_xCu_{0.2}Cd_{0.3}Fe_2O_4$ nano ferrites synthesized by employing sol-gel auto-combustion method, J. Mat. Sci.: Materials in Electronics 30, 20801–20815. https://doi.org/10.1007/s10854-019-02447-x

Hossen, M. M., Nasrin, S. and Hossen, M. B., (2020). Effect of Mn^{2+} doping on structural, magnetic and electrical properties of $Ni_{0.5-x}Mn_xCu_{0.2}Cd_{0.3}Fe_2O_4$ nano ferrites prepared by sol-gel auto combustion method for high-frequency applications, Physica B : Cond. Matt., 599, 412456. https://doi.org/10.1016/j.physb.2020.412456

Hankare, P. P., Kadam, M. R., Patil, R. P., Garadkar, K. M., Sasikala, R. A. and Tripathi, K., (2010). Effect of zinc substitution on structural and magnetic properties of copper ferrite, J. Alloys Compd., 501 (1) 37. https://doi.org/10.1016/j.jallcom.2010.03.178

Hoque, S. M., Choudhury, M. A. and Islam, M. F., (2002). Characterization of Ni–Cu mixed spinel ferrite, J. Magn. Magn. Mater., 251 (3) 292–303. https://doi.org/10.1016/S0304-8853(02)00700-X

Hussain, A., Abbas, T. and Niazi, S. B., (2013). Preparation of$Ni_{1-x}Mn_xFe_2O_4$ ferrites by sol-gel method and study of their cation distribution, Ceram. Internat., 39, 1221–1225. http://dx.doi.org/10.1016/j.ceramint.2012.07.049

Jonscher, A. K., (1977). The 'universal' dielectric response, Nature, 267, 673-679.

Kumar, E. R.and Jayaprakash, R., (2013). Effect of combustion rate and annealing temperature on structural and magnetic properties of manganese substituted nickel and zinc ferrites, J. Magn. Magn. Mater., 348 (2013) 93–100. https://doi.org/10.1016/j.jmmm.2013.07.042

Kang, M., (2003). Synthesis of Fe/TiO photocatalyst with nanometer size by solvo-thermal method and the effect of HO addition on structural stability and photodecomposition of methanol. J. Molecular Catalysis A: Chemical, 197, 173-183. https://doi.org/10.1016/S1381-1169(02)00586-1

Khan, M., Duan, J., Chen, Y., Yao, H., Lyu, S., Shou, H., Heng, K. and Xu, Q., (2017). Superparamagnetic nickel–substituted manganese ferrite ($Mn_{0.8}Ni_{0.2}Fe_2O_4$) nanoplates as anode materials for lithium-ion batteries, J. Alloys Compd., 701, 147-152. http://dx.doi.org/10.1016/j.jallcom.2017.01.113

Kumar, L., Kumar, P., Narayan, A. and Kar, M., (2013). Rietveld analysis of XRD patterns of different sizes of nanocrystalline cobalt ferrite, Int. Nano Lett., 3 (1), 1–12. https://doi.org/10.1186/2228-5326-3-8

Koops, C.G., (1951). On the dispersion of resistivity and dielectric constant of some semiconductors at audio frequencies. Phys. Rev., 83 (1), 121–124. https://doi.org/10.1103/PhysRev.83.121

Kadam, A.A., Shinde, S.S., Yadav, S.P., Patil, P.S. and Rajpure, (2013). Structural morphological, electrical and magnetic properties of Dy doped Ni–Co substitutional spinel ferrite, J. Magn. Magn. Mater., 329, 59–64. https://doi.org/10.1016/j.jmmm.2012.10.008

Lodhi, M. Y., Mahmood, K., Mahmood, A., Malik, H., Warsi M. F., Shakir, I., Asghar, M. and Khan, M. A., (2014). New $Mg_{0.5}Co_xZn_{0.5-x}Fe_2O_4$ nano-ferrites: Structural elucidation and electromagnetic behavior evaluation, Curr. Appl. Phys., 14, 716. https://doi.org/10.1016/j.cap.2014.02.021

Lyakishev, N. P., Alymov, M. I. and Dobatkin, S. V., (2003). Structural Bulk Nanomaterials, Russian Metallurgy (Metally), 2003 (3), 191-202. https://www.researchgate.net/publication/288371185

Morales, J. R., Garay, J. E., Biasini, M. and Beyermann, W. P., (2008). Magnetic characterization of bulk nanostructured iron oxides, App. Phys. Lett., 93, 022511. DOI: 10.1063/1.2959070

Mokdad, I.F. A., Hassan, R. S. and Awad, R., (2019). Physical and Dielectric Properties of $MnFe_2O_4$ Doped by Mo, Current Nanomaterials, 4 (2), 125-136. DOI:10.2174/2405461504666190405153730

Marinca, T.F., Chicinaş, I., Isnard, O. and Popescu, V., (2013). Nanocrystalline/Nanosized $Ni_{1-\gamma}Fe_{2+\gamma}O_4$, ferrite obtained by contamination with Fe during milling of NiO–Fe_2O_3 mixture. Structural and magnetic characterization, J. Am. Ceram. Soc., 96(2), 469–475. https://doi.org/10.1111/jace.12043

Mirzaee, S., Kalandaragh, Y. A. and Rahimzadeh, P., (2020). Modified co-precipitation process effects on the structural and magnetic properties of Mn-doped nickel ferrite nanoparticles, Sol. Stat. Sci., 99, 106052. https://doi.org/10.1016/j.solidstatesciences.2019.106052

Mirzaee, S., Shayesteh, S. F. and Mahdavifar, S., (2014). Anisotropy investigation of cobalt ferrite nanoparticles embedded in polyvinyl alcohol matrix: A Monte Carlo study, Polym., 55 (16), 3713-3719. https://doi.org/10.1016/j.polymer.2014.06.039

Muhammad, A. and Maqsood, A., (2008). Structural, electrical and magnetic properties of $Cu_{1-x}Zn_xFe_2O_4$ ($0 \leq x \leq 1$), J. Alloys Compds., 460, 54−59. https://doi.org/10.1016/j.jallcom.2007.06.019

Mahmood, M. and Hossen, M., (2021). Dynamic response of electrical, dielectric and magnetic properties of La-substituted Ni-Cu-Cd bulk ceramics with structural rietveld refinement, J. Mater. Sci: Mater. Electron., 32, 14248–14273. https://doi.org/10.1007/s10854-021-05988-2

Magdysyuk, O. V., Smaalen, S. V. and Dinnebier, R. E., (2019). Application of the maximum-entropy method to powder-diffraction data. International Tables for Crystallography, Vol. H, ch. 4.8, 473-488. doi:10.1107/97809553602060000963

Maxwell, J.C., (1954). Electricity and Magnetism, vol. 328, Oxford University Press, New York.

Miah, M. J. and Hossain, A. K. M. A., (2016). Magnetic, Dielectric and Complex Impedance Properties of $xBa_{0.95}Sr_{0.05}TiO_3 - (1-x)BiFe_{0.9}Gd_{0.1}O_3$ Multiferroic Ceramics, Acta Metall. Sin. Engl. Lett., 29 (6), 505-517. https://doi.org/10.1007/s40195-016-0408-z

Narang, S. B. and Pubby, K., (2021). Nickel Spinel Ferrites: A Review, J. Magn. Magn. Mater., 519, 167163. doi.org/10.1016/j.jmmm.2020.167163

Nath, S. K., Maria, K. H., Noor, S., Sikder, S. S., Hoque, S. M. and Hakim, M. A., (2012). Magnetic ordering in Ni–Cd ferrite, J. Magn. Magn. Mater, 324, 2116. https://doi.org/10.1016/j.jmmm.2012.02.023

Nersesyan, M. D., Peresada, A. G. and A. G. Merzhanov, (1998), Int. J. SHS 7, 60

Ohta, K. and Kobayshi. N., (1964). Magnetostriction constants of Mn-Zn-Fe ferrites, Jpn. J. Appl. Phys., 3 (10) 576.

Patil, A. N., Patil, M. G., Patankar, K. K., Mathe, V. L., Mahajan, R. P. and Patil, S. A., (2000). Dielectric behaviour and a.c. conductivity in $Cu_xFe_{3-x}O_4$ ferrite, Bull. Mater. Sci., 23 (5), 447-452. https://doi.org/10.1007/BF02708397

Patil, B. B., Pawar, A. D., Bhosale, D. B., Ghodake, J. S., Thorat, J. B. and Shinde, T. J., (2019). Effect of La^{3+} substitution on structural and magnetic parameters of Ni–Cu–Zn nano-ferrites, J. Nanostruc. Chem., 9, 119–128. https://doi.org/10.1007/s40097-019-0302-0

Pandav, R. S., Patil, R. P., Chavan, S. S., Mulla, I. S. and Hankare, P. P., (2016). Magneto-structural studies of sol-gel synthesized nanocrystalline manganese substituted nickel ferrites. J. Magn. Magn. Mater., 417, 407–412. http://dx.doi.org/10.1016/j.jmmm.2016.04.090

Ram, M. and Chakrabarti, S., (2008). Dielectric and modulus behavior of $LiFe_{1/2}Ni_{1/2}VO_4$ ceramics, J. Phys. Chem. Solids, 69 (4), 905–912. https://doi.org/10.1016/j.jpcs.2007.10.008

Raghuvanshi, S., Mazaleyrat, F. and Kane, S. N., (2018). $Mg_{1-x}Zn_xFe_2O_4$ nanoparticles: Interplay between cation distribution and magnetic properties, AIP Advances, 8, 047804. https://doi.org/10.1063/1.4994015

Rezlescu, N., Rezlescu, E., Pasnicu, C. and Craus, M., (1994). Effects of the rare-earth ions on some properties of a nickel-zinc ferrite, J. Phys: Condens. Mat., 6, 5707-5716. https://doi.org/10.1088/0953- 8984/6/29/013

Roy, P. K., Nayak, B. B. and Bera, J., (2008). Study on electromagnetic properties of La substituted Ni-Cu-Zn ferrite synthesized by auto-combustion method, J. Magn. Magn. Mater., 320, 1128–1132. https://doi.org/10.1016/j.jmmm.2007.10.025

Raju, K., Balaji, C. G. and Reddy P. V., (2014). Microwave properties of Al and Mn-doped nickel ferrites at Ku band frequencies, J. Magn. Magn. Mater., 354, 383–387. https://doi.org/10.1016/j.jmmm.2013.11.040

Singh, S.B., Srinivas, C. and Tirupanyam, B.V., (2016). Structural, thermal and magnetic studies of $Mg_xZn_{1-x}Fe_2O_4$ nano ferrites: a study of exchange interactions on magnetic anisotropy, Ceram. Int., 42 (16), 19179–19186. doi: 10.1016/j.ceramint.2016.09.081

Shelar, M. B., Jadhav, P. A., Chougule, S. S., Mallapur, M. M. and Chougule, B. K., (2009). Structural and electrical properties of nickel-cadmium ferrites prepared through self-propagating auto combustion method, J. Alloys Compd., 476, 760–764. https://doi.org/10.1016/j.jallcom.2008.09.107

Siddique, M., Butt, N. M., Shafi, M., Abbas, T. and Islam, M., (2003). Cation distribution in Ni-substituted Mn-ferrites by Mössbauer technique, J. Radioanal. Nucl. Chem., 258 (3), 525-529. DOI:10.1023/B:JRNC.0000011746.68066.f5

Shirsath, S. E., Toksha, B. G., Kadam, R. H., Patange, S. M., Mane, D. R., Ganesh, S., Jangam and Ghasemi, A., (2010). Doping effect of Mn^{2+} on the magnetic behavior in Ni–Zn ferrite nanoparticles prepared by sol-gel auto-combustion, J. Phys. Chem. Solid., 71, 1669–1675. https://doi.org/10.1016/j.jpcs.2010.08.016

Standely, J., (1972). Oxide Magnetic Materials, Clarendon, Oxford, UK.

Smit, J. H. and Wijn, P. J., (1959). Ferrites, Philips Technical Library, Eindhovan, the Netherlands.

Soibam, I., (2016). A study of microwave sintered ni substituted lithium zinc ferrite synthesized by citrate precursor method**,** Int. J. Mater Sci. Eng., 4 (1), 54–59. https://doi.org/10.17706/ijmse.2016.4.1.54-59

Sujatha, C., Reddy, K.V., Babu, K.S., Reddy, A.R.C. and Rao, K.H., (2012). Structural and magnetic properties of Mg substituted NiCuZn Nano Ferrites, Physica B : Cond. Matt., 407, 1232–1237. https://doi.org/10.1016/j.physb .2012.01.108

Suzuki, T., Tanaka, T. and Ikemizu, K., (2001). High density recording capability for advanced particulate media, J. Magn. Magn. Mater., 235, 159-164. https://doi.org/10.1016/S0304-8853(01)00329-8

Singh, A. K., Verma, A., Thakur O. P., Prakash, C., Goel, T. C. and Mendiratta, R. G., (2003). Electrical and magnetic properties of Mn-Ni-Zn ferrites processed by citrate precursor method, Mater. Lett., 57, 1040–1044. https://doi.org/10.1016/S0167-577X(02)00921-7

Shah, M. R. and Hossain, A. K. M. A., (2013). Structural, Dielectric and Complex Impedance Spectroscopy studies of Lead Free $Ca_{0.5+x}Nd_{0.5-x}(Ti_{0.5}Fe_{0.5})O_3$, J. Mater. Sci. Technol., 29 (4) 323-329. https://doi.org/10.1016/j.jmst.2012.11.008

Thangjam, B. and Soibam., I., (2017). Comparative study of structural, electrical, and magnetic behaviour of Ni-Cu-Zn nanoferrites sintered by microwave and conventional techniques, J. Nanomat. Article ID 5756197, 1–10. https://doi.org/10.1155/2017/5756197

Tatarchuk, T., Bououdina, M., Vijaya, J. J. and Kennedy, L. J., (2017). Spinel Ferrite Nanoparticles: Synthesis, Crystal Structure, Properties, and Perspective Applications. Springer International Publishing, 195, 305-325. DOI 10.1007/978-3-319-56422-7_22

Thakura, P., Chahara, D., Tanejaa, S., Bhallab, N. and Thakurc, A., (2020). A review on MnZn ferrites: Synthesis, characterization and applications, Ceram. Int., 46 (10), 15740-15763. https://doi.org/10.1016/j.ceramint.2020.03.287

Tirupanyam, B. V., Srinivas, C., Meena, S. S., Yusuf, S. M., Kumar, A. S., Sastry, D. L. and Seshubai, V., (2015). Investigation of Structural and Magnetic Properties of co-precipitated Mn-Ni Ferrite nanoparticles in the Presence of α-Fe_2O_3 Phase, J. Magn. Magn. Mater., 392, 101–106. http://dx.doi.org/10.1016/j.jmmm.2015.05.010

Tsunekawa, H., Nakata, A., Kamijo, T., Okutani, K., Mishra, R. K., and Thomas, G., (1979). Microstructure and properties of commercial grade manganese zinc ferrites, IEEE Trans. Magn., 15 (6) 1855–1857. DOI: 10.1109/TMAG.1979.1060382

Upadhyay, C., Verma, H. C. and Anand, S., (2004). Cation distribution in nanosized Ni–Zn ferrite, J. Appl. Phys., 95 (10), 5746-5751. https://doi.org/10.1063/1.1699501

Valenzuela, R., Gaudisson, T. and Ammar, S., (2015). Severe reduction of Ni–Zn ferrites during consolidation by Spark Plasma Sintering (SPS), J. Magn. Magn. Mater., 400, 311-314. doi.org/10.1016/j.jmmm.2015.07.044

Valenzuela, R., (2012). Review article: Novel Applications of Ferrites. Hindawi Publishing Corporation, Physics Research International, Vol 2012, Article ID 591839, 9 page. doi:10.1155/2012/591839

Zhao, L., Yang, H., Yu, L., Cui, Y., Zhao, X. and Feng, S., (2007). Magnetic properties of Resubstituted Ni–Mn ferrite nanocrystallites, J. Mat. Sci., 42 (2), 686–691. DOI:10.1007/s10853-006-0273-7

Zulqarnain, M., Ali, S.S., Hira, U., Feng , J.F., Khan , M.I., Rizwan , M. K., Farid , J. G. and Hasan, M.S., (2022). Superparamagnetic contributions, optical band gap tuning and dominant interfacial resistive mechanisms in ferrites nanostructures, J. Alloys Compd., 894, 162431. https://doi.org/10.1016/j.jallcom.2021.162431

Zaharescu, M., Balasoiu, M., Crisan, M., Crisan, D., Tavala, T. and Moser, V., (1984). The influence of the properties of ferric oxides on the formation of Mn-Zn ferrite, Rev. Roum. Chim., 29 (3), 247–252.

List of presentation

Presentations

1. Abstract on topic **'The structural with Reitveld analysis, magnetic and electrical properties of Mn substituted Ni-Cu-Cd bulk ferrites synthesized from nanocrystalline powders'** was accepted in 7th Conference of Bangladesh Crystallographic Association held on 8-9 December, 2022 at BUET, Dhaka-1000. Oral presentation was also performed successfully on the same occasion.

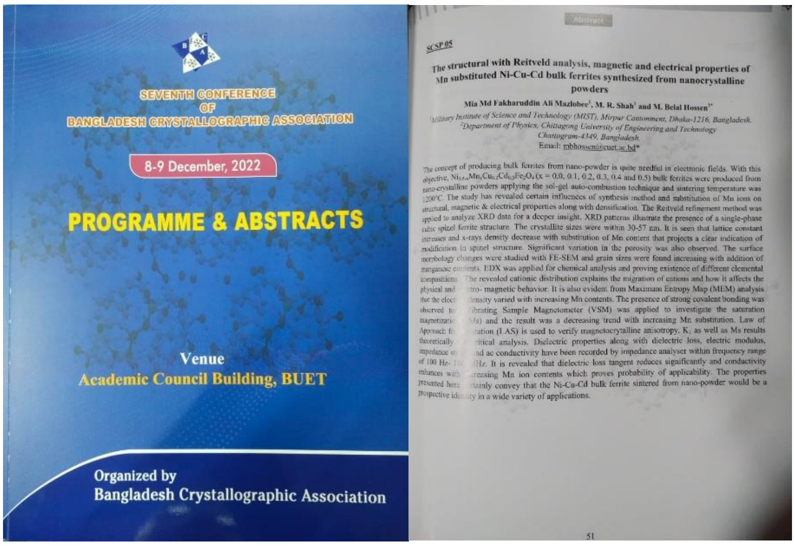

SEVENTH CONFERENCE
OF
BANGLADESH CRYSTALLOGRAPHIC ASSOCIATION

8-9 December, 2022

PROGRAMME & ABSTRACTS

Venue
Academic Council Building, BUET

Organized by
Bangladesh Crystallographic Association

Abstract

SCSP 05

The structural with Reitveld analysis, magnetic and electrical properties of Mn substituted Ni-Cu-Cd bulk ferrites synthesized from nanocrystalline powders

Mia Md Fakharuddin Ali Mazlobee[1], M. R. Shah[1] and M. Belal Hossen[2*]

[1]*Military Institute of Science and Technology (MIST), Mirpur Cantonment, Dhaka-1216, Bangladesh.*
[2]*Department of Physics, Chittagong University of Engineering and Technology*
Chattogram-4349, Bangladesh.
Email: mbhossen@cuet.ac.bd*

The concept of producing bulk ferrites from nano-powder is quite needful in electronic fields. With this objective, $Ni_{0.5-x}Mn_xCu_{0.2}Cd_{0.3}Fe_2O_4$ (x = 0.0, 0.1, 0.2, 0.3, 0.4 and 0.5) bulk ferrites were produced from nano-crystalline powders applying the sol-gel auto-combustion technique and sintering temperature was 1200°C. The study has revealed certain influences of synthesis method and substitution of Mn ions on structural, magnetic & electrical properties along with densification. The Reitveld refinement method was applied to analyze XRD data for a deeper insight. XRD patterns illustrate the presence of a single-phase cubic spinel ferrite structure. The crystallite sizes were within 30-57 nm. It is seen that lattice constant increases and x-rays density decrease with substitution of Mn content that projects a clear indication of modification in spinel structure. Significant variation in the porosity was also observed. The surface morphology changes were studied with FE-SEM and grain sizes were found increasing with addition of manganese contents. EDX was applied for chemical analysis and proving existence of different elemental compositions. The revealed cationic distribution explains the migration of cations and how it affects the physical and electro- magnetic behavior. It is also evident from Maximum Entropy Map (MEM) analysis that the electron density varied with increasing Mn contents. The presence of strong covalent bonding was observed [illegible] Vibrating Sample Magnetometer (VSM) was applied to investigate the saturation magnetization (Ms) and the result was a decreasing trend with increasing Mn substitution. Law of Approach for [illegible] ration (LAS) is used to verify magnetocrystalline anisotropy, K_1 as well as Ms results theoretically [illegible] critical analysis. Dielectric properties along with dielectric loss, electric modulus, impedance [illegible] and ac conductivity have been recorded by impedance analyser within frequency range of 100 Hz- [illegible] Hz. It is revealed that dielectric loss tangent reduces significantly and conductivity enhances with increasing Mn ion contents which proves probability of applicability. The properties presented here certainly convey that the Ni-Cu-Cd bulk ferrite sintered from nano-powder would be a prospective identity in a wide variety of applications.

51

7th Conference of Bangladesh Crystallographic Association

Certificate of Participation

This is to certify that Name: *Mia Md Fakharuddin Ali Mazlobee*
Institution: *Military Institute of Science and Technology, Mirpur Cantonment, Dhaka-1216, Bangladesh.*
has given an oral presentation
Title: *The structural with Reitveld analysis, magnetic and electrical properties of Mn substituted Ni-Cu-Cd bulk ferrites synthesized from nanocrystalline powders*
in the 7th Conference of Bangladesh Crystallographic Association held on 08-09 December 2022 at Bangladesh University of Engineering and Technology, Dhaka-1000, Bangladesh.
We wish him/her every success in life.

A. Hossain.
Prof. Dr. A. K. M. Akther Hossain
Chair, Organizing Committee
Department of Physics, BUET

Prof. Dr. Mohammad Mizanur Rahman
Organizing Secretary, Organizing Committee
Department of Physics, University of Dhaka

2. Abstract on topic **'Analysis on the structural and magnetic properties of Mn substituted Ni-Cu-Cd bulk ferrites synthesized from nanocrystalline powders'** was accepted in 4th International Conference on ''Physics for Sustainable Development and Technology (ICPSDT 2022)'' held on January 22-23, 2022 at Department of Physics, CUET, Bangladesh. Online presentation was also performed on the same occasion.

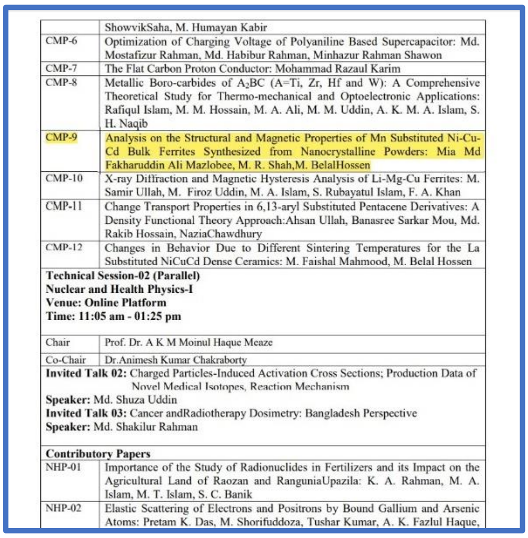

	ShowvikSaha, M. Humayan Kabir
CMP-6	Optimization of Charging Voltage of Polyaniline Based Supercapacitor: Md. Mostafizur Rahman, Md. Habibur Rahman, Minhazur Rahman Shawon
CMP-7	The Flat Carbon Proton Conductor: Mohammad Razaul Karim
CMP-8	Metallic Boro-carbides of A_2BC (A=Ti, Zr, Hf and W): A Comprehensive Theoretical Study for Thermo-mechanical and Optoelectronic Applications: Rafiqul Islam, M. M. Hossain, M. A. Ali, M. M. Uddin, A. K. M. A. Islam, S. H. Naqib
CMP-9	Analysis on the Structural and Magnetic Properties of Mn Substituted Ni-Cu-Cd Bulk Ferrites Synthesized from Nanocrystalline Powders: Mia Md Fakharuddin Ali Mazlobee, M. R. Shah,M. BelalHossen
CMP-10	X-ray Diffraction and Magnetic Hysteresis Analysis of Li-Mg-Cu Ferrites: M. Samir Ullah, M. Firoz Uddin, M. A. Islam, S. Rubayatul Islam, F. A. Khan
CMP-11	Change Transport Properties in 6,13-aryl Substituted Pentacene Derivatives: A Density Functional Theory Approach:Ahsan Ullah, Banasree Sarkar Mou, Md. Rakib Hossain, NaziaChawdhury
CMP-12	Changes in Behavior Due to Different Sintering Temperatures for the La Substituted NiCuCd Dense Ceramics: M. Faishal Mahmood, M. Belal Hossen
Technical Session-02 (Parallel) **Nuclear and Health Physics-I** **Venue: Online Platform** **Time: 11:05 am - 01:25 pm**	
Chair	Prof. Dr. A K M Moinul Haque Meaze
Co-Chair	Dr.Animesh Kumar Chakraborty
Invited Talk 02: Charged Particles-Induced Activation Cross Sections; Production Data of Novel Medical Isotopes, Reaction Mechanism **Speaker:** Md. Shuza Uddin **Invited Talk 03:** Cancer andRadiotherapy Dosimetry: Bangladesh Perspective **Speaker:** Md. Shakilur Rahman	
Contributory Papers	
NHP-01	Importance of the Study of Radionuclides in Fertilizers and its Impact on the Agricultural Land of Raozan and RanguniaUpazila: K. A. Rahman, M. A. Islam, M. T. Islam, S. C. Banik
NHP-02	Elastic Scattering of Electrons and Positrons by Bound Gallium and Arsenic Atoms: Pretam K. Das, M. Shorifuddoza, Tushar Kumar, A. K. Fazlul Haque,